UNIVERSITY OF SOUTHAMPTON

# CHARGE TRANSPORT MECHANISMS IN CORONA CHARGED POLYMERIC MATERIALS

By

YUAN ZHUANG

A thesis submitted for the degree of Doctor of Philosophy

Supervisors: Prof George Chen

Dr Mihai Rotaru

School of Electronics and Computer Science

Faculty of Physical Sciences and Engineering

University of Southampton

United Kingdom

May 2013

UNIVERSITY OF SOUTHAMPTON

# ABSTRACT

FACULTY OF PHYSICAL SCIENCES AND ENGINEERING
ELECTRONICS AND COMPUTER SCIENCE

Doctor of Philosophy

by Yuan Zhuang

Polymeric materials have been widely used as an insulator due to their excellent electrical properties, light weight and low cost. Surface potential measurement is one of the simplest and low cost tools to gauge electrical properties of materials. Once charged, the surface charges or surface potential tend to decay over a period of time, and the exact pattern of the decay represents the characteristic of the material. For corona charged sample, it has been observed that the potential of sample with an initial high surface potential decays faster than that with an initial lower surface potential, known as the cross-over phenomenon. Various theories and models have been proposed to explain the phenomenon. The common feature of these models is that they are all based on single charge carrier injection from corona charged surface. With the recent experimental results on comparing different types of ground of corona charged low density polyethylene sample, bipolar charge injection from both electrodes has been verified. Based on this fact, a new model based on bipolar charge injection has been proposed. In this thesis, the detail of the new model was tested both experimentally and numerically. The new simulation results show that several features experimentally observed can be readily revealed using the bipolar charge injection model. More importantly, the modelling can illustrate charge dynamics across the sample and allows one to extract parameters that are associated with material properties. The effect on different charging polarities and charging times were also discussed in the thesis. Additionally, experiments have been done to nano polyimide materials and the results clearly show that adding different amounts of nano-particles can change the material's electrical property.

# Table of Contents

ABSTRACT ..... i

Table of Contents ..... ii

List of Figures ..... v

List of Tables ..... ix

Definitions and Abbreviations ..... x

Publications ..... xii

Acknowledgements ..... xiv

**Chapter 1 Introduction** ..... - 1 -

1.1 Underground power cables ..... - 1 -

1.2 Polyethylene ..... - 2 -

1.3 Charge Transport ..... - 5 -

*1.3.1 Charge transport in metal, semiconductor and insulator* ..... - 5 -

*1.3.2 Traps in Polymer* ..... - 6 -

1.4 Research aims and objectives ..... - 7 -

1.5 Contributions ..... - 8 -

**Chapter 2 Surface Potential Decay and Experimental Setup** ..... - 10 -

2.1 Background ..... - 10 -

*2.1.1 Previous work review* ..... - 10 -

*2.1.2 Application of the potential decay research* ..... - 11 -

*2.1.3 Measurements of electrostatic potentials* ..... - 12 -

*2.1.4 Corona discharge* ..... - 14 -

2.2 Surface Potential Decay Experimental Details ..... - 14 -
2.3 The cross-over phenomenon ..... - 18 -
2.4 Experimental details of corona charging current measurement and space charge measurement ..... - 19 -
*2.4.1 Corona charging current measurement* ..... - 19 -
*2.4.2 Space charge measurement -- Pulsed Electro-acoustic Method (PEA)* - 20 -
**Chapter 3 A New Model on Surface Potential Decay** ..... - 23 -
3.1 Existing Models ..... - 23 -
3.2 Bipolar charge transport model ..... - 25 -
3.3 New model on surface potential decay ..... - 30 -
3.4 Effect of parameters in the model ..... - 33 -
**Chapter 4 Effect of Different Ground Electrodes on Surface Potential Decay** . - 39 -
4.1 Gold ground sample preparation ..... - 39 -
4.2 Experimental Results and Discussion ..... - 40 -
*4.2.1 Surface potential decay measurement* ..... - 40 -
*4.2.2 Corona charging current measurement* ..... - 42 -
*4.2.3 Space charge measurement* ..... - 43 -
*4.2.4 Discussion* ..... - 48 -
4.3 Simulation Results ..... - 50 -
4.4 Conclusions ..... - 51 -
**Chapter 5 Surface Potential Decay with Different Polarity and Charging Times**- 53 -
5.1 Effect of Different Polarity ..... - 53 -
5.2 Effect of Different Charging Time ..... - 55 -
*5.2.1 Surface Potential Decay Measurements* ..... - 55 -
*5.2.2 PEA Measurements* ..... - 60 -
5.3 Discussion ..... - 62 -
*5.3.1 Double Exponential Decay Analysis* ..... - 62 -

*5.3.2 Simulation Results* ..... - 65 -

*5.3.3 Trap Energy Distribution* ..... - 66 -

**Chapter 6 Simulation on Surface Potential Decay** ..... - 69 -

6.1 Mathematical Analysis on Experimental Results ..... - 69 -

6.2 Simulation Results ..... - 73 -

6.3 Conclusions ..... - 78 -

**Chapter 7 Surface Potential Decay of Nano-polyimide Material Test** ..... - 79 -

7.1 Introduction ..... - 79 -

7.2 Experimental Results ..... - 80 -

*7.2.1 Tests on high percentage nano-PI* ..... - 80 -

*7.2.2 Tests on low percentage nano-PI* ..... - 84 -

7.3 Discussion ..... - 88 -

**Chapter 8 Modelling of Corona Charging Process** ..... - 91 -

8.1 Introduction ..... - 91 -

8.2 Model Description ..... - 93 -

*8.2.1 Geometry of the model* ..... - 93 -

*8.2.2 Mathematical model* ..... - 94 -

*8.2.3 Boundary and initial conditions* ..... - 96 -

8.3 Simulation results ..... - 96 -

*8.3.1 Effect of the grid electrode height* ..... - 97 -

*8.3.2 Effect of the geometry of grid electrode* ..... - 100 -

8.4 Conclusion ..... - 103 -

**Chapter 9 Conclusions and Future Work** ..... - 104 -

9.1 Conclusions ..... - 104 -

9.2 Future work ..... - 106 -

**Appendix A Matlab code for bipolar charge transport model** ..... - 108 -

**References** ..... - 122 -

# List of Figures

Figure 1-1 Polymerization of ethylene to polyethylene [4]. ..... - 3 -
Figure 1-2 Energy band diagram for metals, semiconductors and insulators. ..... - 6 -
Figure 1-3 Schematic representation of state density in a disordered dielectric material. Shallow and deep traps are related to physical and chemical disorder, respectively .. - 7 -
Figure 2-1 The decaying curves of positive charge on the polyethylene film of 0.015mm thick with a little amount of surface active agent [14]. ..... - 11 -
Figure 2-2 Schematic diagram of the field mill [50] ..... - 13 -
Figure 2-3 Surface potential decay measurement system ..... - 15 -
Figure 2-4 The sensitivity varies with separation distance from surfaces for JCI 140 static monitor [53] ..... - 16 -
Figure 2-5 Calibration of current experiment measurement system ..... - 17 -
Figure 2-6 Surface potential decay of LDPE after corona charged under different grid voltages for 2 minutes ..... - 18 -
Figure 2-7 Corona charging current measurement system ..... - 19 -
Figure 2-8 The principle of pulsed electro-acoustic method [21]. ..... - 21 -
Figure 2-9 Sample arrangement details in PEA setup ..... - 22 -
Figure 3-1 Schematic diagram of the conduction, trapping and recombination [73] - 28 -
Figure 3-2 Model for surface charge and space charge distribution immediately after corona charging [74] ..... - 30 -
Figure 3-3 Flow chart of simulation. ..... - 32 -
Figure 3-4 Discretization of the specimen. ..... - 33 -
Figure 3-5a Simulation results with different charging voltages ..... - 34 -
Figure 3-5b Simulation results with different injection barrier heights ..... - 34 -
Figure 3-5c Simulation results with different mobilities ..... - 35 -
Figure 3-5d Simulation results with different trap coefficients ..... - 35 -
Figure 3-5e Simulation results with different trap densities ..... - 36 -

Figure 3-5f Simulation results with different recombination coefficients ..... - 36 -
Figure 4-1 K5000X Sputter coater ..... - 40 -
Figure 4-2 Surface potential decay for aluminium ground and gold ground with different grid voltages ..... - 40 -
Figure 4-3 Surface potential decay rates for aluminium ground and gold ground .... - 41 -
Figure 4-4 Corona charging current for aluminium ground sample and gold ground sample ..... - 43 -
Figure 4-5 Corona charging current ratio versus grid potential for aluminium ground sample and gold ground sample at 2 min ..... - 43 -
Figure 4-6a Space charge distribution for normal ground sample at– 2 kV ..... - 44 -
Figure 4-6b Space charge distribution for normal ground sample at– 4 kV ..... - 45 -
Figure 4-6c Space charge distribution for normal ground sample at– 6 kV ..... - 45 -
Figure 4-6d Space charge distribution for normal ground sample at– 8 kV ..... - 46 -
Figure 4-7a Space charge distribution for gold ground sample at – 2 kV ..... - 46 -
Figure 4-7b Space charge distribution for gold ground sample at – 4 kV ..... - 47 -
Figure 4-7c Space charge distribution for gold ground sample at – 6 kV ..... - 47 -
Figure 4-7d Space charge distribution for gold ground sample at – 8 kV ..... - 48 -
Figure 4-8 Space charge measurement set up for gold ground sample ..... - 48 -
Figure 4-9 Simulation results for aluminium ground sample and gold ground sample- 51 -
Figure 5-1 Surface potential decay for negative polarity and positive polarity ..... - 54 -
Figure 5-2 Corona charging current for negative polarity and positive polarity ..... - 54 -
Figure 5-3a Surface potential decay of LDPE after corona charged under a grid voltage of – 8 kV for different times ..... - 55 -
Figure 5-3b Surface potential decay of LDPE after corona charged under a grid voltage of – 8 kV for different times ..... - 56 -
Figure 5-4a Surface potential decay of LDPE after corona charged under a grid voltage of – 6 kV for different times ..... - 57 -
Figure 5-4b Surface potential decay of LDPE after corona charged under a grid voltage of – 6 kV for different times ..... - 57 -
Figure 5-5a Surface potential decay of LDPE after corona charged under a grid voltage of – 4 kV for different times ..... - 58 -
Figure 5-5b Surface potential decay of LDPE after corona charged under a grid voltage of – 4 kV for different times ..... - 58 -

Figure 5-6a Surface potential decay of LDPE after corona charged under a grid voltage of – 2 kV for different times ..... - 59 -
Figure 5-6b Surface potential decay of LDPE after corona charged under a grid voltage of – 2 kV for different times ..... - 59 -
Figure 5-7a Space charge distribution for − 8 kV with 5 s charging time..... - 60 -
Figure 5-7b Space charge distribution for − 8 kV with 4 min charging time..... - 61 -
Figure 5-7c Space charge distribution for − 8 kV with 10 min charging time ..... - 61 -
Figure 5-8a. Double exponential decay fitting for − 8 kV 5s ..... - 63 -
Figure 5-8b. Double exponential decay fitting for − 8 kV 4 min ..... - 63 -
Figure 5-9a. Parameters A for equation (21) − 8 kV ..... - 64 -
Figure 5-9b. Parameters B for equation (21) − 8 kV ..... - 64 -
Figure 5-10a. Simulation results for different barrier heights with 4 min charging time..- 65 -
Figure 5-10b. Simulation results for different charging times with 1.2 eV injection barrier height..... - 65 -
Figure 5-11a. Trap energy distribution for − 8 kV for different times ..... - 67 -
Figure 5-11b. Trap energy distribution for − 8 kV for different times..... - 68 -
Figure 6-1 Selected experimental results from Figure 4-1. ..... - 70 -
Figure 6-2a Mathematical results for – 2 kV. ..... - 70 -
Figure 6-2b Mathematical results for – 4 kV. ..... - 71 -
Figure 6-2c Mathematical results for – 6 kV. ..... - 71 -
Figure 6-2d Mathematical results for – 8 kV. ..... - 72 -
Figure 6-3 Simulation results..... - 74 -
Figure 6-4a Charge and electric field distribution of corona charged LDPE film during surface potential decay process at – 2 kV. ..... - 76 -
Figure 6-4b Charge and electric field distribution of corona charged LDPE film during surface potential decay process at – 8 kV. ..... - 77 -
Figure 7-1 Surface potential decay of pure PI after corona charged under different grid voltages for 4 minutes..... - 81 -
Figure 7-2 Surface potential decay of 5% nano PI after corona charged under different grid voltages for 4 minutes ..... - 82 -
Figure 7-3 Surface potential decay of 10% nano PI after corona charged under different grid voltages for 4 minutes ..... - 82 -

Figure 7-4 Surface potential decay of 15% nano PI after corona charged under different grid voltages for 4 minutes ..... - 83 -
Figure 7-5 Comparison surface potential decay of all the samples after corona charged under a grid voltage of -2kV for 4 minutes ..... - 83 -
Figure 7-6 Comparison surface potential decay of all the samples after corona charged under a grid voltage of -7kV for 4 minutes ..... - 84 -
Figure 7-7 DC conductivity measurement equipment ..... - 86 -
Figure 7-8 Surface potential decay at -8kV grid potential with 3min charging for low percentage nano-PI ..... - 86 -
Figure 7-9 Currents at 6.5kV for 1 hour for low percentage nano-PI ..... - 87 -
Figure 7-10 Cubic array of spherical nano $TiO_2$ particle of radius r and matrix spacing d. ..... - 88 -
Figure 7-11 Separation distance between two adjacent nano $TiO_2$ particles with increasing volume fraction calculated from equation (22). ..... - 89 -
Figure 7-12 Schematic diagram of interaction zone around nano TiO2 particles. .... - 90 -
Figure 8-1 Needle-Grid electrodes corona charging system ..... - 92 -
Figure 8-2 'FEA mesh' distribution in the model..... - 92 -
Figure 8-3 Picture of the needle..... - 93 -
Figure 8-4 Corona charging system simulation geometry..... - 94 -
Figure 8-5 Current for models I, II and III ..... - 98 -
Figure 8-6 Surface charge densities for models I, II and III at 5 μs ..... - 98 -
Figure 8-7 Electron density plot at 0.6 μs (peak of first impulse current in model I) - 99 -
Figure 8-8 Electric potential distribution along the symmetry axis..... - 100 -
Figure 8-9 Current for models III, IV and V ..... - 100 -
Figure 8-10 Surface charge densities for models III, IV and V at 5 μs ..... - 101 -
Figure 8-11 Logarithm plot of electrons for model III at different times..... - 102 -

# List of Tables

Table 1-1 Parameters of different types of polyethylene [5]. ..... - 3 -
Table 3-1 Tested Simulation Parameters ..... - 37 -
Table 4-1 Simulation Parameters ..... - 50 -
Table 6-1 Parameters for equation (19) ..... - 72 -
Table 6-2 Simulation parameters ..... - 75 -
Table 8-1 Simulation parameters [95] ..... - 95 -
Table 8-2 Boundary conditions for all the models ..... - 96 -
Table 8-3 Model description ..... - 97 -

# Definitions and Abbreviations

## Abbreviations

| | |
|---|---|
| Ac | Alternating current |
| Dc | Direct current |
| HV | High voltage |
| Hz | Hertz |
| kV | Kilovolt |
| PE | Polyethylene |
| LDPE | Low density polyethylene |
| XLPE | Crosslinked polyethylene |
| PEA | Pulsed electroacoustic method |
| LIPP | Laser induced pressure pulse |
| TSM | Thermal step method |
| Al | Aluminium |
| Au | Gold |

## Symbols

| | |
|---|---|
| $E,F$ | Electric field, $Vm^{-1}$ |
| $\rho$ | Net Charge density, $Cm^{-3}$ |
| $\varepsilon$ | Permittivity of dielectric, $Fm^{-1}$ |
| $n$ | Density of mobile species, $Cm^{-3}$ |
| $\mu$ | Mobility of charge carrier, $m^2V^{-1}s^{-1}$ |
| $q, e$ | Electronic charge, C |
| $d$ | Sample thickness, m |
| $\sigma$ | Conductivity, $Sm^{-1}$ |

| | |
|---|---|
| $\sigma 1, \sigma 2$ | Density of surface charge, $Cm^{-2}$ |
| $J, j$ | Current density, $Amm^{-2}$ |
| $A$ | Richardson constant, $A = 1.2 \times 10^{6} Am^{-1} K^{-2}$ |
| $kB$ | Boltzmann constant, $k=1.38 \times 10^{-23} m^{2}kgs^{-2}K^{-1}$ |

# Publications

G Chen, T J Sadipe, Y Zhuang, C Zhang and G C Stevens, *"Conduction in Linear Low Density Polyethylene Nanodielectric Materials"*, The 9th International Conference on Properties and Applications of Dielectric Materials, 19-23 July 2009, Harbin, China, pp. 845-848

G Chen, J Zhao and Y Zhuang, *"Numerical Modeling of Surface Potential Decay of Corona Charged Polymeric Material"*, IEEE International Conference on Solid Dielectrics, 4-9 July, 2010, Potsdam, Germany, pp. 549-552

J Zha, G Chen, Y Zhuang and Z Dang, *"Novel surface potential decay of $TiO_2$-based polyimide nanocomposite films"*, Annual Report Conference on Electrical Insulation and Dielectric Phenomena, 17-20 October 2010, Purdue University, West Lafayette, Indiana, USA, pp. 26-29

Y Zhuang, G Chen and M Rotaru, *"Numerical modelling of needle-grid electrodes for negative surface corona charging system"*, Journal of Physics: Conference Series, 310. 012011. ISSN 1742-6596

Y Zhuang, G Chen and M Rotaru, *"Charge injection in gold ground electrode corona charged polyethylene film: surface potential decay and corona charging current measurement"*, 14th International Symposium on Electrets, 28-31 August 2011, Montpellier, France, pp. 127-128

Y Zhuang, G Chen and M Rotaru, *"Charge injection in gold ground electrode corona charged polyethylene film: Numerical simulation on surface potential decay"*, 14th International Symposium on Electrets, 28-31 August 2011, Montpellier, France, pp. 129-130

Y Zhuang, J Zha and G Chen, *"Surface potential decay and DC conductivity of $TiO_2$-based polyimide nanocomposite films"*, 14th International Symposium on Electrets, 28-31 August 2011, Montpellier, France, pp. 169-170

Y Zhuang, G Chen, P H Chappell and M Rotaru, *"Surface Potential Decay: Effect of Different Corona Charging Times"*, 2012 IEEE Conference on Electrical Insulation and Dielectric Phenomena, Montreal, Canada, 14 - 17 Oct 2012, pp. 620-623

Y Zhuang, G Chen and M Rotaru, *"Charge Injection from Aluminium and Gold Ground Electrode of Corona Charged Polyethylene Film"*, Journal of Electrostatics (Submitted)

Y Zhuang, G Chen, M Rotaru and P H Chappell, *"Simulation of surface potential decay using bipolar charge transport model"*, IEEE Transactions on Dielectrics and Electrical Insulation (Submitted)

# Acknowledgements

I would like to say a big Thank You to my supervisor Prof. George Chen, and co-supervisor Dr. Mihai Rotaru. They have shown their great patience and understanding to my case. They also provide invaluable enlightenment of this study and to firm the confidence and determination for me to complete the project.

My thanks also go to my colleagues in EPE group especially Dr. Junwei Zhao as he did not hesitate to answer my questions every time I visit him and Dr. Junwei Zha who provided the nano materials he made in China.

Finally, I would like to thank my family for the invaluable continual moral support.

# Chapter 1 Introduction

## 1.1 Underground power cables

As the number of high voltage technologies in use increases, the demand of overhead lines and underground power cables transmission systems have been rising around the world. From technical and economical point of view, it can be said that overhead lines option is heavily favoured. For example, only about 1% underground transmission lines were used in 1980's in US, and most of these are in the major urban centres. The first reason is overhead lines have typically 6 to 20 times less cost on installation and manufacturing and the second relates to the thermal limited and fault detection [1]. However, in the past few decades, due to the large number of population growth in urban and suburban areas and special requirements such as water crossing, airports, under highways and nature aesthetic environment factors, installation of overhead lines became more expensive and in some case it becomes impossible [2]. Therefore, mixture of the overhead and underground power transmission circuit is more popular, which improves the position of underground transmission.

The cable is an insulated conductor. Power cables are classified according to their types of insulation. Paper insulation was the first insulation tried on the first underground transmission line connecting a generating station outside London with the city centre in

the 1880's by Sebastian de Ferranti. The old jute or rubber insulations proved to be unsuitable for 10kV, 50Hz transmission. Paper had been used as insulation in the telephone cables, and Ferranti found that by impregnating it with ozokerite, a by-product of the manufacture of candle wax; it could withstand very high voltage [3]. Cables for power transmission and distribution are composed of many different types of insulation, conductors and sheathing materials. Cable capacitance is very dependent on the dielectric constant of the cable insulation. There are basically three types of cable insulation: tape insulation, solid insulation and gas insulation. The principal tape insulation is oil-impregnated cellulose paper. It exists in two categories, self-contained oil-filled (OF) cables and pipe-type OF (POF) cables. Solid insulation is usually extruded onto the conductor; it contains polyethylene (PE), cross-linked polyethylene (XLPE), butyl rubber, ethylene-propylene copolymer, etc. Gas insulation is normally referring to compressed $SF_6$ gas, which is most appealing for long distance cable because the dielectric constant is minimal and the dielectric dissipation factor is virtually zero. Insulation thickness of a power cable is determined by recognizing that it must withstand not only the steady state AC voltage but also transient lightning impulses and switching surge voltages. The conductor shield is provided to prevent any corona discharge between the conductor and the insulation and therefore is required to make good contact with the insulation [1].

## 1.2 Polyethylene

Polyethylene has been widely used as an insulator and its properties have been studied throughout. Therefore, most experimental work in this thesis will be carried out using polyethylene. Polyethylene exhibits excellent electrical properties such as lower dielectric loss, high volume resistivity and high breakdown strength; hence it becomes one of the most ideal cable insulation materials. High density polyethylene is produced by polymerizing ethylene gas into the material at a relatively low pressure (1 to 100 atm). Low density polyethylene is polymerized thermally under a pressure as high as 1000 to 2000 atm [1]. Most of the synthetic high polymers are organic compounds consisting of long, chain-like molecules where repeated molecular units are linked by covalent bonds. The process of polymerization in which small molecules of the starting material, the monomer, undergo chemical reaction together to form long chains may

proceed in a variety of ways. These may be divided into two principal categories, addition and condensation polymerization, which have major structural implications for the final product. The formation of polyethylene involves thousands of ethylene molecules bonding together to form a chain of repeating -$CH_2$- units as shown in Figure 1-1:

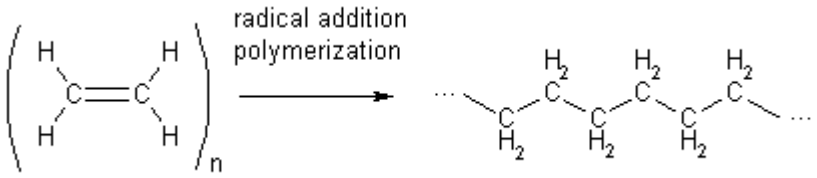


Figure 1-1 Polymerization of ethylene to polyethylene [4].

There are varying types of polyethylene with different properties, Table 1-1 shows the details for low density polyethylene (LDPE), high density polyethylene (HDPE), linear low density polyethylene (LLDPE) and cross-linked polyethylene (XLPE).

Table 1-1 Parameters of different types of polyethylene [5].

| Property | | HDPE | LLDPE | LDPE | XLPE |
|---|---|---|---|---|---|
| Breakdown Strength $E_B$ | kV/mm | 100 | 75 | 75 | 50 |
| Dielectric Constant $\varepsilon_r$ | | 2.3 | 2.3 | 2.2 | 2.4 |
| Volume Resistivity $\rho$ | Ω · cm | $5x10^{17}$ | $5x10^{17}$ | $5x10^{17}$ | $10^{16}$ |
| Dielectric Loss tan $\delta$ | (1 MHz) | $10^{-3}$ | $10^{-3}$ | $2x10^{-4}$ | $10^{-3}$ |
| Crystallinity | % | 80-95 | 70-80 | 55-65 | -- |
| Density | $g/cm^3$ | 0.95 | 0.93 | 0.92 | 0.92 |
| Melting Point | ℃ | 130 | 120 | 110 | -- |
| Tensile Strength | MPa | 25 | 15 | 13 | 31 |

LDPE has a high degree of the short and long chain branching, which means that the chains do not pack into the crystal structure as well. It has, therefore, less strong intermolecular forces as the instantaneous-dipole induced-dipole attraction is fewer. This results in a lower tensile strength and increased ductility. LDPE is created by free radical polymerization. The high degree of branching with long chains gives molten

LDPE unique and desirable flow properties. LDPE is used for both rigid containers and plastic film applications such as the plastic bags and film wrap [6].

HDPE has a low degree of branching and thus has a strong intermolecular forces and tensile strength. HDPE can be produced by chromium/silica catalysts, Ziegler-Natta catalysts or metallocene catalysts. The lack of branching is ensured by an appropriate choice of catalyst (for example, chromium catalysts or Ziegler-Natta catalysts) and reaction conditions. HDPE is used in products and packaging such as milk jugs, detergent bottles, margarine tubs, garbage containers and water pipes [6].

LLDPE is a substantially linear polymer with significant numbers of short branches, commonly made by copolymerization of ethylene with short-chain alpha-olefins (for example, 1-butene, 1-hexene and 1-octene). LLDPE has higher tensile strength than LDPE, it exhibits higher impact and puncture resistance than LDPE. In general, LLDPE is produced at lower temperatures and pressures by copolymerization of ethylene and such higher alpha-olefins. The copolymerization process produces an LLDPE polymer that has a narrower molecular weight distribution than conventional LDPE and in combination with the linear structure, significantly different rheological properties. LLDPE is used in packaging, particularly film for bags and sheets. While other applications are available, LLDPE is used predominantly in film applications due to its toughness, flexibility and relative transparency [6].

XLPE is a three-dimensional, net-structured polyethylene with inter-molecular bridges. It can be cross-linked by irradiation or by chemical reaction. Cross-linking polyethylene endows it with additional improved performance with respect to thermal deformation, thermal aging and environment stress cracking, while retaining almost all the characteristics of permittivity, dissipation factor and breakdown strength, as in comparison to regular polyethylene. XLPE is a very popular material used on cable insulation [1].

## 1.3 Charge Transport

### *1.3.1 Charge transport in metal, semiconductor and insulator*

The electrical property of metal is to conduct electric current very well; on the other hand, insulator is designed not to conduct any electric current at all. Figure 1-2 shows the energy diagram for metal, semiconductor and insulator. Initially, the full valence band contains electrons and the conduction band is empty; at this stage, there is no electric current through the material. It can be seen that from the band diagram for metal, the band structure is a valence band either just touching or overlapping the overlying empty conduction band. Even a small electric field applied to the metal will energize the electrons moving from the valence band to the conduction band hence an electric current will appear. For semiconductor and insulator, an energy gap is sitting between the valence band and the conduction band and the energy gap is larger (> 4 eV) in insulator. The energy gap is the difference in energy between the top of the valence band and the bottom of the conduction band, the unit of the energy gap is defined in electron-volts (eV), this is the energy that must be supplied to an electron so that it can across the forbidden energy gap to become a conduction electron [7]. For example, silicon with the band gap of 1.11 eV at 300 K and PE is 8.8 eV at 300 K [8]. It is highly important to measure the band gap energy for semiconductors and insulators. The band gap energy can be measured in several different ways such as UV/Vis/NIR Spectrometer [9].

If energy is supplied to take an electron from the valence band, across the energy gap, up into the conduction band, then the electron that has made it to the conduction band is now available for conduction. In addition, there is now a vacant electron energy state left in the valence band. This vacant state is called a ‘hole’ and it behaves like a positive charge carrier with the same magnitude of charge as the electron, but opposite sign. The hole in the valence band is able to carry current in just the same way as an electron in the conduction band, except that the hole has a positive charge. The hole is not a free particle, it can only exist within a solid where there is an electron missing from an otherwise full band. However, in most of the metals, the electron promoted to the conduction band does not leave a hole for conduction in the valence band as another electron will immediately fill the blank [7].

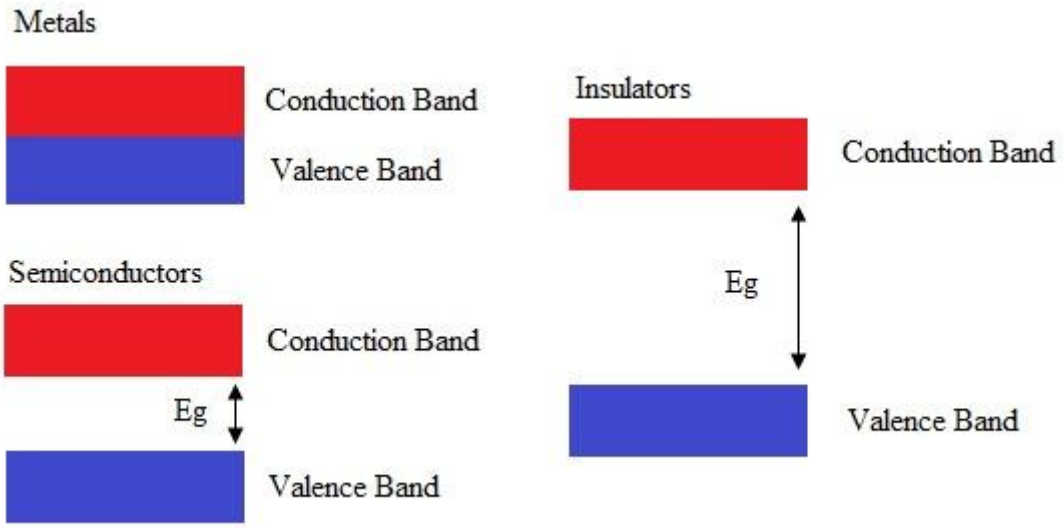


Figure 1-2 Energy band diagram for metals, semiconductors and insulators.

### *1.3.2 Traps in Polymer*

The electrical property of crystalline insulating materials can be described by an energy band diagram described in the last section. Polyethylene is a typical semi-crystalline material; it may contain additives (e.g. antioxidants) and impurities (e.g. oxidized groups), therefore, the real band structure is significantly different from the ideal one which has a large band gap and no localized states. Disorder in the polyethylene comes from chemical or structural nature, it modifies the degenerate states of the valence and conduction bands and forms localized states in the forbidden gap. These localized states are accessible either to electrons or holes depending on their distance in energy to the valence and conduction bands. The band gap for polyethylene crystals has been estimated to be 8.8 eV [10]. The disorder produces localized states at the edge of both bands, with depth in the range 0.15–0.3 eV. This is called physical trap, and it is defined as shallow trapping centres. The residence times of carriers within these sites are of the order of $10^{-12}$ s [11]. Therefore, it can be considered as local conduction sites and do not contribute to long-`lasting trapping of charges. Besides, chemical defects like hydroxyl or ketone functions or double bonds act as deeper sites for carriers. Chemical disorder

introduces deeper energy levels in the range 0.4–1.5 eV for both electrons and holes [12]. Some of these centres then act as deep trapping centres and the residence time for carriers is virtually infinite. Therefore, traps in polymer can affect the charge transport inside the material and it will be deeply discussed in next few chapters. A schematic representation of these energy levels is given in Figure 1-3.

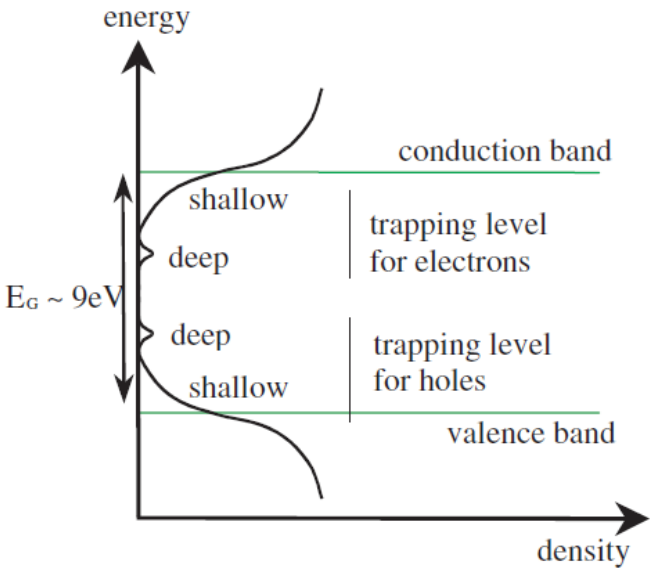


Figure 1-3 Schematic representation of state density in a disordered dielectric material. Shallow and deep traps are related to physical and chemical disorder, respectively [13].

## 1.4 Research aims and objectives

The general objectives of the present research are as the follows:

1. Using basic corona charge system to observe the cross-over phenomenon for the sample, i.e. the potential of sample with an initial high surface potential decays faster than that with an initial lower surface potential. (Chapter 2)

2. Understanding how parameters in bipolar charge transport model affect the final results. (Chapter 3)

3. Comparing the surface potential decay results for the aluminium ground LDPE with gold ground LDPE. Also using corona charging current, space charge measurement

methods and numerical model to explain the effect of different grounds on the surface potential decay. (Chapter 4)

4. Measuring the effect of different charging polarities and different charging times to the surface potential decay results. (Chapter 5)

5. A numerical model was built based on bipolar charge injection method that was observed from the experimental results. (Chapter 6)

6. Using the surface potential decay method to examine some unknown materials insulation property (nano-polyimide). Comparing the results to the DC conductivity results. (Chapter 7)

7. Establishing a model based on gas discharge process using COMSOL to understand the corona charging process. (Chapter 8)

## 1.5 Contributions

This thesis contributes to the understanding of charge transport under corona charge polymeric insulation materials through experimental investigation and theoretical modelling work. To understand the physical reason of the cross-over phenomenon that had been studied for a few decades, experiments on the effect of the ground electrode were carried out initially. The experiments contain surface potential decay measurements, corona charging current measurements and space charge measurements. After confirming that the bipolar charge injection is involved during the corona charging and potential decaying process, the dynamics of surface potential decay in corona charged polyethylene is simulated using the bipolar charge transport model, which includes charge injection, charge transport with trapping and combination processes. The simulation can clearly tell us the influence of charge injection, charge mobility together with the trapping and recombination dynamics which cannot be observed experimentally at the moment.

A special phenomenon of effect of different corona charging time was also observed. To extend the charging time up to 10 min, it is found that rate of surface potential decay

do not change with the charging time consequently. Space charge measurements and a mathematical analysis were involved to find out the reason behind it. As nano-materials become more and more popular recently, attempts on examining nano-polyimide materials using surface potential decay measurements had also been carried out. Finally, a gas discharge model was built in COMSOL to understand the corona charging process and the structure of the corona charging system.

# Chapter 2 Surface Potential Decay and Experimental Setup

## 2.1 Background

### *2.1.1 Previous work review*

The study of surface potential decay in dielectric materials has a long history and is closely related to the wide application of corona charged dielectrics. It became a particularly popular topic after the cross-over phenomenon for surface potential decay was found in 1967 [14].

Figure 2-1 shows the cross-over phenomenon observed by Ieda [14]. It shows that a sample with an initial high surface potential decays faster than that with an initial lower surface potential. In order to understand the physics behind it, many assumptions and hypothesis have been made to explain this phenomenon. Generally, there are four possible mechanisms that have been discussed in relation to their effects on the surface potential decay processes: gas neutralization, surface conduction, sample polarization and charge injection [15]. Most hypotheses believe that the effect of gas neutralization

and surface conduction can only be applied in some special circumstances like very thick materials (about 1 mm) and neglected in conventional conditions; the sample polarization is also negligible if the charging period is long enough [16-20]. The deep trap on the surface and shallow trap in the material was used to qualitatively explain the cross-over phenomenon; when corona discharge charged the polymer, the surface of the film is at a high potential and electrons travel across the deep trap easily due to its higher energy, therefore, electric charge on the surface decays faster. If the film is less charged by corona discharge, and the surface is at a low potential, then the electron with less total energy cannot travel across the deep trap easily [21].

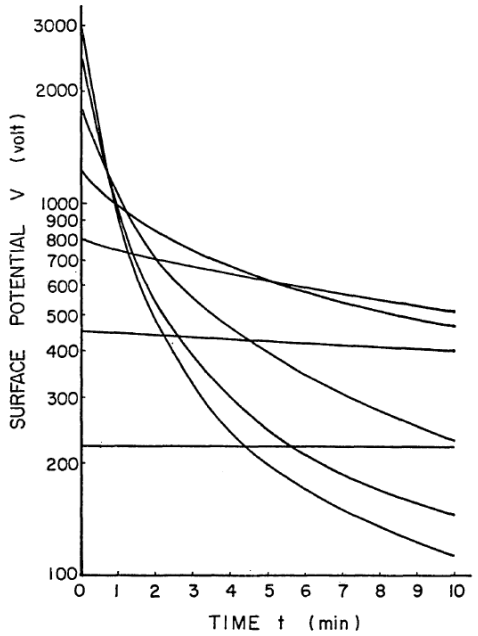


Figure 2-1 The decaying curves of positive charge on the polyethylene film of 0.015mm thick with a little amount of surface active agent [14].

### *2.1.2 Application of the potential decay research*

First application of corona discharge is electro-optics. Since 1950, the design of photocopiers and laser printers led to most of the research on corona charging, charge injection mechanisms and surface potential decay dynamics, especially on photoconductive insulators [22-25]. They had taken semiconductor physics as a starting point. The decrease of the potential due to transport mechanisms in a disordered material has been modelled in detail, by introducing trapping, which led to the dispersive transport models and the thermodynamic models [26]. The surface potential

decay dynamics were also studied in electrets area. The possibility to store charges on the surface of sample for a long time in insulating materials has been used to develop many electrets-based devices. However, the research focus of these researchers is from an opposite point. They are interested in how to improve the time stability of the charge. Their work shows that the researches concentrated on the topic of charge build-up and charge trapping in the material, rather than on decay models [27-33]. Recently, surface potential decay measurement is widely used in the space industry, especially for satellite designers and manufacturers to understand the charging and discharging behaviour of insulating materials [34-38], several studies on the potential decay after electron beam charging were also carried out [39-47].

One of the popular materials used in the earlier corona research is low density polyethylene. In addition, low density polyethylene has been widely used as insulating material for power cables. Both surface charge and space charge play an important role in DC insulation, but the behaviour is very complicated and not well known yet. The charge dynamics strongly depend on properties of dielectric materials and the electrode conditions. To understand the electric carries situation in the LDPE film under the conditions of corona discharge, a numerical model is necessary to obtain information that cannot be directly observed from experiments.

### *2.1.3 Measurements of electrostatic potentials*

There are several possible ways to measure surface potential by not contacting the sample surface. Kelvin probe, field mill and electrostatic probe are the most popular methods to measure surface potential of the sample with one side grounded. They are briefly described below:

i) Kelvin probe: It is a non-contact, non-destructive vibrating capacitor device used to measure the work function of conducting materials or surface potential of semiconductor or insulating surfaces. The probe vibrates in the direction perpendicular to the tested surface and the current flowing to and from the probe changes proportionally to the amplitude and frequency of that vibration. The probe tip is typically 0.2 – 2.0 mm away from the sample.

However, this is a truly sensitive instrument and the results can be affected by electromagnetic and mechanical noise produced by wires, external electric fields, piezoelectric effects and mechanical parts [48].

ii) Field mill: The field mill principle is based on electrostatic induction. It consists of one or more electrodes which are periodically exposed to and then shielded from the field by a grounded, rotating shutter. The induced charge on the sensing electrode and the current between the sensing electrode and ground are both proportional to the strength of the electric field [49]. Because of the induced charge, the measurement result on field mill is changed by the distance between the instrument and the sample surface; therefore, it needs to be calibrated before use. Figure 2-2 shows the schematic representation of the field mill.

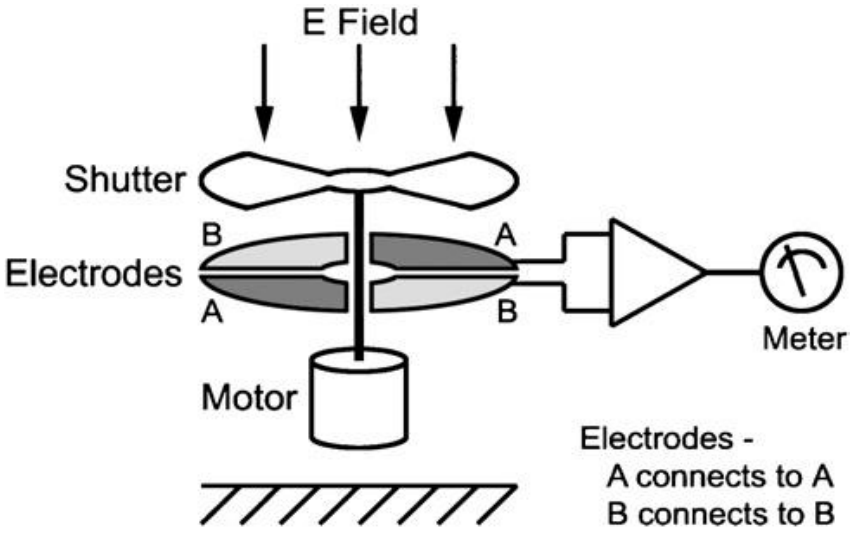


Figure 2-2 Schematic diagram of the field mill [50]

iii) Electrostatic probe: This is also called feedback-null surface potential monitors or non-contact voltmeters. It solves the problem of non-contact measurements by means of a control loop and an integrated high voltage source driving the probe potential in order to cancel the electric field between the surface and the probe. Therefore, this instrument can directly measure the surface potential [51].

It can be found that kelvin probe is the most accuracy tool to measure the surface potential; however, it needs an extremely good environment condition to work precisely and the cost is much higher than the others. Although the electrostatic probe can also directly measure the surface potential, the measurable range is low (less than $\pm$ 5 kV).

The field mill electrostatic monitor has been selected in our experimental system due to its low cost and wide measurable range.

### *2.1.4 Corona discharge*

In order to create charges on insulator's surface, several ways of charging the material can be used. In our laboratory, corona discharge from a needle electrode had been selected. A corona discharge is sustained non-thermal plasma which occurs in close vicinity to a thin discharge electrode, such as a pin or a wire, at a high potential. Coronas may be either positive or negative, depending on the polarity of the electrode. One feature common to both positive and negative corona is the formation of an electron avalanche. Such an avalanche occurs when a strong electric field acts on naturally occurring free electrons in the air. The electric field accelerates these electrons so that they gain sufficient kinetic energy to cause ionisation when they collide with neutral gas molecules in their path. Additional electrons are liberated during these collisions, which after acceleration are also able to ionise. As the process continues more and more electrons are liberated and an avalanche rapidly builds up. In this way, a small number of seed electrons can cause ionisation of an entire gas and turn it into plasma. In a positive corona, the avalanche electrons are drawn towards the electrode while the resultant positive ions are repelled. In a negative corona, the avalanche is in the opposite direction, with the electrons repelled and the positive ions drawn to the electrode. In a positive corona the electrons accelerate as the avalanche progresses, while in a negative corona they decelerate as they travel away from the electrode [52].

## 2.2 Surface Potential Decay Experimental Details

The samples used for the decay experiments are low density polyethylene (LDPE) film with 50 μm thickness. The film was purchased commercially from GoodFellow. Additive-free LDPE was selected to avoid extra complications that may arise from the presence of antioxidants and other additives. The film was cut into a circular disc with a diameter of 55 mm, cleaned initially using methanol, rinsed in deionized water and then dried in air. The LDPE film was negatively charged in the needle-grid corona charging

system as shown in Figure 2-3. The needle electrode is 3 cm away from the top surface of earth plate. It always has a relatively high voltage to generate corona discharge. The grid electrode is 1.5 cm away from the top surface of earth plate. It was used to control the surface potential of the tested samples and achieve a uniformly distributed potential along the whole surface of the sample. The grid potential is influenced by the needle potential. If the grid potential is selected too low, then its value will be controlled by the needle potential instead of the voltage source connected to the grid. As the gap between the grid electrode and the sample is large, the decay starts at 63% of the applied grid voltage due to the gap between the grid electrode and the material. All the results shown in this thesis were referenced by the grid electrode voltage to avoid any misunderstanding. After the charging voltage has been set up, the sample will be charged under the grid electrode for a fixed charging time. It has been reported that temperature and humidity can also affect the surface potential decay results [53, 54]. Therefore, to achieve consistent results, all experiments were carried out in a controlled environment where temperature and relative humidity were kept at 23 ℃ and 20% respectively.

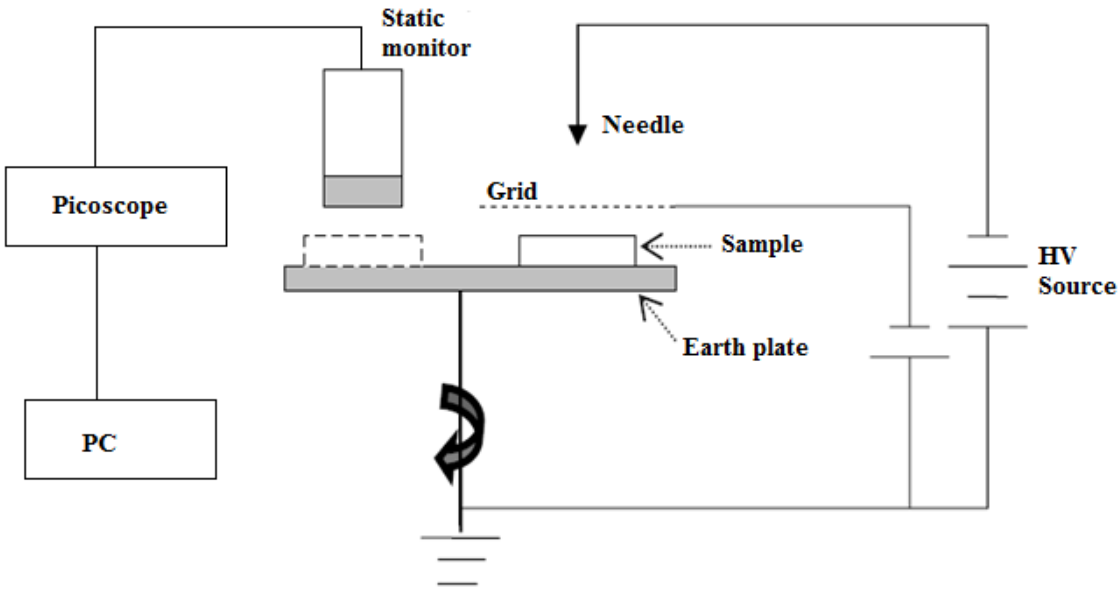


Figure 2-3 Surface potential decay measurement system

Once charged, the sample was transferred quickly to a compact JCI 140 static monitor to observe the isothermal surface potential decay. The JCI 140 is a device that follows the field mill principle described above. The time required to transfer the sample is

around 1 s, and the first decay reading is taken at 5 s after the charging due to the delay in data transfer from the monitor to PC.

The readings from the static monitor are not direct values of the surface potential. To convert the readings into the surface potentials, a calibration needs to be carried out. From the user manual of JCI 140 static monitor, the measuring range of the device can be set by 2 different switches. Due to the extremely high voltage processes in these experiments, all measurements will be done on stage '2', which represents a range between 0 to $\pm$ 20 kV. However, the static monitor's sensitivity is changing by varies separation distance from the sample surface as a graph shown in Figure 2-4.

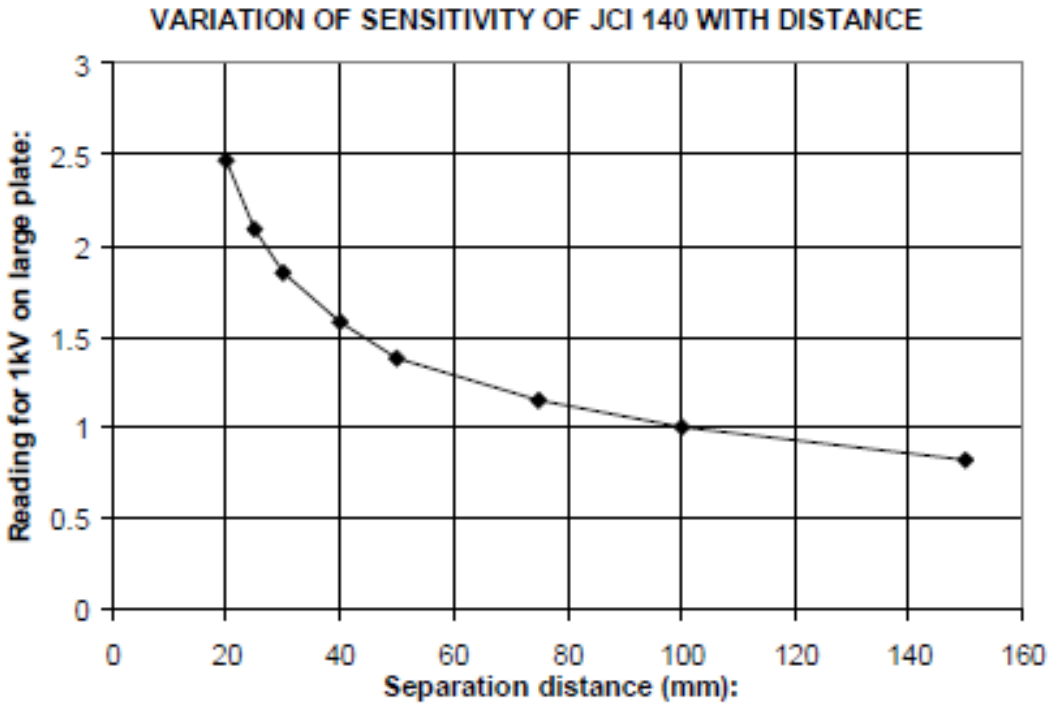


Figure 2-4 The sensitivity varies with separation distance from surfaces for JCI 140 static monitor [55]

From Figure 2-4, it can be seen that when the separation distance between the static monitor's probe and the sample surface is 100 mm, the static monitor can give the actual readings. However, if the separation distance is high, the results can be disturbed by the ions and electrons in the air or any experiment equipment. To avoid the static monitor taking the reading from the electrodes (which both have relative high voltage and a decay process on the probe), a metal plate is inserted in the middle of the static

monitor and the grids. The calibration is done by using a thin aluminium foil, which has the same size and shape as the measured samples with a small tail to connect with a high voltage source placed on top of a LDPE sample. For a LDPE sample with thickness 100 μm and less, sparks had been observed when the applied voltage exceeded – 3.5 kV, therefore, the full calibration process is done by using an 180 μm thickness LDPE sample. The distance between the probe head and the surface of the sample was set to 3 cm.

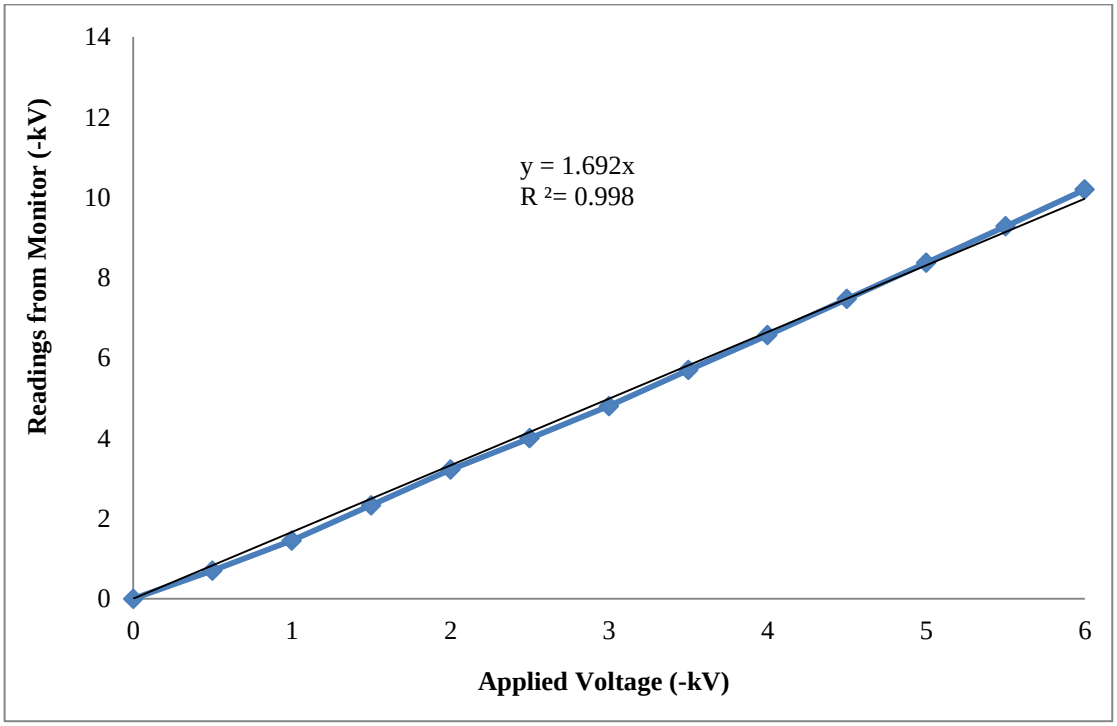


Figure 2-5 Calibration of current experiment measurement system

In the present case, a linear relationship with $R^2$=0.998 is obtained between the readings and true voltage as shown in Figure 2-5. Therefore, according to the formula shown in Figure 2-5, the surface potential on the LDPE film can be evaluated by using the readings from the static monitor divided by a factor of 1.692. Of course, the slope in the linear relationship will change with the geometry of the experimental settings. However the thickness of the gold is negligible; hence the surface potential from the films with gold electrode can be measured using the same calibration.

## 2.3 The cross-over phenomenon

The first step of this project is to successfully observe the cross-over phenomenon by measuring the surface potential decay on corona charged LDPE sample. It has been reported that negative charge are easier to get cross-over than positive charge, and if the charging time was too low the cross-over phenomenon cannot be observed [18]. Therefore, the charging time was fixed at 2 min with various charging voltages from – 1 kV to – 9 kV grid potential. All the experimental results presented in the thesis were operated at least 10 times per results to check the repeatability.

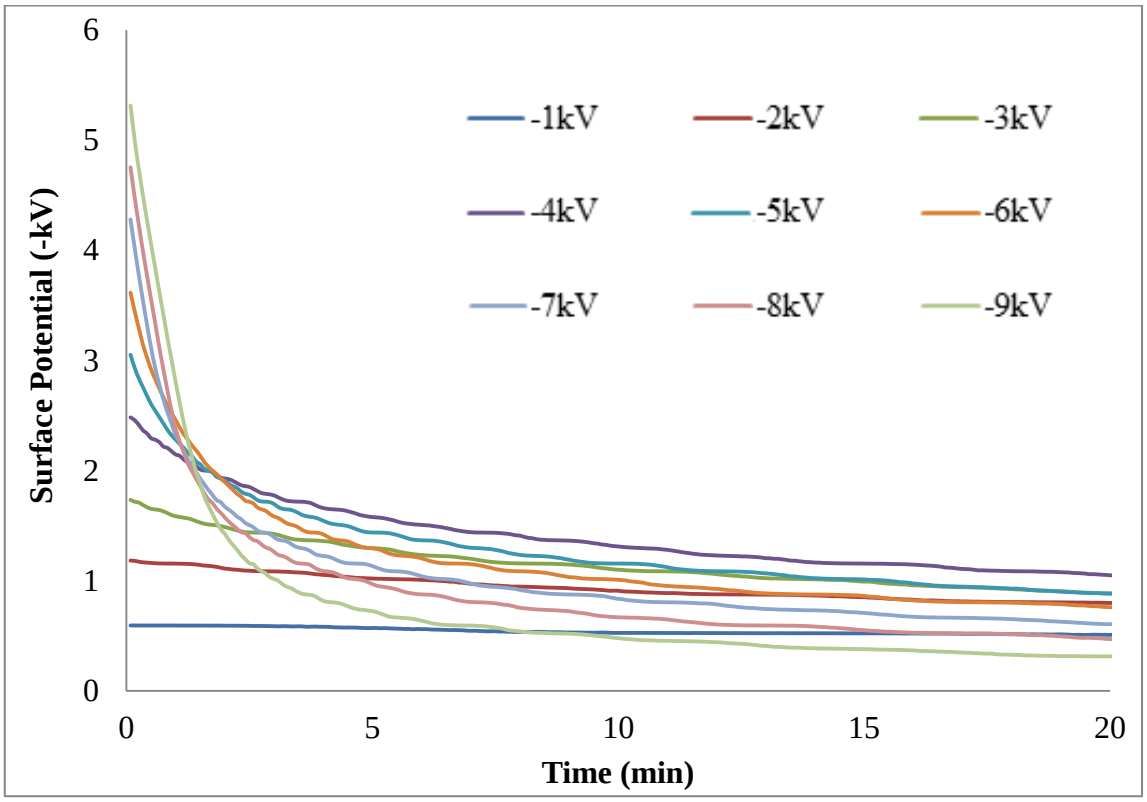


Figure 2-6 Surface potential decay of LDPE after corona charged under different grid voltages for 2 minutes

Figure 2-6 shows the results on surface potential decay from – 1 kV to – 9 kV. It can be seen that below – 4 kV, there is no cross-over phenomenon over a period of 20 minutes observation. However, it can be still clearly observed that the higher initial surface potential leads to a faster decay. When the grid voltage is equal to or higher than – 5 kV, the cross-over phenomenon can be clearly seen. For – 8 kV and – 9 kV results, the decay tails can even cross the – 1 kV decay curve within 20 min. These results proved

the cross-over phenomenon that had been observed by other researchers and the electric field range is much wider than those reported results. As corona charging voltage is the only experimental condition that was changed during the experiments, it is also known that charge injection and charge transport inside the bulk can be affected by the electric field; therefore, our research will focus on explaining the cross-over phenomenon based on charge injection and charge transport.

## 2.4 Experimental details of corona charging current measurement and space charge measurement

### *2.4.1 Corona charging current measurement*

The corona charging current was measured with a slight modification on the existing system as shown in Figure 2-7. Considering the large size of the grid electrode (9 cm × 4.5 cm), the corona charging current was measured by using a 10 cm diameter LDPE. As the charging current is in nano size, it was determined by measuring the voltage across a 10 MΩ resistor.

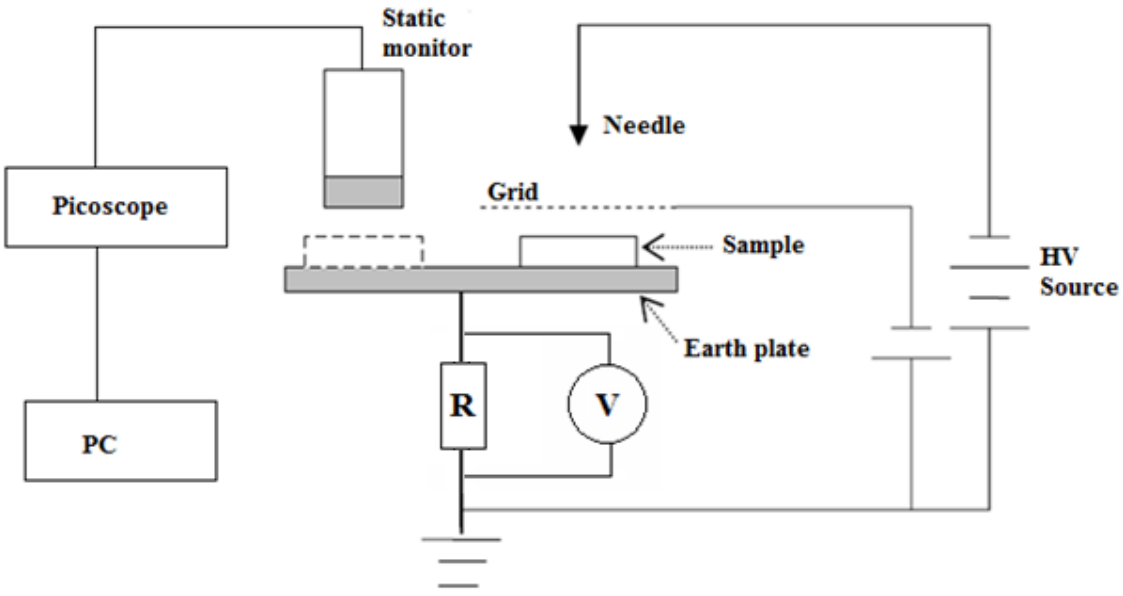


Figure 2-7 Corona charging current measurement system

### *2.4.2 Space charge measurement -- Pulsed Electro-acoustic Method (PEA)*

To understand how the corona charged film decays, not only does the charge injection along the surface need to be studied, but also knowledge on the charge distribution inside the polymer film is required. Over the last 20 years, there has been significant development in space charge mapping in solid dielectrics due to the advances in sensors, signal capture and processing. Techniques such as the laser-induced pressure pulse method (LIPP) [56], thermal step method (TS) [57] and pulsed electroacoustic method (PEA) [58] have been used to study in the field of space charge measurement. They have provided significant assistance in the understanding of charge injection, charge transport and trapping (de-trapping) in dielectric materials.

The PEA method was first developed by Maeno, Takada and co-workers in 1980s [59] and it is now widely used in mapping the charge distribution, charge injection and transport in solid dielectrics around the world. Figure 2-8 shows the principle of PEA measurement. When a high voltage pulse of 5 ns length is applied to the sample sandwiched between the two electrodes, the pulse electric field interacts with the charges on the electrodes as well as the accumulated space charges in the specimen, resulting in the movement of charges that generates acoustic waves. The acoustic wave produced corresponds to each charge layer. The waves are then transmitted to the bottom electrode and detected by the piezoelectric transducer. The waves are converted into an electrical signal by the transducer, amplified and finally captured with a digital oscilloscope.

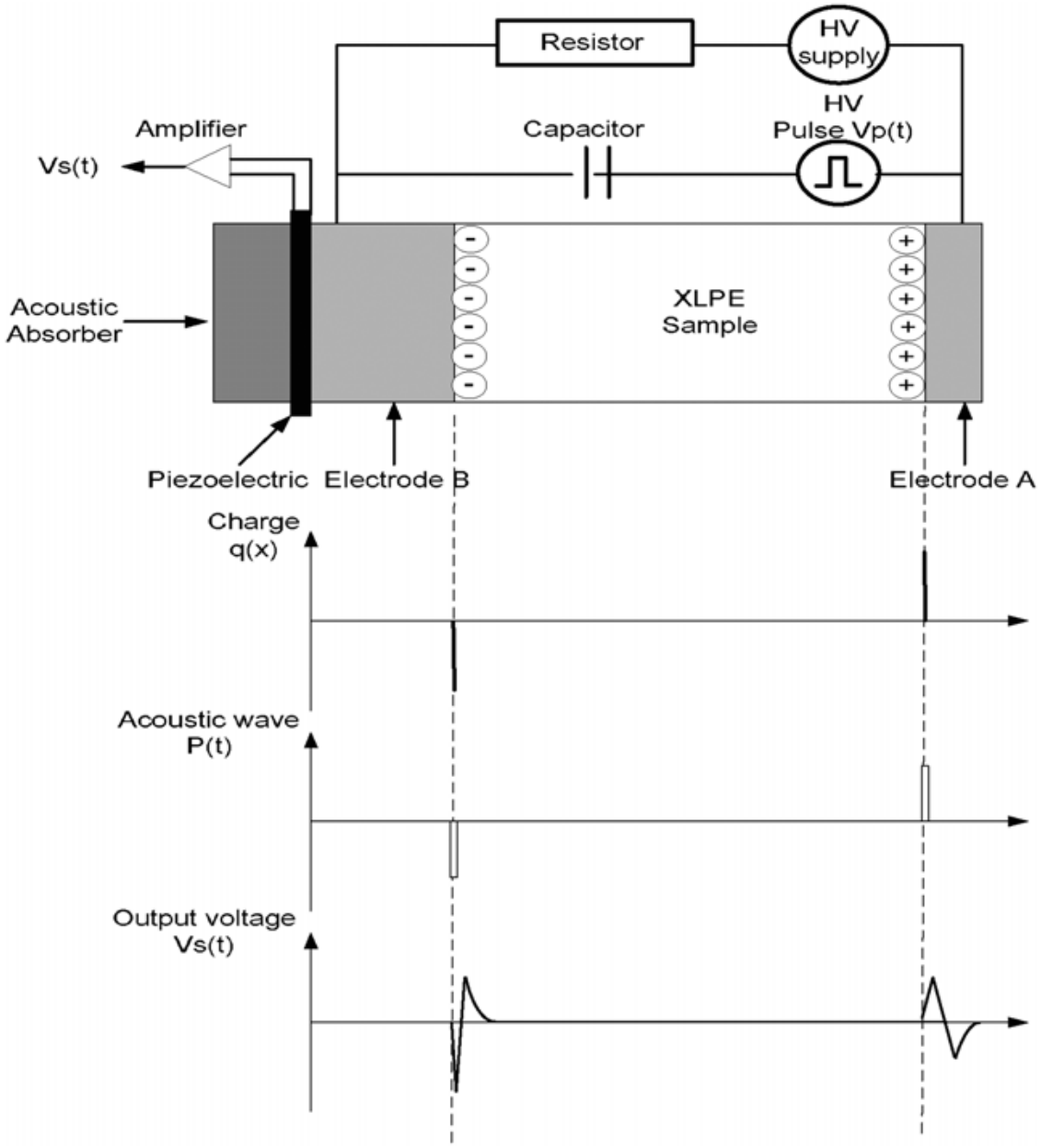


Figure 2-8 The principle of pulsed electro-acoustic method [21].

The electric signal obtained in the time domain represents the charge distribution is:

$$V_s(t) = K[\sigma_1 + \sigma_2 + v_{sa}\Delta T\rho]e_p \quad (1)$$

where $\sigma_1$ and $\sigma_2$ are the surface charges at the electrodes, $v_{sa}$ is the sound velocity through the material, $\Delta T$ is the width of the pulse, $\rho$ is the bulk charge and $e_p$ is the amplitude of the pulsed voltage. The quantitative charge analysis needs $K$ to be calibrated, and this is typically done by applying 1 kV across the sample to generate a known charge density on the two surfaces at the electrodes [50].

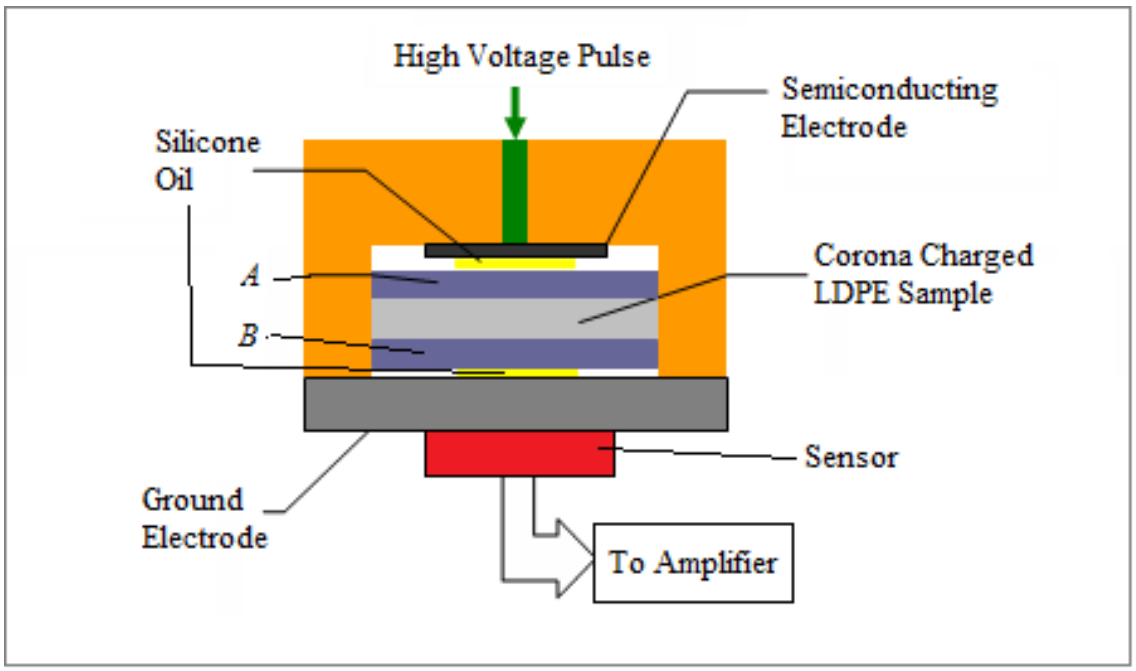


Figure 2-9 Sample arrangement details in PEA setup

The space charge distribution in the corona charged LDPE film was measured by this PEA technique. This technique is widely used due to its simple structure, low cost and ease of implementation. After the LDPE film was corona charged for 2 min in the corona charging system, it was carefully removed by using a pair of insulated head tweezers. To protect the charges on both side of the sample, it needs to be sandwiched by two additional 50 μm thick clean LDPE films *A* and *B*. The typical experimental procedure is described as follows: (i) place film *B* on the aluminium plate in the PEA system, (ii) transfer the corona charged film and put it on top of film *B*, and (iii) finally place film *A* on top of the corona charged sample before mounting the PEA head. The whole process takes about one minute before the first PEA measurement can be carried out. Figure 2-9 shows the setup of PEA measurement. A very thin layer of silicone oil is often smeared on the electrodes to improve acoustic coupling.

# Chapter 3 A New Model on Surface Potential Decay

## 3.1 Existing Models

The study of the potential decay in dielectric materials has a long history and is closely related to the wide application of corona charged dielectrics. One of the interesting observations associated with surface potential decay is the cross-over phenomenon, which was firstly reported by Ieda in 1967 [14]. His results showed that in particular circumstances, polyethylene potential decay curves with several initial charge levels crossed each other (see Figure 2-1). However, the reason behind that was not satisfactorily explained. This crossover phenomenon has been studied in many works and excited theoreticians imagination. Many models about the potential decay have been published, but no direct experimental observation to support the assumptions made in the establishment of the models.

Batra et al [60, 61] came out a mathematical model based on photo insulators and successfully proved the value of hole mobility. This one-dimensional time-dependent model contains the law of conduction, the continuity equation, Poisson's equation and

the total current density. The effect of partial instantaneous injection and trapping was not taken into account in the model but still came out with few qualitative discussions. At the same time, Wintle [17, 62, 63] developed a model that was based on transient space charge limited current conditions. The analytic results were given for the following cases: (a) mobility proportional to a power of the field; (b) mobility proportional to a power of the free-carrier concentration, and (c) deep trapping. It was assumed that after one transit time, the surface voltage becomes a unique function of time, independent of its initial value. However, the model could not explain the cross-over effect. Wintle also made an assumption on the cross-over phenomenon that the depth of penetration of the initial charge is field independent. Batra agreed with Wintle's assumption and then updated his model, but it still cannot account for the cross-over. He concluded that by attributing a finite field-independent depth of penetration to the space charge cannot explain the cross-over; a field-dependent mobility, thermally generated carriers, field-dependent injection and thermally activated release of the surface charge do not lead to any cross-over phenomenon either [64]. Later, Sonnonstine and Perlman came out with two distinct theories for surface potential decay in insulators [65]. The first is a modification of Batra's theory to include both instantaneous partial injection and field-dependent mobility. The second theory assumes that the charge carriers at the corona charged surface are in surface traps, they released from the traps by thermal process then injected into the bulk of the insulator. As a result, the approximate forms of the decay curves were theoretically predicted in the paper at certain surface potential; however, the charging conditions were neglected as they said that the instantaneous complete injection was the key fact to get the cross-over phenomenon. Baum et al [18, 66] demonstrated that the crossover phenomenon depended on the duration of the corona charging process, and the cross-over phenomenon did not occur for positive corona voltage, which apparently contradicts the findings of Ieda et al [14]. They concluded that the excited molecules as well as photons produced in the corona discharge play an important role in inducing charge from surface states to enter the bulk of material where they are much more mobile. This leads to rapid decay of surface potential at higher initial surface fields, and the crossover effect is then observed. They also proved that cross-over is charging-time dependent by demonstrating that no cross-over appeared for charging times of less than 25 ms even the initial surface fields are high. Kao et al [67] used thermally stimulated discharge (TSD) on negatively corona charged low density polyethylene revealed a deep surface

trap distribution centred at 95 ◦C and a shallow surface and bulk distribution centred at 55 ◦C. Using the same technique, they were able to show that corona generated excited free molecules trapped charge from the shallow traps, but have little effect on the deep traps. The free charge is driven by its own field into the bulk, can be retrapped in a trap of the same energy or another shallow trap. It also can transit through the sample. Charge release caused by the excited molecules gives rise to the crossover effect observed in surface potential decay by producing initial charge distributions which differ depending on charging conditions. In 1980, Toomer and Lewis [68] introduced a model that contains both deep and shallow surface traps in the sample. They also showed that negative charges penetrate more readily into the bulk and the bulk traps exist for both sign of carriers. In addition to various assumptions, which were not evident, one of the common features in the models proposed so far is that all the models are based on single charge carrier injection. The new experimental evidence from the Tony Davies HV Lab has shown this is not always the case especially where the cross-over is concerned. Bipolar charge injection has been verified by the measurement of space charge in the corona-charged sample as shown in the section below. This new finding challenges the existing surface potential decay models which were developed based on a single charge carrier injection [50].

## 3.2 Bipolar charge transport model

Recently, the bipolar charge transport model is widely used, and it contains three most important components: charge build-up (or generation), charge transport process with trapping/detrapping and charge recombination under dc voltage. One of the first attempts to develop a bipolar charge transport model in relation to experimentally determined space charge profiles and their dynamics was made by Alison and Hill in 1994. Trapping and recombination phenomena were included in the model which addressed degassed cross-linked polyethylene [69].

In the model, the description of carrier mobility is the most difficult part to solve. Charge transport within insulating polymers is often described by a hopping mechanism in which carriers move from site to site by getting over a potential barrier. For a single trapping level of depth $W$, the resulting current $J$ and mobility $\mu$ have the form:

$$J = 2neva \exp\left(-\frac{W}{kT}\right) \sinh\left(\frac{eEa}{2kT}\right) \quad (2)$$

$$\mu = \frac{2va}{E} \exp\left(-\frac{W}{kT}\right) \sinh\left(\frac{eEa}{2kT}\right) \quad (3)$$

which gives, in the low field limit $eEa \ll kT$,

$$\mu = \frac{vea^2}{kT} \exp\left(-\frac{W}{kT}\right) \quad (4)$$

where *n* is the charge carrier concentration, *e* is the elementary charge, *v* is the phonon frequency, *a* is the inter-site distance, *k* is the Boltzmann constant, *T* is the temperature and *E* is the field. Mott and Gurney [70] used it to describe ionic transport in disordered media, but it has been applied to both electrons and holes.

There is another mechanism to describe conduction in insulating polymers using phonon-assisted tunnelling in which site to site motion is achieved by tunnelling through the barrier. The tunnelling probability $W_{ij}$ from site *i* to site *j* is of the form [13]

$$W_{ij} = [\exp(-2\alpha a)][\exp\left(-\frac{E_j - E_i}{kT}\right)] \quad (5)$$

where $E_i$ and $E_j$ are the energy of the sites and $\alpha$ is a parameter describing the interaction between sites.

However, the most widely used principle for describing charge transport in polymeric insulation is to consider a trap-controlled mobility. Carriers move within bands and can be trapped in shallow sites in which they are still in interaction with bands. This scheme amounts to considering an effective mobility $\mu_{\text{eff}}$ of the form [13]

$$\mu_{\text{eff}} = \mu_b \exp\left(-\frac{W'}{kT}\right) \quad (6)$$

where $\mu_b$ is the band mobility and $W'$ is the activation energy of shallow traps. Trapping in deep traps is not accounted for in this approach.

The numeric approach of the bipolar charge transport model is essentially governed by three basis set of one-dimensional equations. They describe the behaviour of charge carrier in polymers through a time and spatial dependence *f(x,t)*. These three equations are,

Gauss's Law:

$$\frac{\partial E(x,t)}{\partial x} = \frac{\rho(x,t)}{\epsilon} \tag{7}$$

Transport Equation:

$$j(x,t) = \mu n(x,t) E(x,t) \tag{8}$$

Continuity Equation:

$$\frac{\partial n(x,t)}{\partial t} + \frac{\partial j(x,t)}{\partial x} = s \tag{9}$$

where

$\epsilon$ -- dielectric permittivity (F/m)

$\mu$ -- mobility of carriers ($m^2$/Vs)

ρ -- net charge density ($C/m^3$)

n -- density of mobile species ($C/m^3$)

*E* -- electric field (V/m)

*j* -- current density ($A/m^2$)

*x* -- spatial coordinate (m)

*t* -- time (s)

*s* -- source term

The Gauss's Law can be solved by direct discretization method or advanced finite element method. The continuity is normally solved using a splitting method. It is completed by first solving the equation,

$$\frac{\partial n(x,t)}{\partial t} + \frac{\partial j(x,t)}{\partial x} = 0 \tag{10}$$

And then resolve the second equation,

$$\frac{\partial n(x,t)}{\partial t} = s \tag{11}$$

Here the source term is contributed by charge recombination and trappings that are illustrated in Figure 3-1. For each species, mobile or trapped, the equation (11) actually consists of four equations:

$$s_1 = \frac{\partial n_{e\mu}}{\partial t} = -S_1 n_{ht} n_{e\mu} - S_3 n_{h\mu} n_{e\mu} - B_e n_{e\mu}\left(1 - \frac{n_{et}}{n_{0et}}\right) \quad \text{mobile electrons}$$

$$s_2 = \frac{\partial n_{h\mu}}{\partial t} = -S_2 n_{et} n_{h\mu} - S_3 n_{h\mu} n_{e\mu} - B_h n_{h\mu}\left(1 - \frac{n_{ht}}{n_{0ht}}\right) \quad \text{mobile holes}$$

$$s_3 = \frac{\partial n_{et}}{\partial t} = -S_2 n_{ht} n_{et} - S_0 n_{ht} n_{et} + B_e n_{e\mu}\left(1 - \frac{n_{et}}{n_{0et}}\right) \quad \text{trapped electrons}$$

$$s_4 = \frac{\partial n_{ht}}{\partial t} = -S_1 n_{ht} n_{e\mu} - S_0 n_{ht} n_{et} + B_h n_{h\mu}\left(1 - \frac{n_{ht}}{n_{0ht}}\right) \quad \text{trapped holes} \tag{12}$$

where $s_1$, $s_2$, $s_3$, $s_4$ are the source term for each species; $S_0$, $S_1$, $S_2$, $S_3$ are the recombination coefficient for different opposite species; $B_e$, $B_h$ are the electrons/holes trapping coefficients; $n_{e\mu}$, $n_{et}$, $n_{h\mu}$, $n_{ht}$ respectively indicate the densities of mobile electron, trapped electrons, mobile holes and trapped holes; $n_{0et}$ and $n_{0ht}$ are the trap densities for electrons and holes [71, 72].

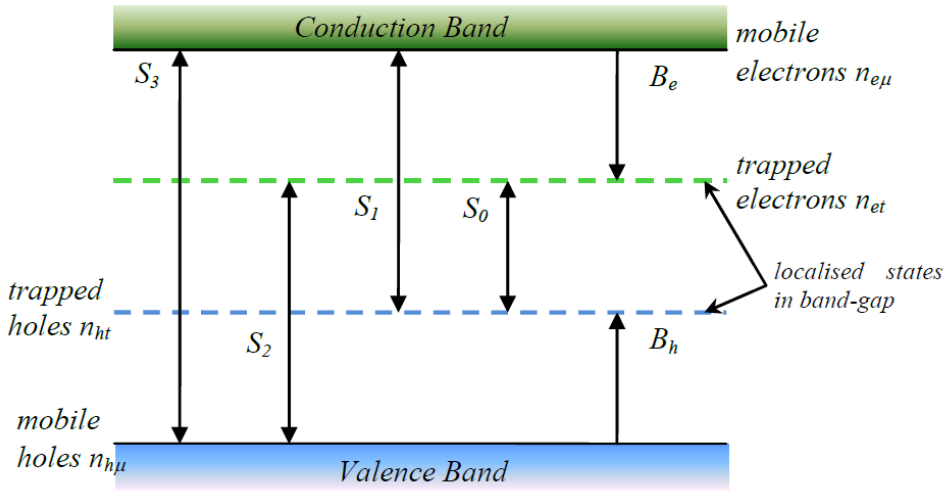


Figure 3-1 Schematic diagram of the conduction, trapping and recombination [73]

The boundary condition is defined by the Schottky injection [71-73] at both electrodes,

$$j_e(0,t) = AT^2\exp(-\frac{ew_{ei}}{kT})\exp(\frac{e}{kT}\sqrt{\frac{eE(0,t)}{4\pi\varepsilon}})$$
$$j_h(d,t) = AT^2\exp(-\frac{ew_{hi}}{kT})\exp(\frac{e}{kT}\sqrt{\frac{eE(d,t)}{4\pi\varepsilon}})$$

(13)

where $j_e(0,t)$ and $j_h(d,t)$ are the fluxes of electrons and holes at the cathode and anode respectively; T is the temperature; $A = 1.2 \times 10^6 Am^{-1}K^{-2}$ is the Richardson constant; $w_{ei}$ and $w_{hi}$ are the injection barrier for the electrons and holes.

The charge extraction at both electrodes also needs to be considered. If the extraction barrier is set, the current follows a Schottky law (with a barrier different from the one for injection). Otherwise, the extraction fluxes are:

$$j_e(d,t) = \mu_e E(d,t) n_{e\mu}(d,t)$$
$$j_h(0,t) = \mu_h E(0,t) n_{e\mu}(0,t)$$

(14)

The total current density, *J(x,t)* is obtained from the total current equation (15). The first item on the right is the conduction current density; the second is the displacement current density.

$$J(x,t) = j(x,t) + \varepsilon\frac{\partial E(x,t)}{\partial t} \quad (15)$$

The bipolar charge transport model can produce the mobile and trapped charges distribution inside the material, which cannot be observed experimentally. Also, adjusting the model parameters such as charge injection barrier height, mobility, trap coefficient and recombination coefficient can control the total charge distribution and the electric field inside the material.

## 3.3 New model on surface potential decay

Recently, the new surface potential decay model based on the bipolar charge injection described in last section has been proposed as shown in Figure 3-2.

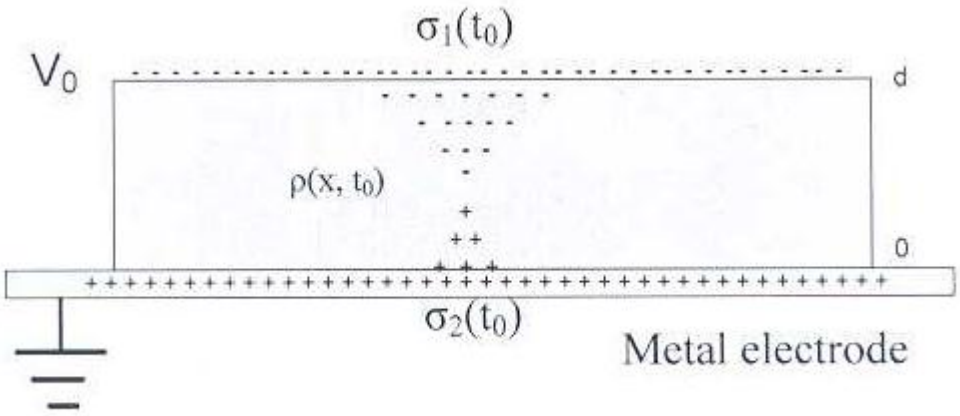


Figure 3-2 Model for surface charge and space charge distribution immediately after corona charging [74]

In Figure 3-2, $V_0$ is the grid voltage and represents the upper limit of the surface potential. $\sigma_1(t_0)$, $\rho(x, t_0)$ and $\sigma_2(t_0)$ are surface charge on the top surface, space charge in the sample and induced charge on the metal electrode respectively. The initial values of all these parameters will depend on the charging voltage and time and their subsequent values will change with time. After the charges are injected into the material under a certain applied field, it will drift across the material under the influence of the electric field produced by both surface charges and space charges. The mobility used in the current model varies with the initial surface potential as it has been widely reported that mobility is field dependent. During this process, some carriers are trapped in the localized states, i.e. deep trap centres and therefore, reduce the total amount of charges moving across the material. As the extra de-trapping term is used, few charges can escape the trap and continue their travelling across the material. On the other hand, they are prone to recombine with their opposite species (electrons with holes).

The charge transport in the bulk of the sample is determined by the electric field. The electric field in the sample at any time consists of contributions from three components, i.e. space charge $\rho(x, t)$, surface charge density at the top $\sigma_1(t)$ and the induced surface charge density at the bottom electrode $\sigma_2(t)$. We assume that the field components are represented by $E_\rho(t)$, $E_{\sigma 1}(t)$ and $E_{\sigma 2}(t)$ respectively, then the surface potential can be calculated by integrating the total electric field:

$$V_0(t) = \int_0^d [E_\rho(t) + E_{\sigma_1}(t) + E_{\sigma_2}(t)]dx \tag{16}$$

In addition, the total charge in the system at any time must be in balance, i.e.

$$\sigma_1(t)S + \sigma_2(t)S + \int_0^d \rho(x,t)Sdx = 0 \tag{17}$$

where S is the surface area where charges are present.

It is clear to see that $\sigma_1(t)$, $\sigma_2(t)$ and $\rho(x, t)$ are dependent quantities. Based on the model, it is possible to calculate $\rho(x, t)$ during the corona charging until a predefined charging time $t=t_0$. The quantities $V_0(t_0)$ and $\rho(x, t_0)$ are the initial condition for surface potential decay. This allows one to determine $\sigma_1(t_0)$ and $\sigma_2(t_0)$ using equations (16) and (17). Once these initial four quantities are determined, one can calculate new space charge distribution $\rho(x, t_0+\Delta t)$ based on the proposed model and the two surface density $\sigma_1(t_0+\Delta t)$ and $\sigma_2(t_0+\Delta t)$ using the Schottky injection [74].

The simulation procedure is explained in the flow chart as shown in Figure 3-3. For the numerical computation, the dielectric specimen is discretized into m (m=100) equal elements of width Δx along its thickness, shown in Figure 3-4. $j_e$ is the flow of mobile electrons from the $k^{th}$ division into the $k+1^{th}$ division and $j_h$ the flow of mobile holes inversely. $j_e$ and $j_h$ of each element are computed progressively from the 1st division to the mth division at each time step *dt*. The simulation is implemented using MATLAB coding and PDE solvers. It has been found that time step of 0.01 s is good enough to produce reasonable results compared with the published simulation results [73-75]. However, there is no difference in the simulated space charge profiles when choosing a larger time step of 0.1 s. Therefore, the simulation in this paper select 0.1 s time step which is ten times faster than using 0.01 s time step without losing accuracy. The spatial

resolution of d/m depends on the specimen thickness. For a thickness of 50 μm, the current spatial resolution of 0.5 μm produces enough resolution for the space charge accumulation in the bulk of polyethylene as the smallest penetration depth of space charge into the bulk of polyethylene is much larger than the spatial resolution. The smaller spatial resolution at m=1000 leads to no observable difference of computation results other than causing considerable time consumption, e.g. it takes more than 400 seconds running to simulate the equivalent one second. A detail of the MATLAB code is shown in Appendix A.

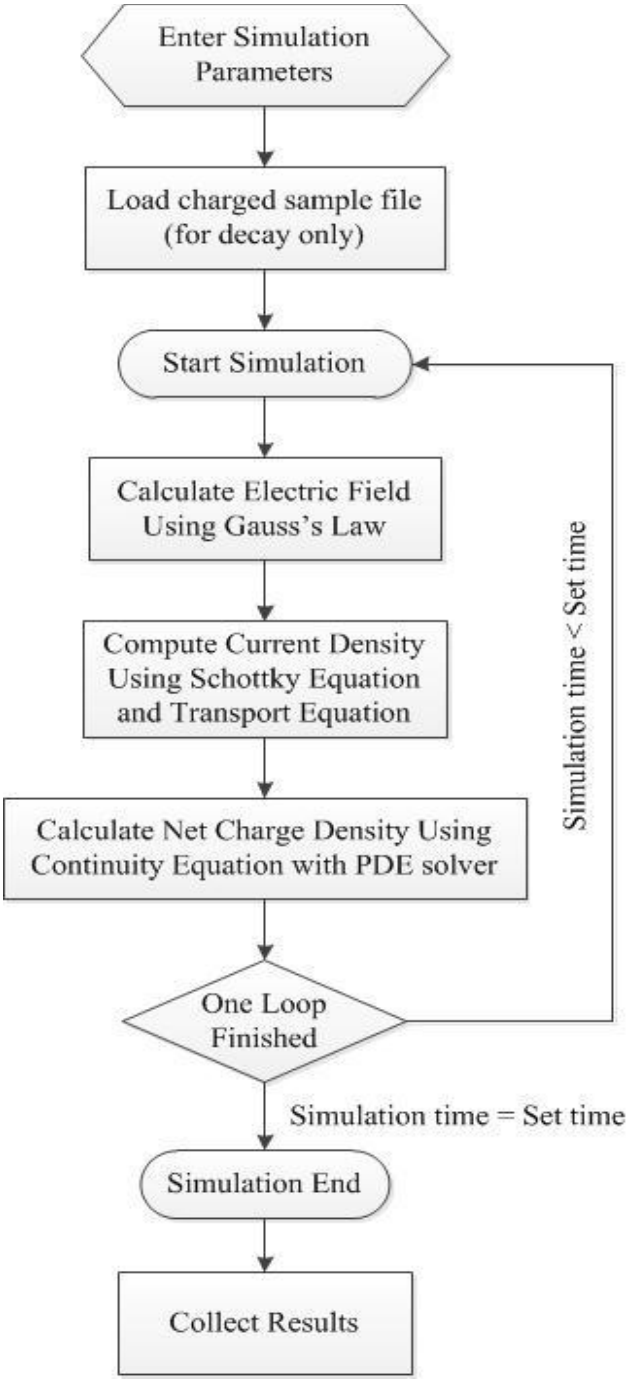


Figure 3-3 Flow chart of simulation.

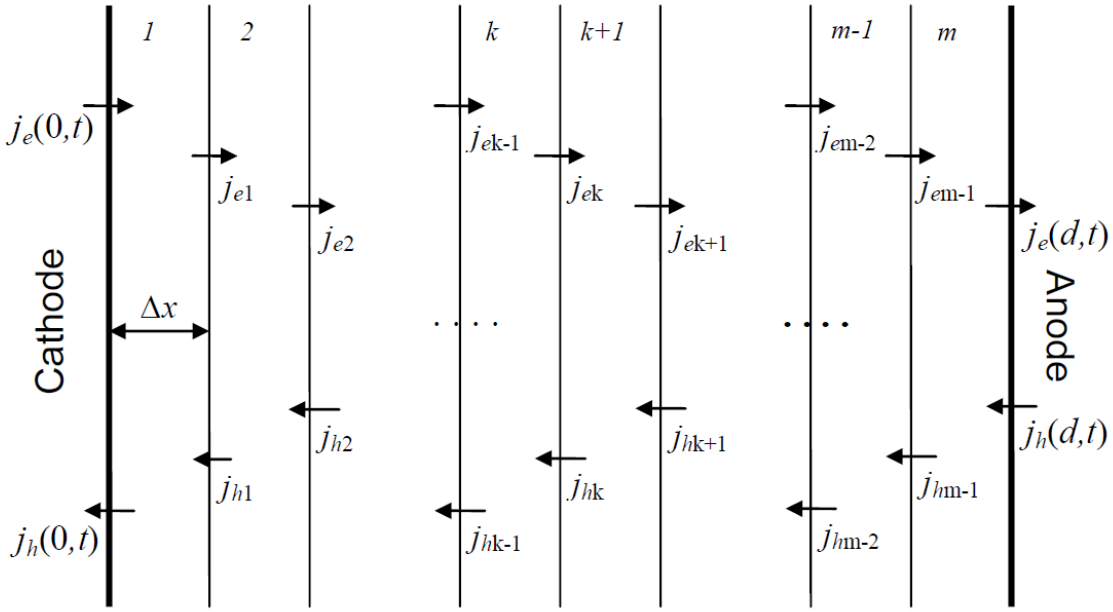


Figure 3-4 Discretization of the specimen.

## 3.4 Effect of parameters in the model

The selection of parameters in the model can affect the final results a lot. To find out how the parameters in the current model will change surface potential decay results, a few tests had been carried out: a) different charging voltages, b) different injection barrier heights, c) different mobilities, d) different trap coefficients, e) different trap densities and f) different recombination coefficients. The parameters tested in the model have also been listed in Table 3-1.

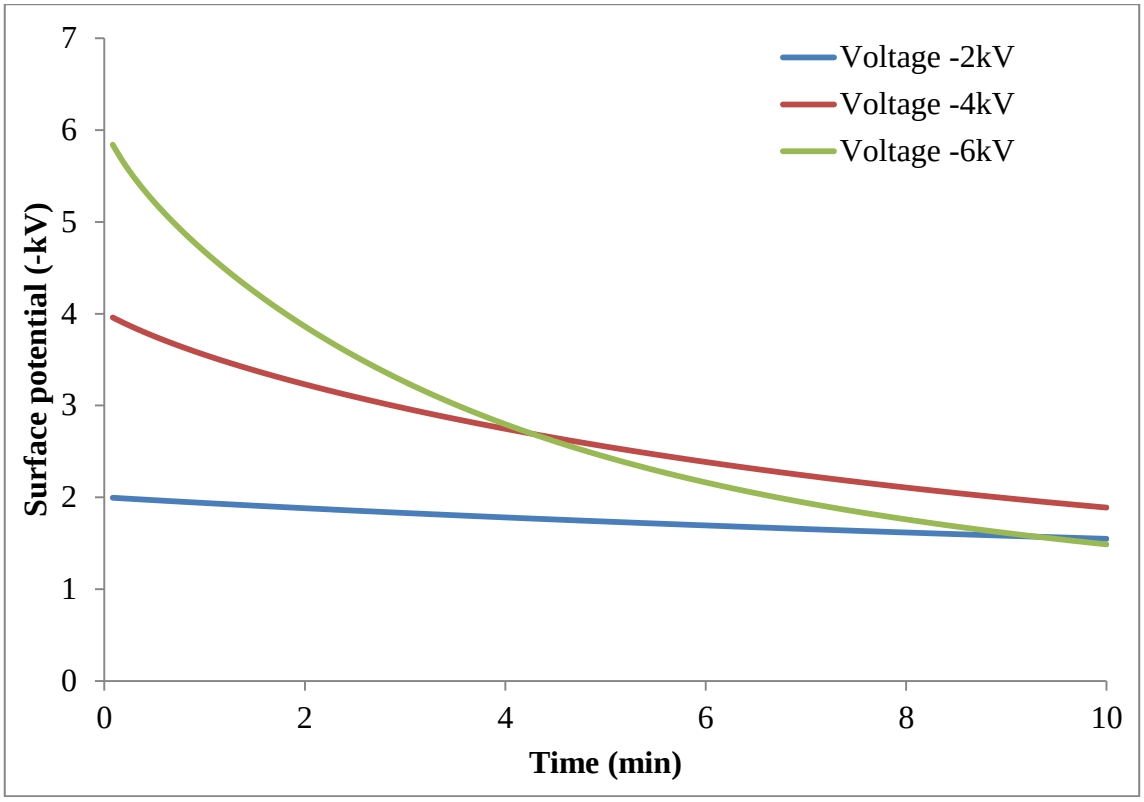


Figure 3-5a Simulation results with different charging voltages based on original value from Table 3-1

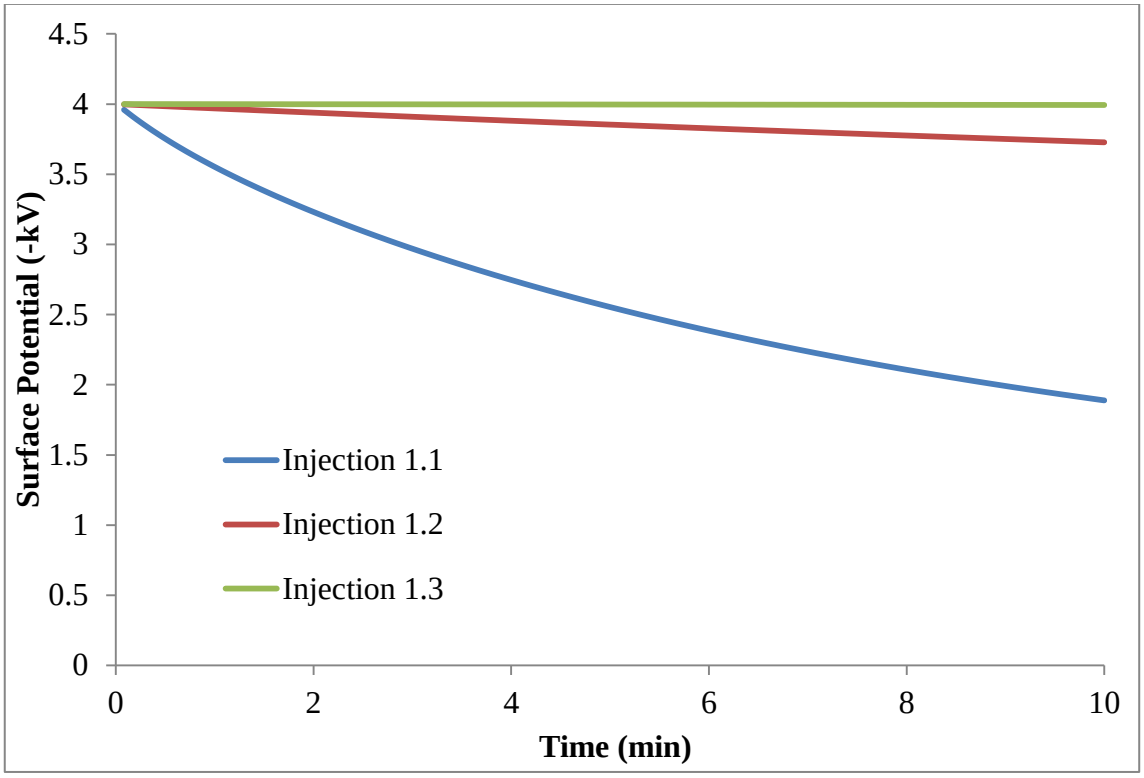


Figure 3-5b Simulation results with different injection barrier heights based on original value from Table 3-1

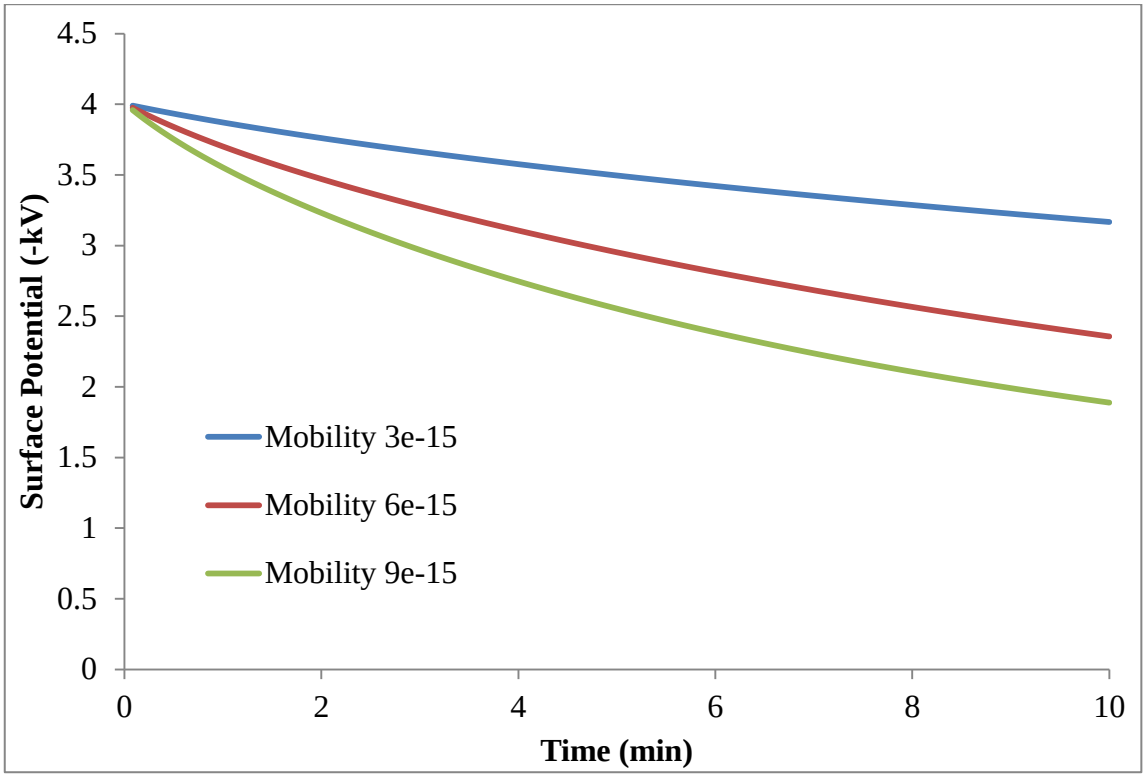


Figure 3-5c Simulation results with different mobilities based on original value from Table 3-1

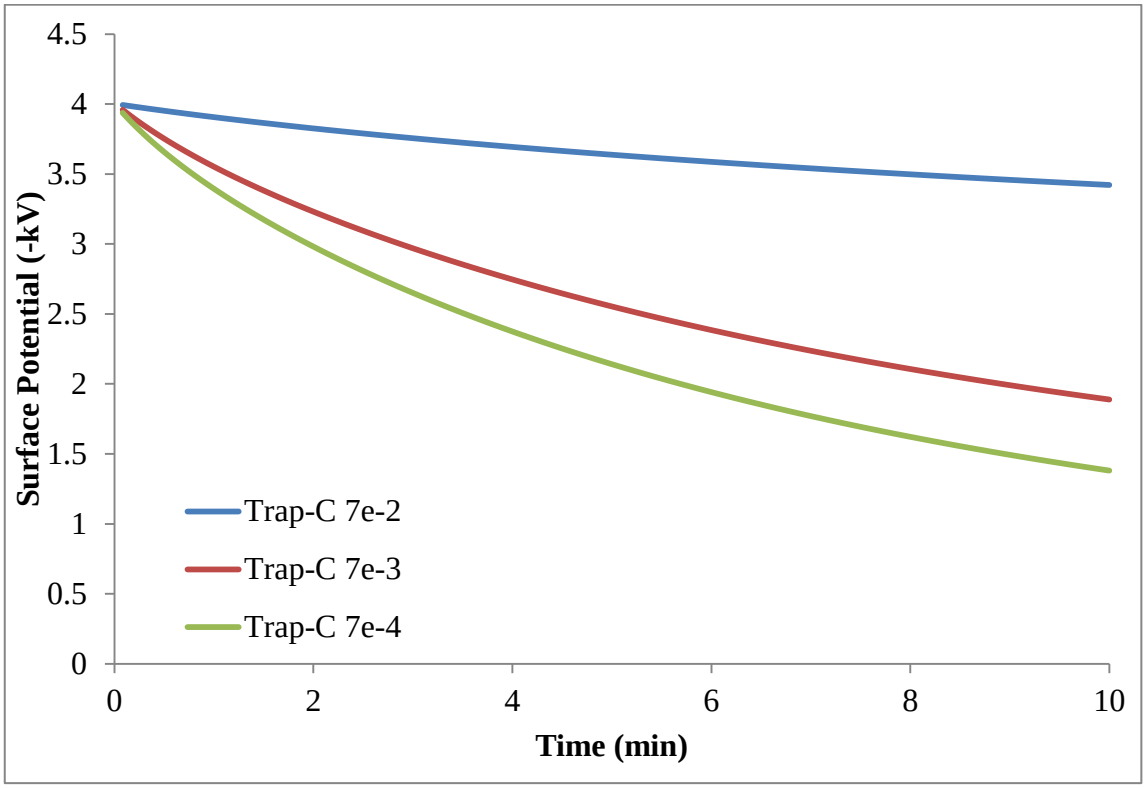


Figure 3-5d Simulation results with different trap coefficients based on original value from Table 3-1

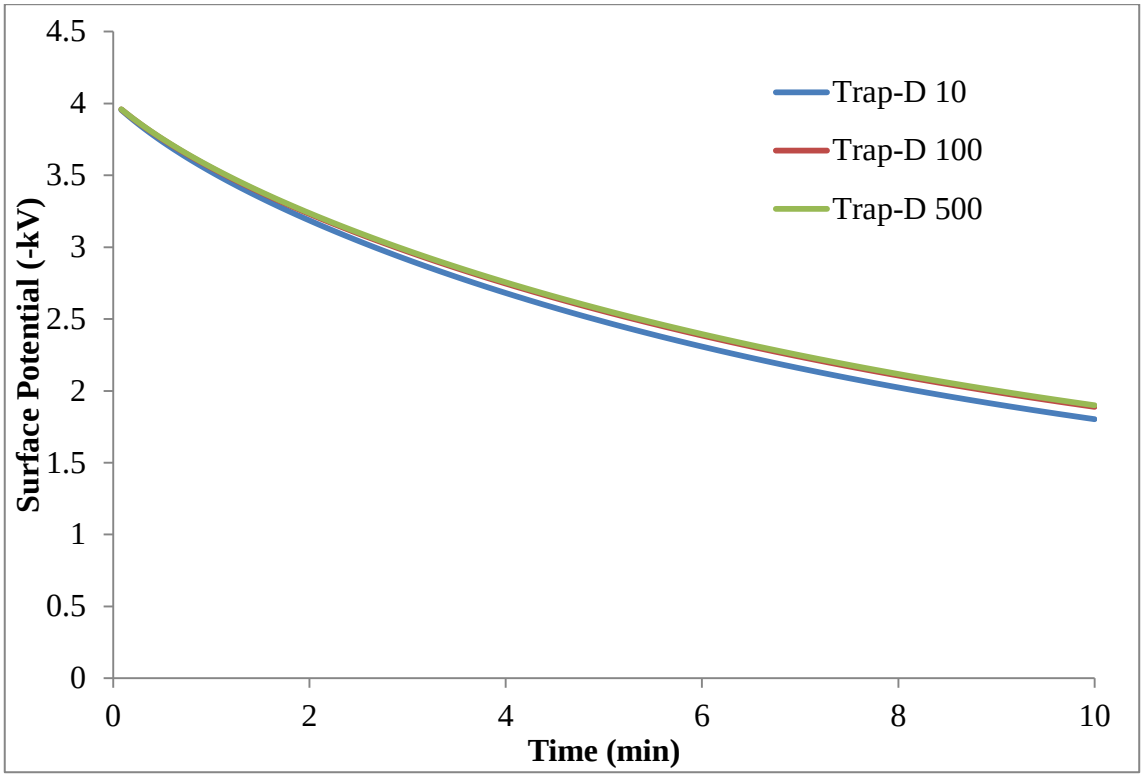


Figure 3-5e Simulation results with different trap densities based on original value from Table 3-1

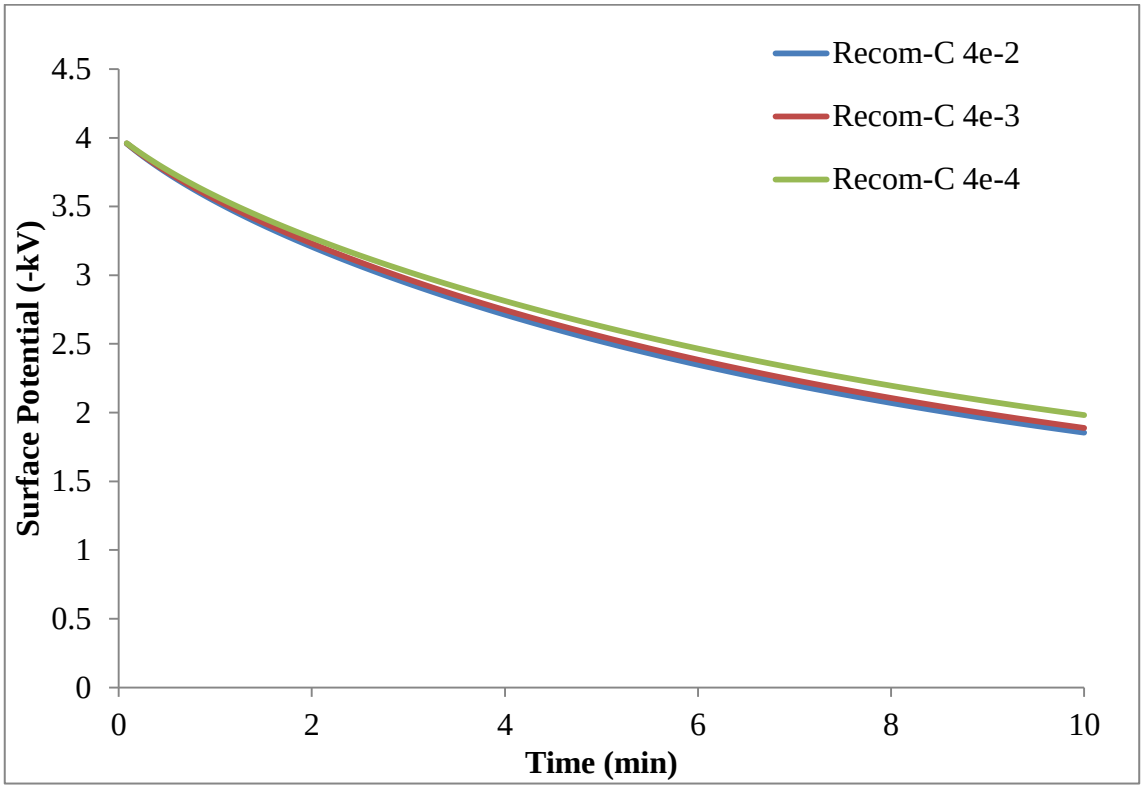


Figure 3-5f Simulation results with different recombination coefficients based on original value from Table 3-1

Table 3-1 Tested Simulation Parameters

| Parameters (Units) | Original Value | Changed Value I | Changed Value II |
|---|---|---|---|
| Grid Potential (V) | -4000 | -2000 | -6000 |
| Injection Barrier Height (eV) | 1.1 | 1.2 | 1.3 |
| Electron/Hole Mobility ($m^2v^{-1}s^{-1}$) | 9.00E-15 | 6.00E-15 | 3.00E-15 |
| Trap Coefficient ($s^{-1}$) | 7.00E-03 | 7.00E-02 | 7.00E-04 |
| Trap Density ($Cm^{-3}$) | 100 | 10 | 500 |
| Recombination Coefficient $S_0$, $S_1$, $S_2$ ($m^3C^{-1}s^{-1}$) | 4.00E-03 | 4.00E-02 | 4.00E-04 |

From the results above, it can be clearly seen that changes made on the grid potential has the biggest effect on the surface potential decay results due to changes in the electric field and charge injection. The cross-over phenomenon can readily be seen from Figure 3-5a. Changes in the injection barrier height also have a significant influence on the surface potential decay results. The lower the injection barrier height, the higher the amount of charge injection will be. Changes in the mobility of electrons and holes can cause a big change to the decay results as well. As mentioned before, charge decay in this model has two different ways, one is leaking from the opposite electrodes, the other is recombining with an opposite sign charge. In this case, if the mobility is higher, the charges are more likely to travel through the bulk of the material; therefore, a faster potential decay can be observed. The trap coefficient parameter controls the rate of mobile charge carriers being trapped in the deep trap centres per second and hence affects the density of mobile and trapped charge carriers. The higher trap coefficient means the more trapped charges and less mobile charges inside the bulk of the material, therefore, slows down the surface potential decay. The trap density indicates the maximum amount of trapped charge in the deep trap sites. A large trap density implies a large probability of trapping occurring. However, the simulation does not demonstrate any significant difference of charge profiles with increased trap densities, but results do indicate a few more trapped charges and a slight reduction of mobile charge density, as shown in Figure 3-5e. Changes in the recombination coefficient have also very little effect on the surface potential decay results. Therefore, it can be concluded that to fit the experimental results using the bipolar charge transport model, values of charge injection

barrier height, electron and hole mobility and trap coefficient are the parameters that need to be focused on.

# Chapter 4 Effect of Different Ground Electrodes on Surface Potential Decay

## 4.1 Gold ground sample preparation

Previous work [21, 50, 76] applied the PEA technique to a corona charged sample and observed the bipolar charge injection from both surface and the charge decay process inside the polymer film. To further verify the bipolar charge injection model, a gold ground LDPE sample was examined and compared with an aluminium ground LDPE sample. The gold electrode was metallized by K500X Sputter coater (Figure 4-1) for 2 min and 30 seconds using a 25 nA current, which gives a 20 nm thick gold on one side of the polymer. As the earth plate is made from aluminium, the bottom surface of the sample will be in direct contact to it. Therefore, it is termed as the aluminium electrode sample. There are two ways to build gold electrode samples: one is that the gold coated on one side of the LDPE sample and the sample will contact the aluminium earth plate; the other is that the gold coated on the aluminium earth plate.

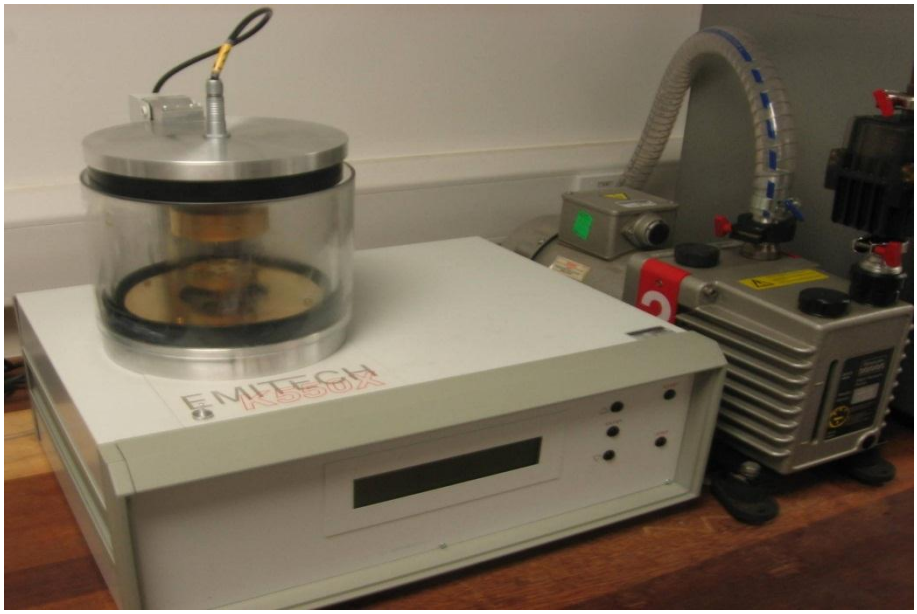


Figure 4-1 K5000X Sputter coater

## 4.2 Experimental Results and Discussion

### *4.2.1 Surface potential decay measurement*

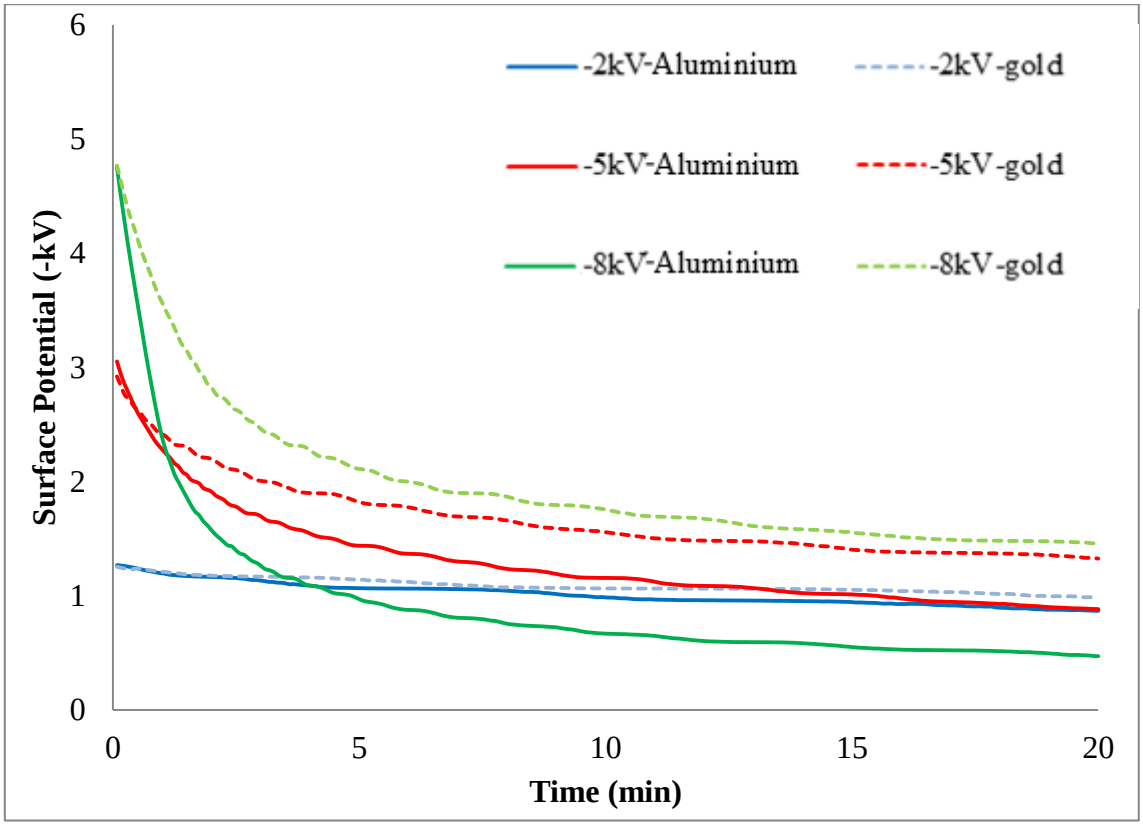


Figure 4-2 Surface potential decay for aluminium ground and gold ground with different grid voltages

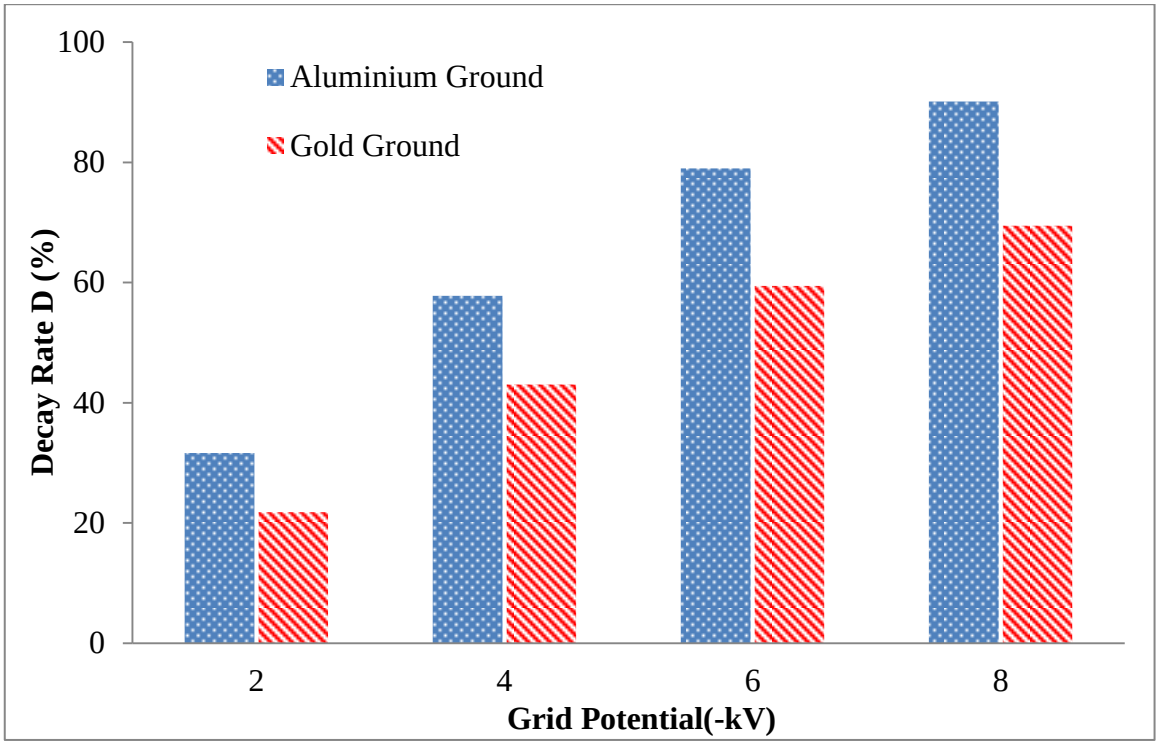


Figure 4-3 Surface potential decay rates for aluminium ground and gold ground

In this section, the surface potential decay results measured by the static monitor were discussed. Negative polarity was used to deposit charges on the sample surface; however, for the sake of easy visualization the absolute surface potential had been used here. It had been observed that the surface potential decay curves are almost the same for gold coated sample and sample placed on gold coated ground electrode, only the results obtained from the gold coated sample were shown here for comparison with aluminium ground sample. From Figure 4-2, the difference between the gold ground and aluminium ground LDPE films can be clearly seen especially with higher corona charging voltage. The cross-over phenomenon was seen with the aluminium LDPE in a short decay period (at about 4 min). However, for the gold ground LDPE it may shift to a much longer time and it cannot be observed over 20 min decay. To analyse the effect of different ground electrode, a decay rate D is introduced. D is defined as:

$$D = \frac{V(t_0) - V(t)}{V(t_0)} \times 100\,\% \tag{18}$$

where $V(t_0)$ and $V(t)$ are the potentials for the initial potential and the potential after a certain time respectively. The detailed decay rates at 20 min for both samples and selected voltage levels were plotted in Figure 4-3. The decay rate D increases with the

initial surface potential contain a complex mechanism. It is clearly shown that the gold ground samples have a slower decay rate compared with the aluminium ground samples under all the voltage levels. This is described later in section 4.2.4.

### *4.2.2 Corona charging current measurement*

Figure 4-4 shows the corona charging current that was calculated from the measured voltage across the 10 MΩ resistor. The current below – 3 kV is too noisy to be measured in the present arrangement. The initial current magnitude is not shown in Figure 4-4 so that the current with lower magnitude can be clearly observed as our interest lies in the "steady state" of this current. To quantify the difference, the ratio of gold ground current (GGC) and aluminium ground current (AGC) at 120 s charging time is shown in Figure 4-5.

$$Ratio = \frac{GGC}{AGC} \times 100\,\% \tag{19}$$

It can be seen that the measured current in the gold ground electrode LDPE films is smaller than the current of aluminium ground LDPE films at any voltage levels, and surprisingly, the ratio between these currents are around 75 % for all the voltage levels measured. The reason is discussed in section 4.2.4.

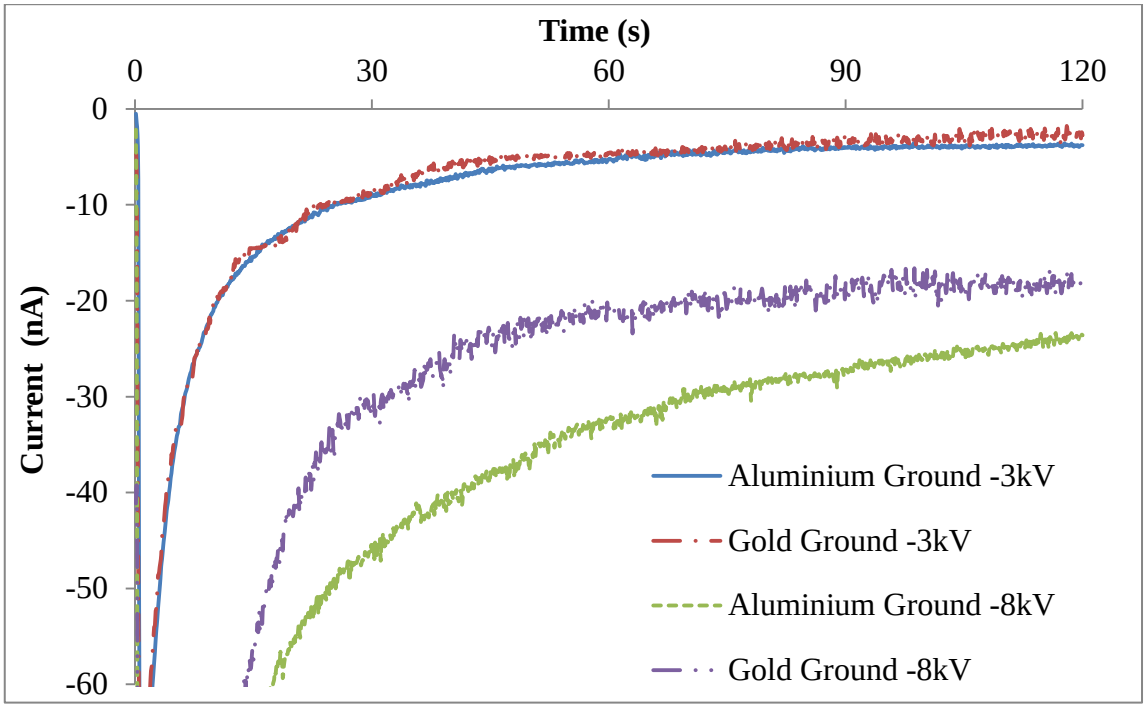


Figure 4-4 Corona charging current for aluminium ground sample and gold ground sample

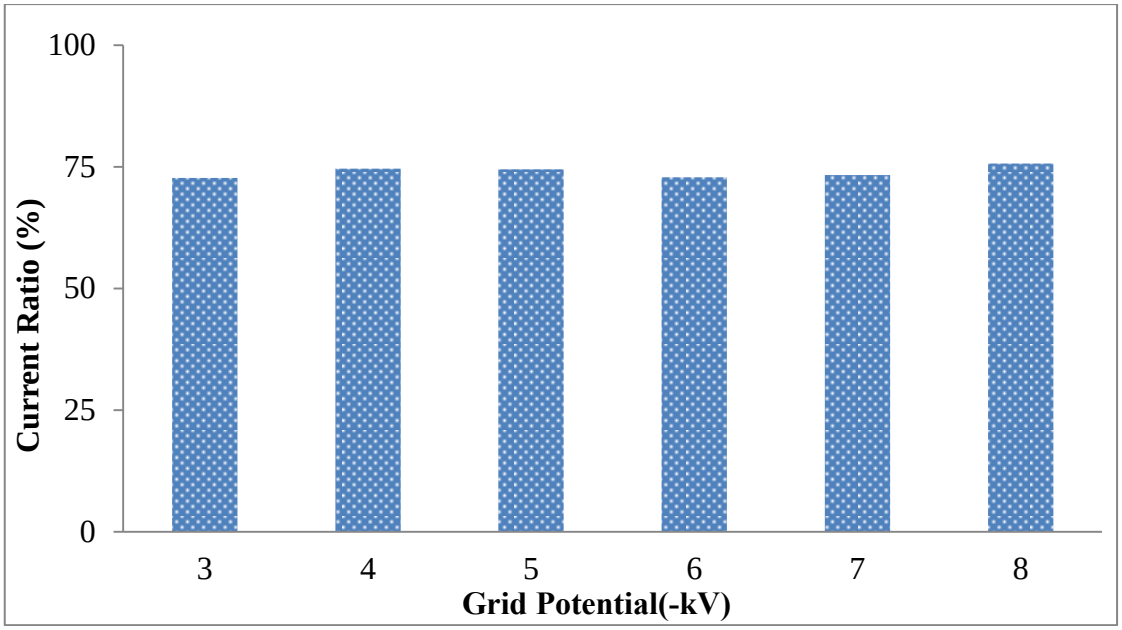


Figure 4-5 Corona charging current ratio versus grid potential for aluminium ground sample and gold ground sample at 2 min

### *4.2.3 Space charge measurement*

It is clear from the above results that the charge injection from the bottom electrode affects the surface potential decay and the corona charging current. To reveal the

mechanism that may be responsible for the observed phenomenon, charge distribution in corona charged LDPE with different electrodes were measured as shown in Figures 4-6 and 4-7. Based on the setup in Figure 2-8, there are two distinctive charge troughs and peaks across the aluminium ground sample from left to right and one trough and two peaks for gold ground sample. For the aluminium ground sample, the first trough and last peak are known as the induced charge perks on the PEA electrodes, and the first peak corresponds to the bottom surface of the corona charged film and the second trough represents the charges from the corona charged side of the sample. For gold ground sample, the first induced charge trough was disappeared because the gold coated side of the sample is grounded during corona charging process. The charges on the gold electrode were induced due to space charge in the sample and surface charge on the top surface. Therefore, based on the measuring set up in Figure 4-8, there are no further induced charges on the plate electrode, i.e. no electric field in LDPE film *B*. Consequently, the first trough disappears compared with the aluminium ground sample.

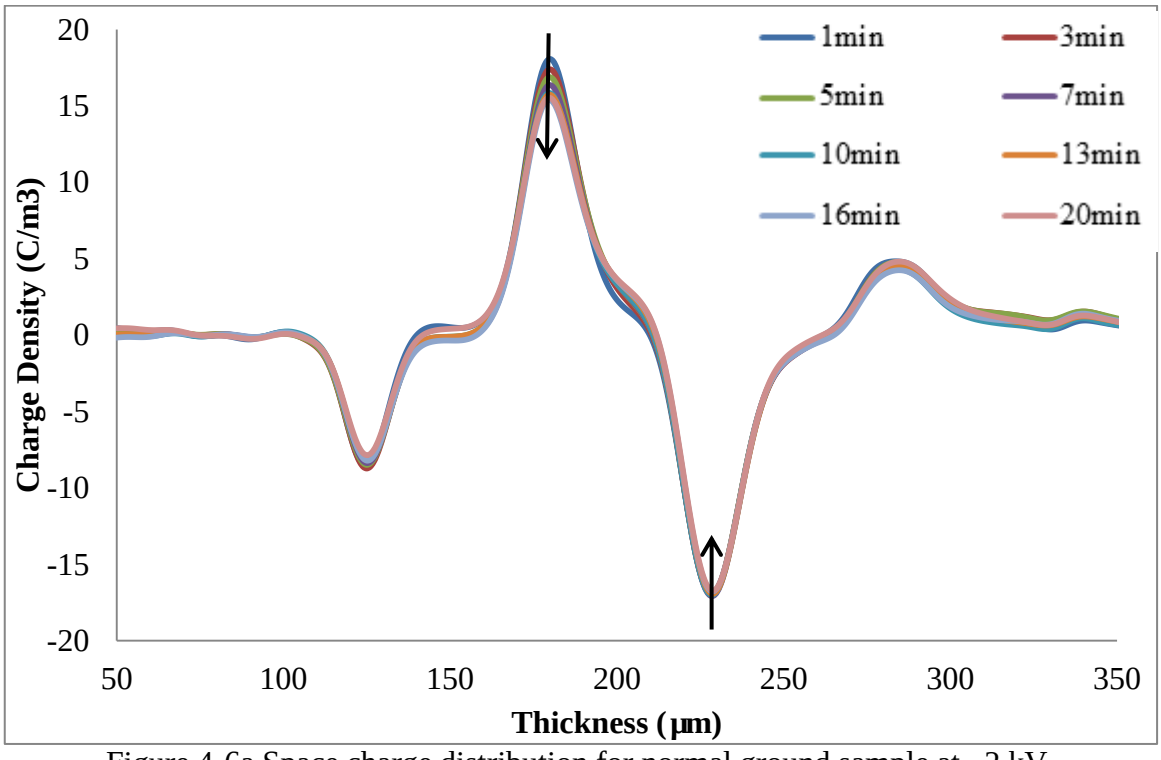


Figure 4-6a Space charge distribution for normal ground sample at– 2 kV

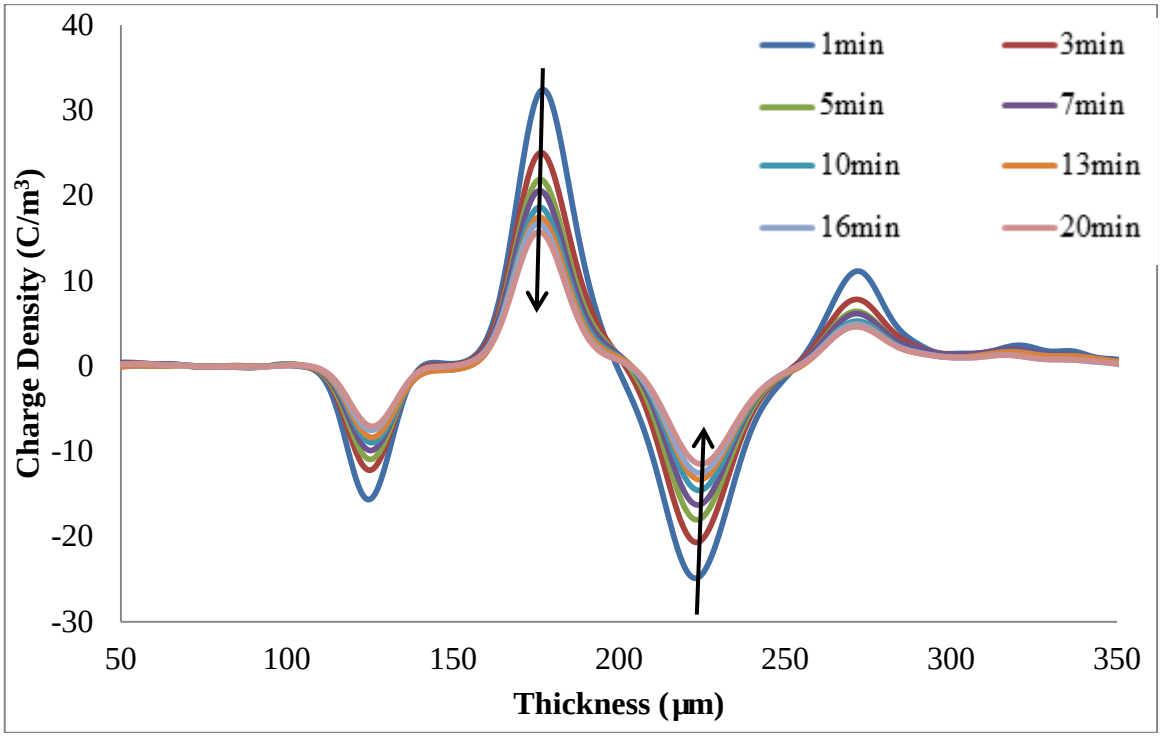


Figure 4-6b Space charge distribution for normal ground sample at– 4 kV

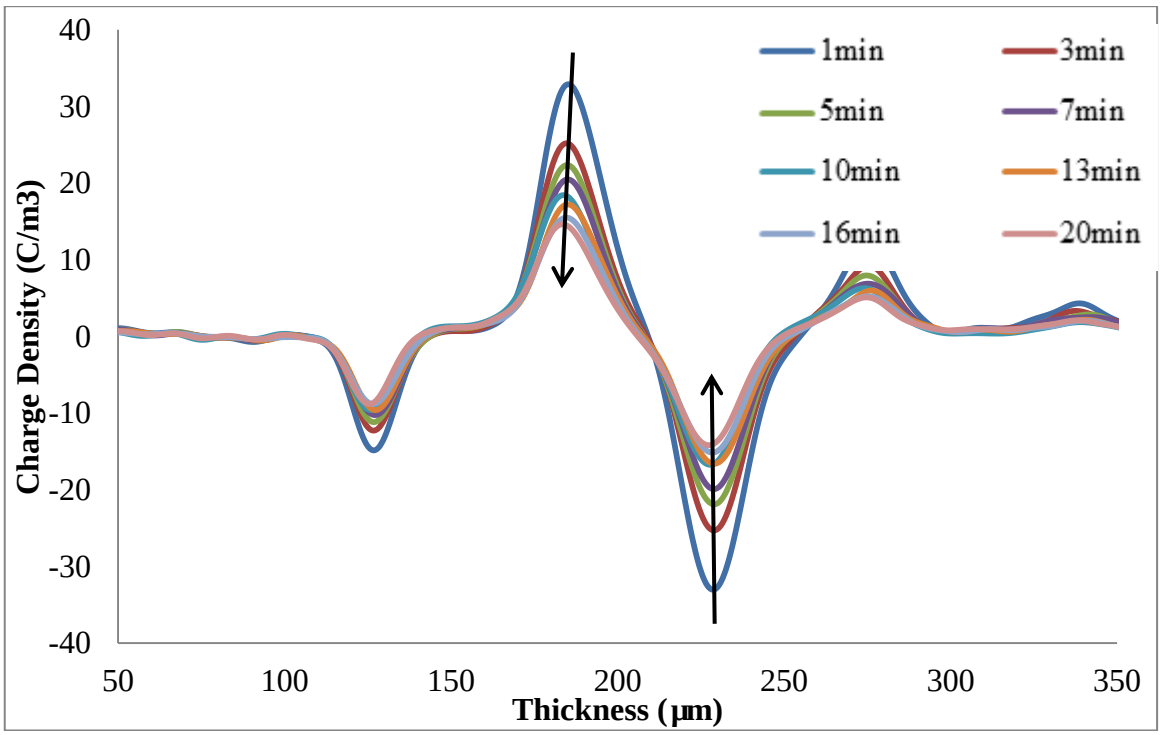


Figure 4-6c Space charge distribution for normal ground sample at– 6 kV

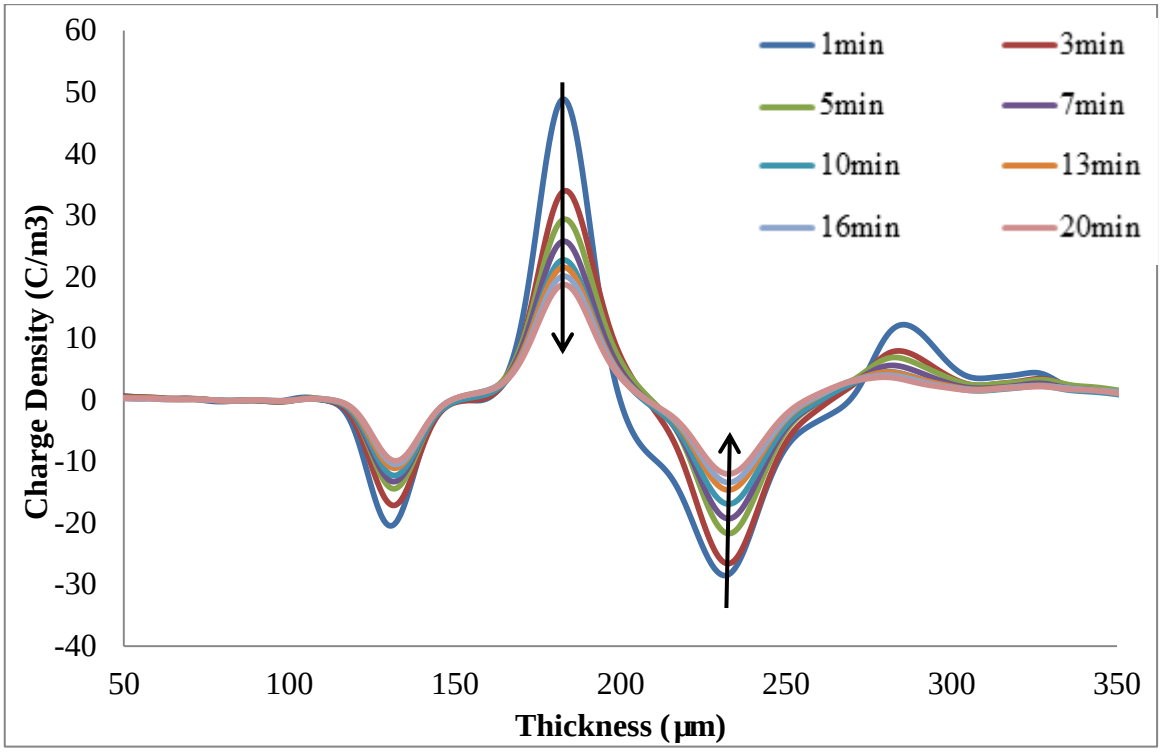


Figure 4-6d Space charge distribution for normal ground sample at– 8 kV

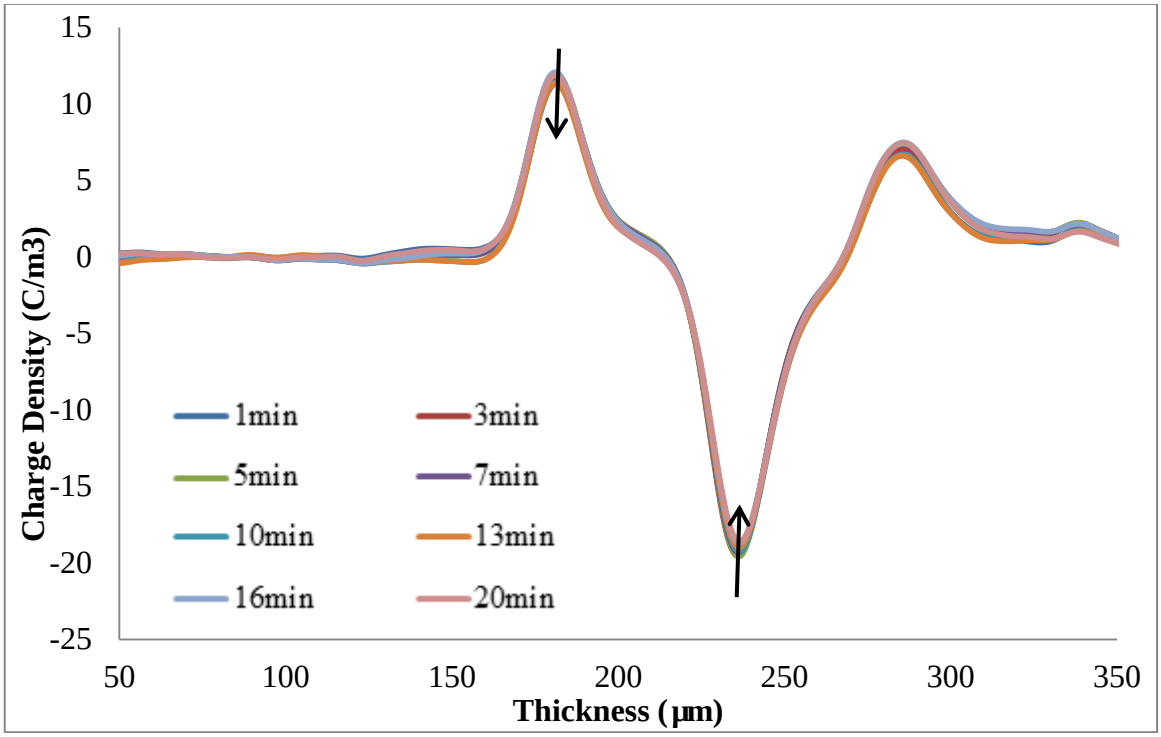


Figure 4-7a Space charge distribution for gold ground sample at – 2 kV

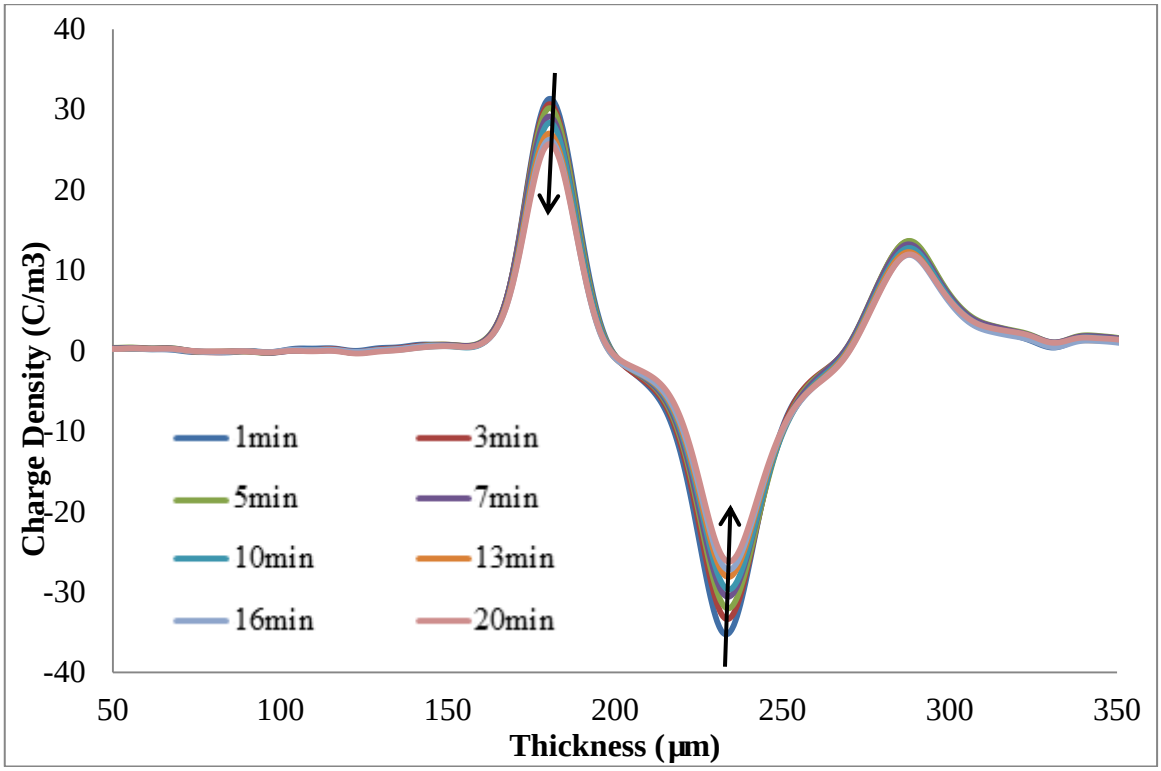


Figure 4-7b Space charge distribution for gold ground sample at – 4 kV

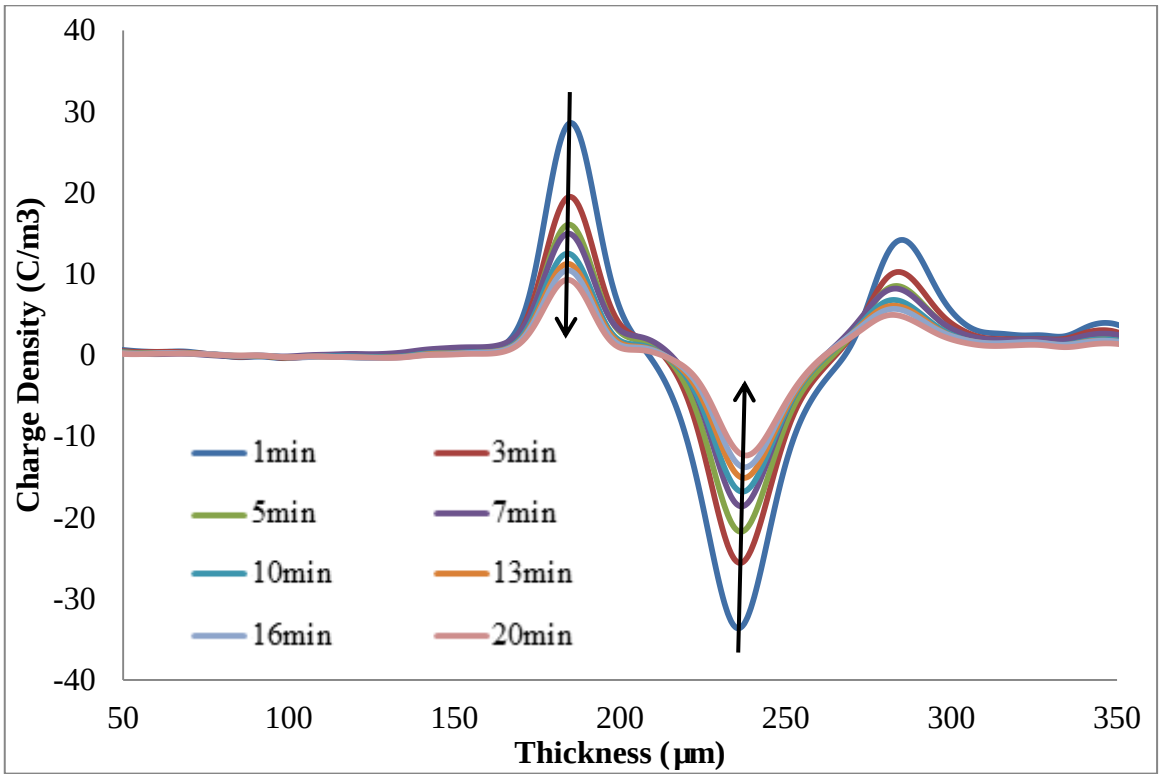


Figure 4-7c Space charge distribution for gold ground sample at – 6 kV

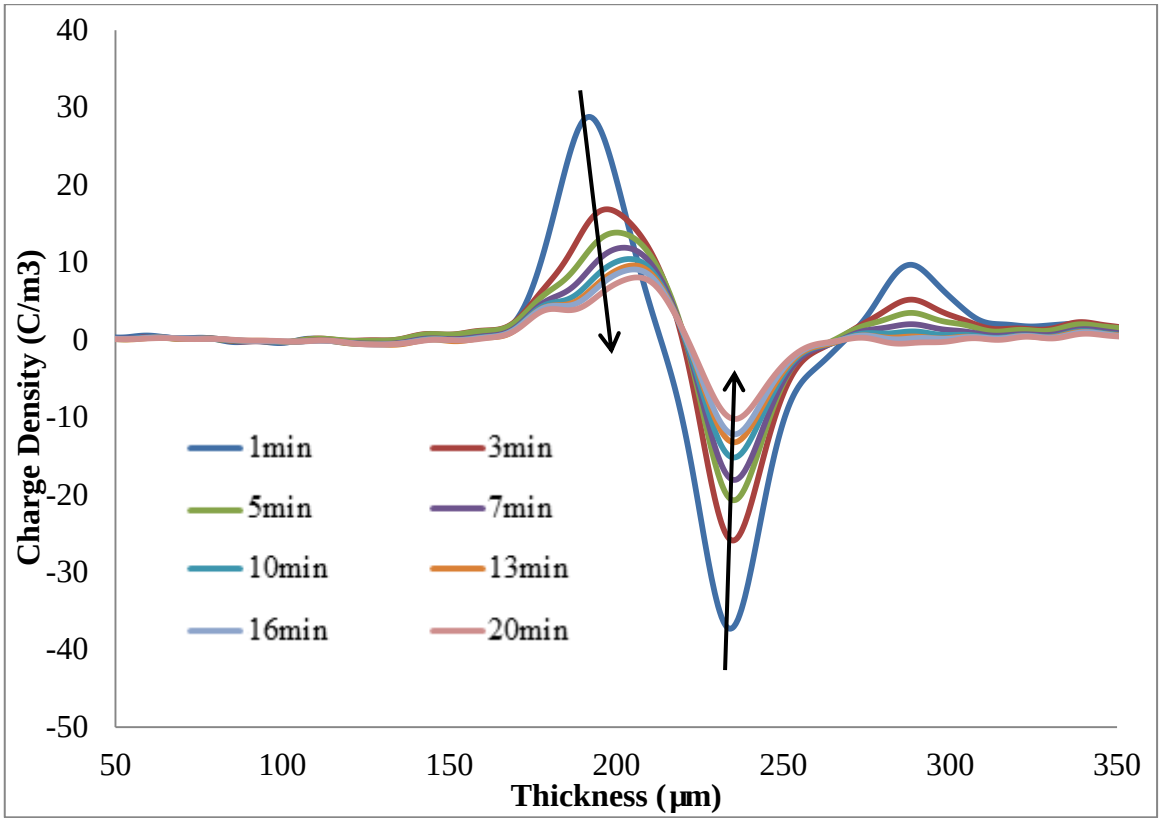


Figure 4-7d Space charge distribution for gold ground sample at – 8 kV

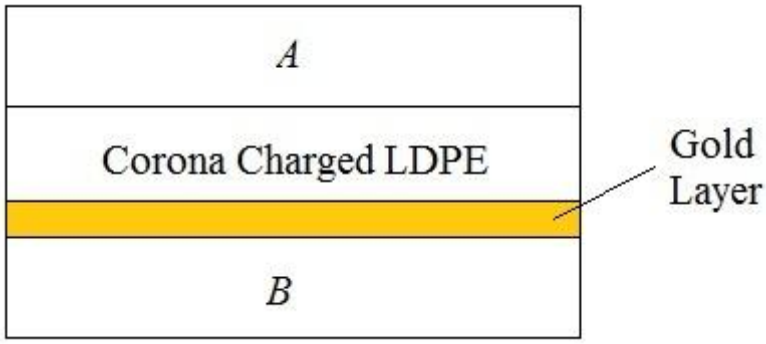


Figure 4-8 Space charge measurement set up for gold ground sample

### *4.2.4 Discussion*

Polyethylene is a typical semi-crystalline material; it contains various charge traps [77]. Therefore, it is believed that the injected charge can be captured by these traps on its way towards to the opposite electrode. Charge injection had been observed to occur in LDPE above a threshold value of 10 kV $mm^{-1}$ [78]. From the surface potential in Figure 4-2, the lowest electric field is 25 kV $mm^{-1}$, which is well above the threshold electric

field value. Therefore, charge injection dominates all the voltage level in this study. By selecting different ground electrode of the sample, the differences in the decay rate, the corona charging current and the charge density on the bottom surface of the corona charged sample can be clearly observed. The work function for gold (Au) is 5.1 - 5.47 eV and for aluminium (Al) is 4.06 – 4.26 eV [79] i.e. gold has a higher work function than aluminium. This means that charge exchange between aluminium and the polymer is easier than gold. Therefore, it explains why different bottom ground electrode can produce differences in the results and the injection from the bottom surface of the sample during corona charging must be taken into account. The results suggest that the charge injection from the bottom electrode takes place. As the cross-over phenomenon only occurs on the sample with an initial high surface potential, the above observation further validates that the bipolar charge injection model can be used to account for the phenomenon.

There are few common features that can be found by comparing Figure 4-6 with Figure 4-7. The first one is that at any voltage levels, electrons and holes are injected into the sample deeply and recombined with each other. As a result, the amount of charge injection can be observed from the corona charged sample's surfaces. As the grid voltage increases, the charge densities on both the bottom surface and the top surface of the corona charged sample increase, which indicates the field dependent mechanism of injection for both surfaces. The second common feature is that the bottom surface always has more charge injection than the top surface for the aluminium ground sample; and it has less injected charge with the gold ground sample. The reason that all the gold ground samples have a larger top surface injection is because all the readings are taken at 1 min decay, the slower decay for gold ground samples caused more charges on the top surface. The surprising observation is that the decay rate on the top surface of corona charged sample is almost the same for either the aluminium ground sample or the gold ground sample; however, there is a big difference on the decay rate of the bottom surface. This indicates that the injection from the corona charged surface is not affected by the ground electrode. However, the injection from the bottom surface is reduced; the decaying rate of the charges on the bottom surface is much slower and therefore reduces the top surface potential decay rate. To understanding the above observation, numerical simulations have been carried out by using different barrier

heights for aluminium and gold ground electrodes, which reflect the difference in work function for aluminium and gold.

## 4.3 Simulation Results

It has been mentioned that the bipolar charge transport model has been widely used to describe the current-voltage characteristics of polymeric insulation since its existence in 1994 [69]. The model contains three important components: charge build-up (or generation), charge transport process with trapping/de-trapping and charge recombination under DC voltage. The results from the numerical modelling can explain the influence of the bottom electrode on injection extraction at the interface during corona charging process and subsequently affect its surface potential decay rate. Details of the model can be found in Chapter 3. The selection of parameters for this model can be found in Table 4-1. To prove that the gold ground can play an essential role in both of the charging and decaying process, all the parameters are kept the same expect the bottom surface injection barrier height from Schottky injection.

Table 4-1 Simulation Parameters

| Parameters (Units) | Value |
|---|---|
| $\mathbf{w_{ei}}$ (eV) | 1.1 |
| Aluminium $\mathbf{w_{hi}}$ (eV) | 1.1 |
| Gold $\mathbf{w_{hi}}$ (eV) | 1.2 |
| Mobility ($\mathbf{m^2V^{-1}s^{-1}}$) | $\mathbf{9 \times 10^{-15}}$ |
| Electrons trapping coefficient ($\mathbf{s^{-1}}$) | $\mathbf{7 \times 10^{-3}}$ |
| Holes trapping coefficient ($\mathbf{s^{-1}}$) | $\mathbf{7 \times 10^{-3}}$ |
| $S_0$ ($\mathbf{m^3C^{-1}s^{-1}}$) | $\mathbf{4 \times 10^{-3}}$ |
| $S_1$ ($\mathbf{m^3C^{-1}s^{-1}}$) | $\mathbf{4 \times 10^{-3}}$ |
| $S_2$ ($\mathbf{m^3C^{-1}s^{-1}}$) | $\mathbf{4 \times 10^{-3}}$ |
| $S_3$ ($\mathbf{m^3C^{-1}s^{-1}}$) | 0 |
| Relative permittivity of LDPE | 2.3 |

The simulation results for aluminium ground sample and gold ground samples are shown in Figure 4-9. It can be clearly seen that the gold ground sample at both – 2 kV and – 8 kV decay slower than the aluminium ground sample. Also, the cross-over phenomenon can be observed for aluminium ground sample and no cross-over is shown for the gold ground sample. These results prove that reducing the amount of charge injection from the bottom layer of the corona charged sample can reduce its corona charged surface potential decay rate, without changing any property from the corona charged side.

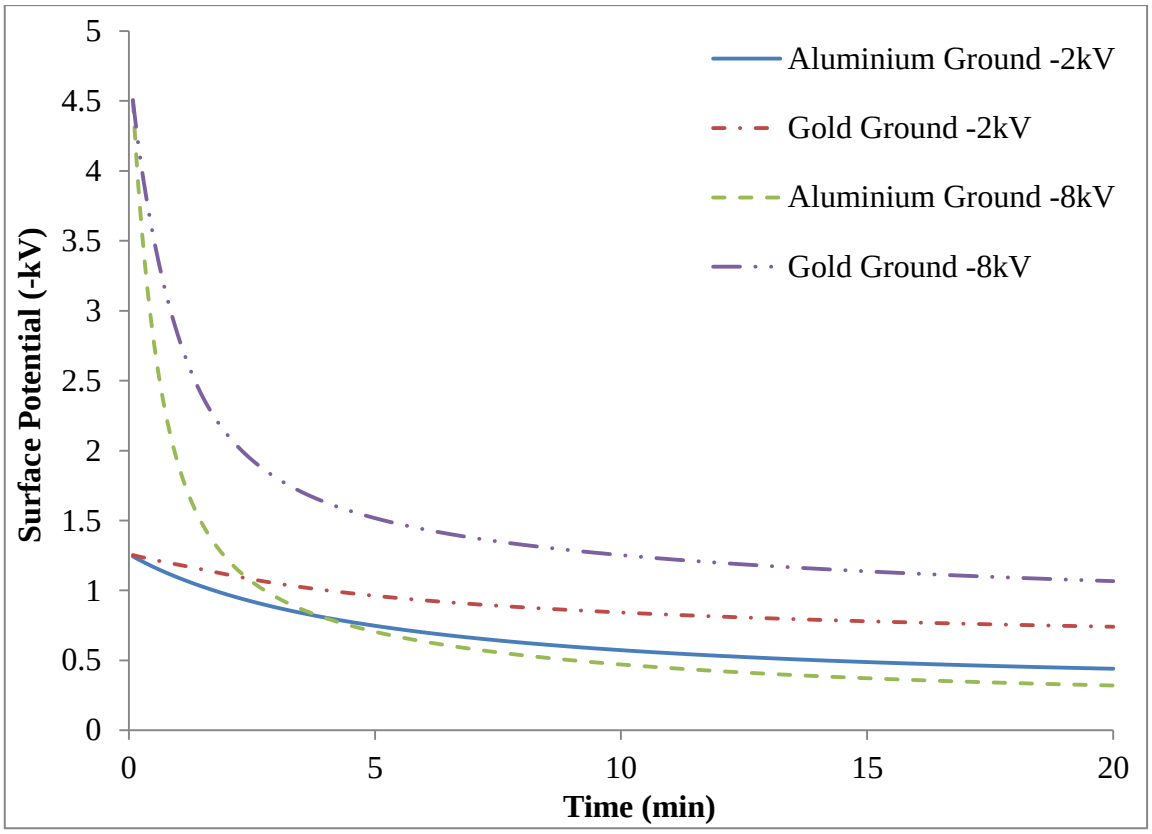


Figure 4-9 Simulation results for aluminium ground sample and gold ground sample

## 4.4 Conclusions

The effect of the bottom surface injection of corona charged LDPE has been studied using four different techniques: surface potential decay measurement, corona charging current measurement, space charge measurement and bipolar charge transport model. The surface potential decay measurement clearly shows the different decay rates of the aluminium ground sample and the gold ground sample. The corona charging current

measurement shows that the ground electrode injection is always smaller than the aluminium ground electrode injection and the space charge measurement clarifies the charge density along both top surface and bottom surface of the sample. Finally, the simulation results prove that the reduction of the bottom surface injection can make the surface potential decaying slower. Combining all the results, it can be concluded that bipolar charge injection is the key factor during the corona charging and decaying processes and the injection from the bottom surface of the sample must be taken into account.

# Chapter 5 Surface Potential Decay with Different Polarity and Charging Times

## 5.1 Effect of Different Polarity

Figure 5-1 shows the effect of charging polarity to the surface potential decay results for 2 min charging time with several different voltage levels. It can be clearly seen that positive corona charging leads a smaller decay than the negative corona charging. One hypothesis [66] states that during the corona charging period, the negative polarity contains both electrons and negative ions; however, for positive polarity, it only contains positive ions. Therefore, the charge injection of positive polarity is smaller than negative polarity, which results a slower surface potential decay. As the charge injection from the bottom electrode cannot be neglected; the corona charging current had been measured as well. It can be seen from Figure 5-2 that the current for positive corona charge is always smaller than negative corona charge. This graph is very similar to the gold ground electrode results in Figure 4-4, which explains why positive corona has a slower surface potential decay from another point of view.

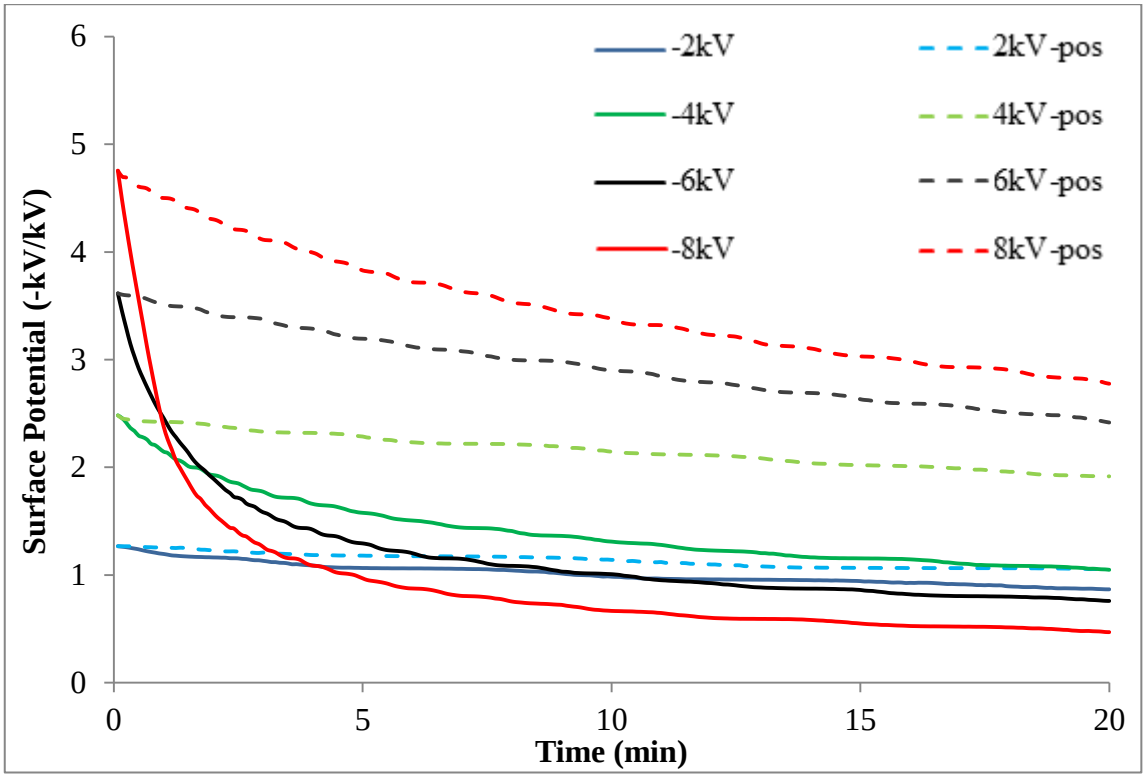


Figure 5-1 Surface potential decay for negative polarity and positive polarity

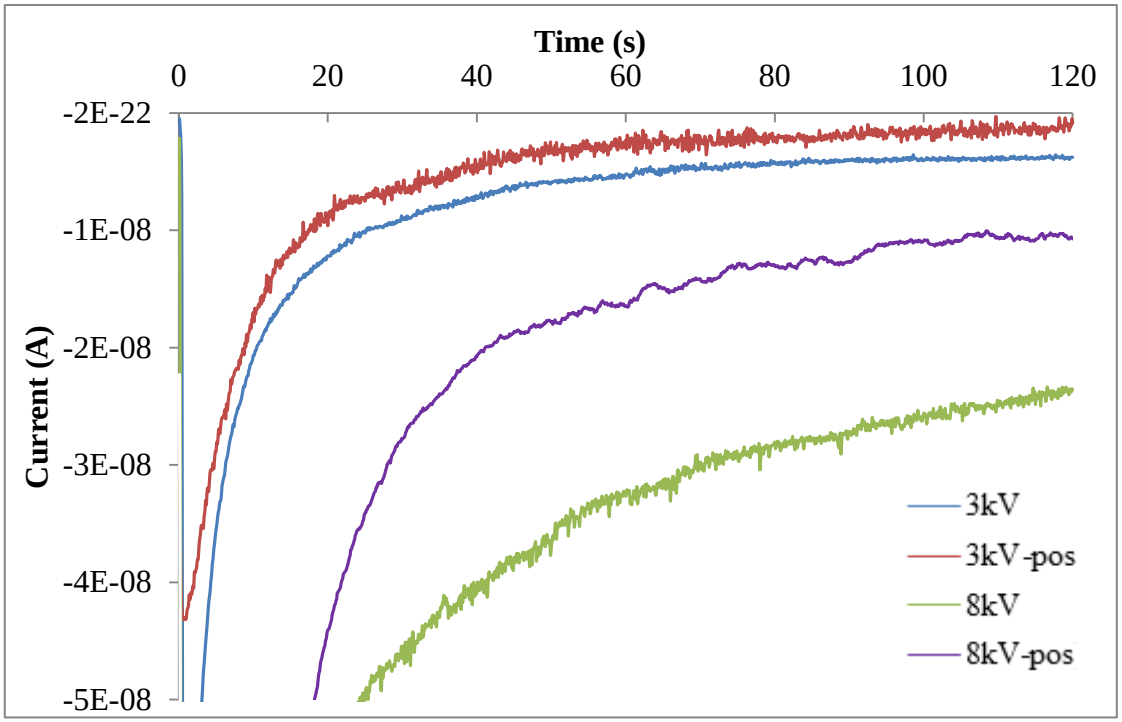


Figure 5-2 Corona charging current for negative polarity and positive polarity

## 5.2 Effect of Different Charging Time

### *5.2.1 Surface Potential Decay Measurements*

The experiment on the effect of different charging time to the surface potential decay was initially planned to using only one charging voltage level. However, there is new phenomenon observed on the – 8 kV results.

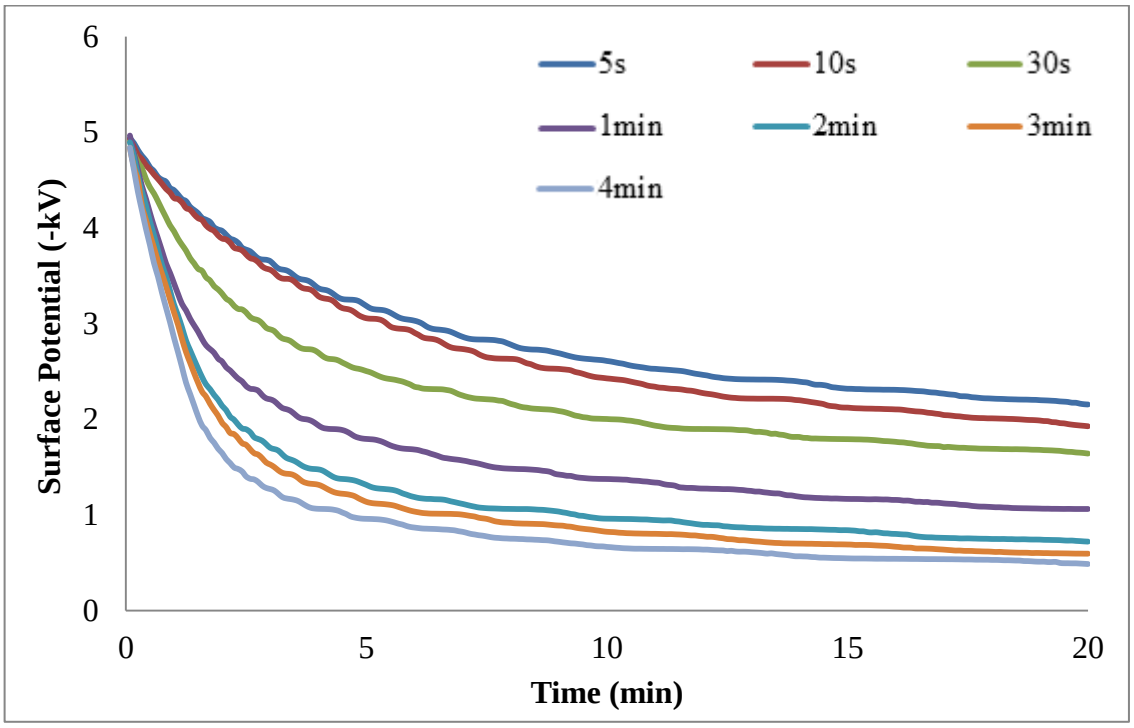


Figure 5-3a Surface potential decay of LDPE after corona charged under a grid voltage of – 8 kV for different times

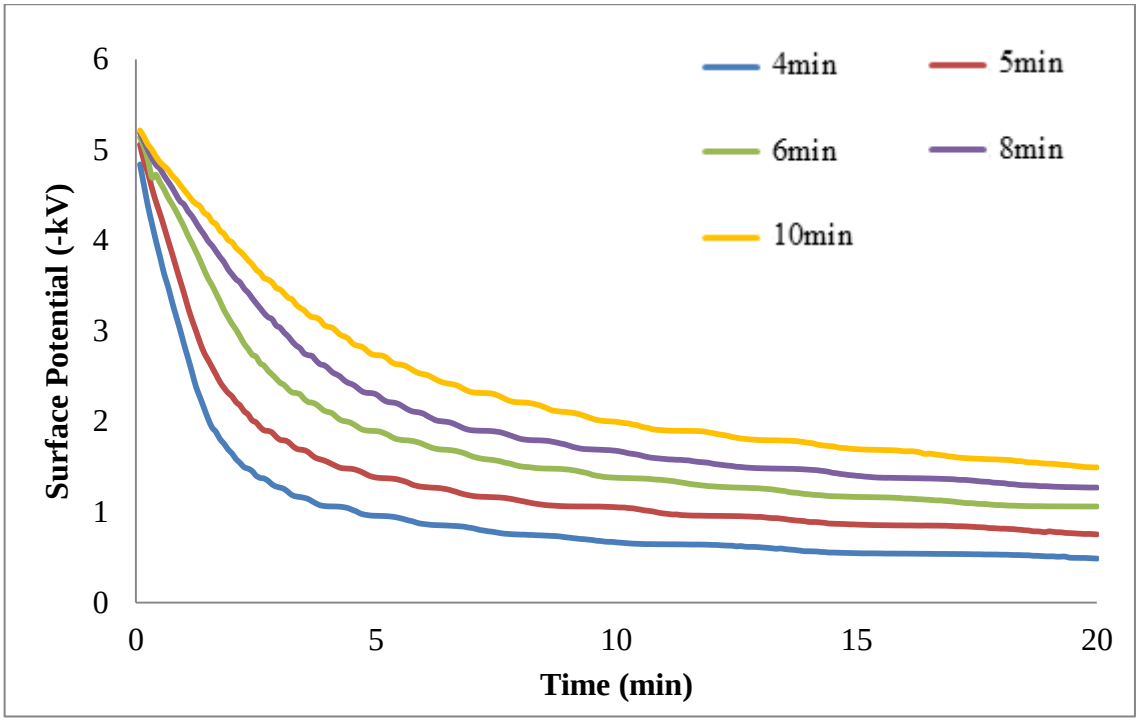


Figure 5-3b Surface potential decay of LDPE after corona charged under a grid voltage of – 8 kV for different times

From Figure 5-3, it can be seen that the experiment results completely different from the prediction of the theory [80], which is the longer charging time leads to a faster surface potential decay. This is true from the first diagram where the charging time is shorter than 4 min. However, when the charging time becomes longer than 4min, the longer charging time will then lead to a slower surface potential decay. Therefore, experiments on - 6 kV, - 4kV and – 2 kV was carried out to further verify the observation.

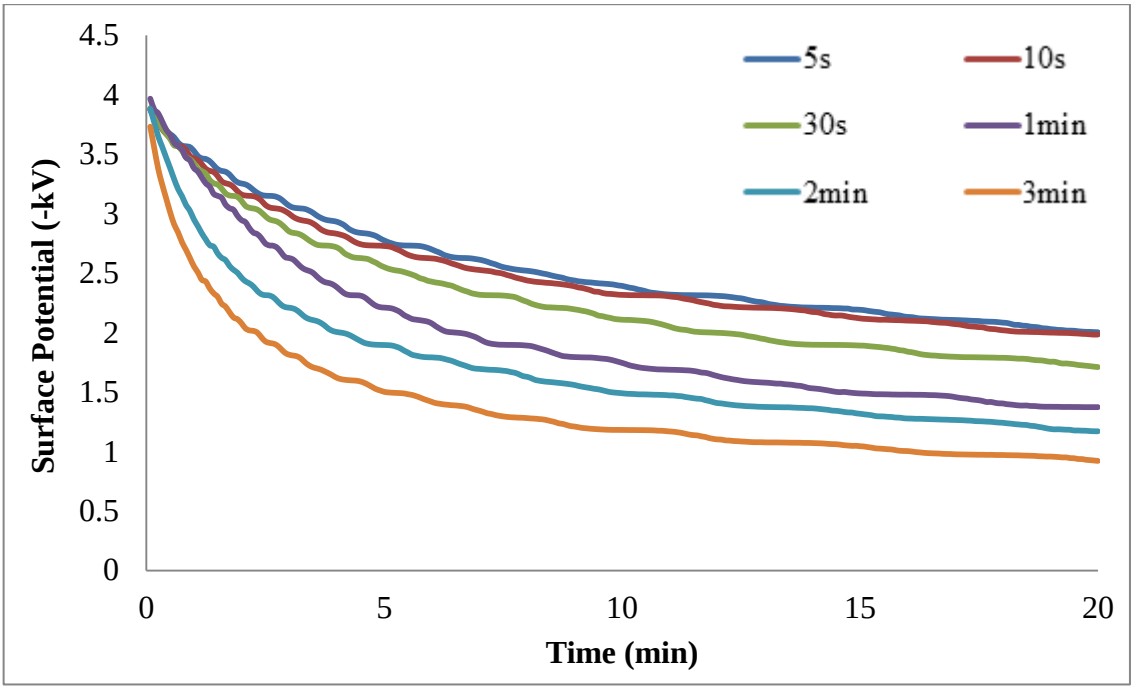


Figure 5-4a Surface potential decay of LDPE after corona charged under a grid voltage of – 6 kV for different times

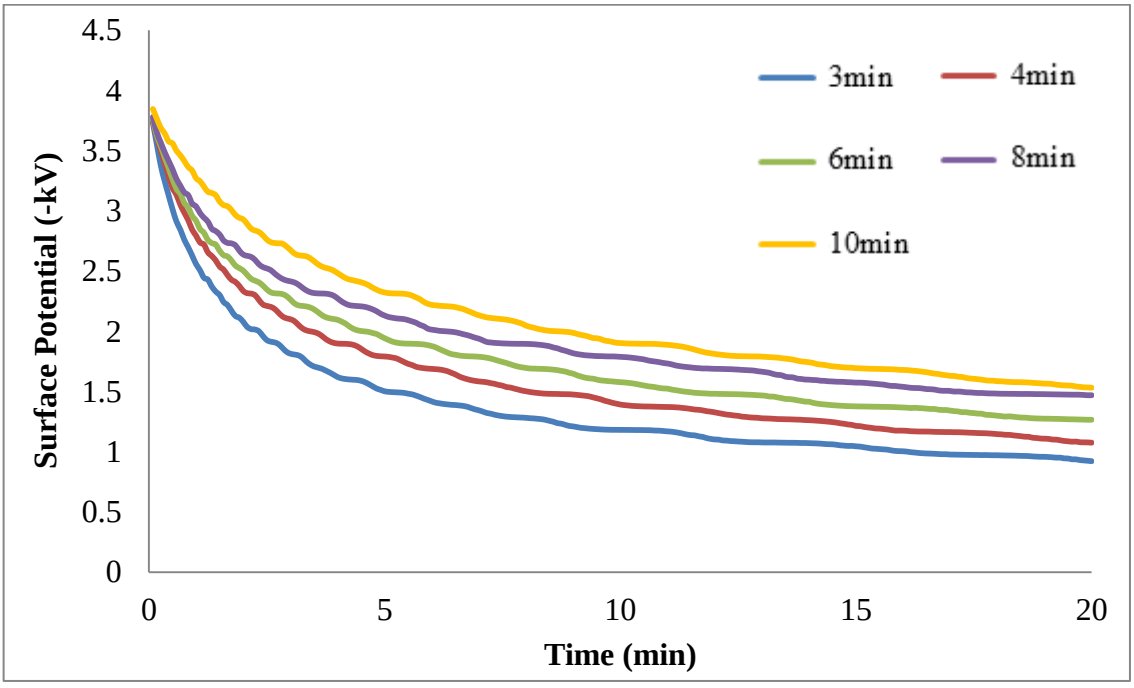


Figure 5-4b Surface potential decay of LDPE after corona charged under a grid voltage of – 6 kV for different times

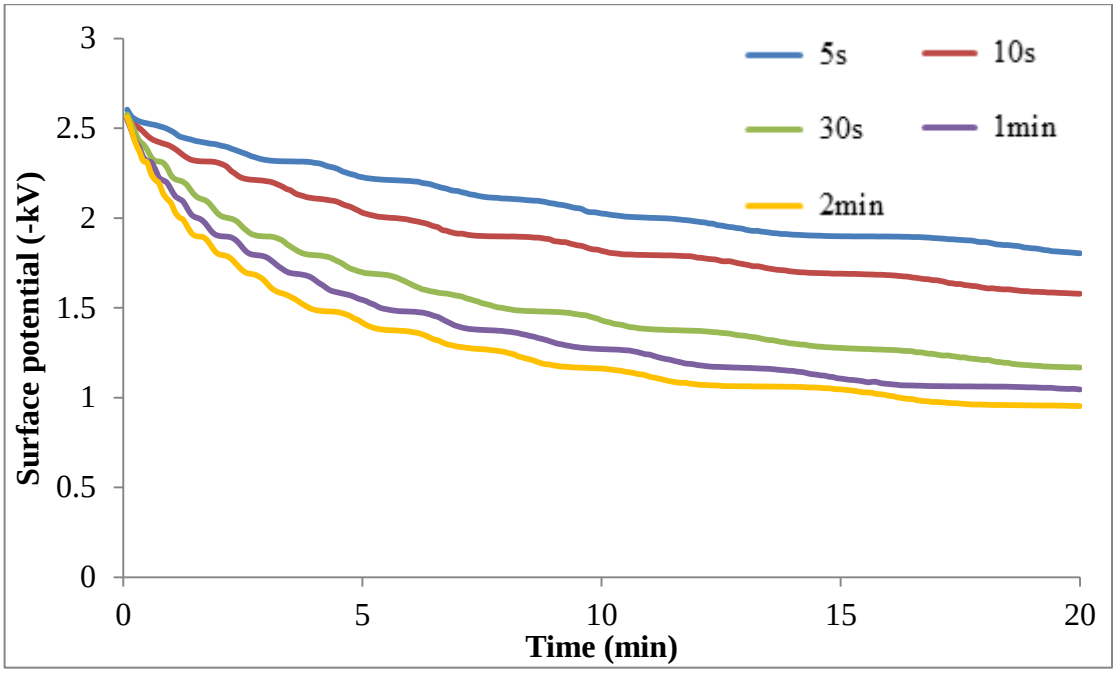


Figure 5-5a Surface potential decay of LDPE after corona charged under a grid voltage of – 4 kV for different times

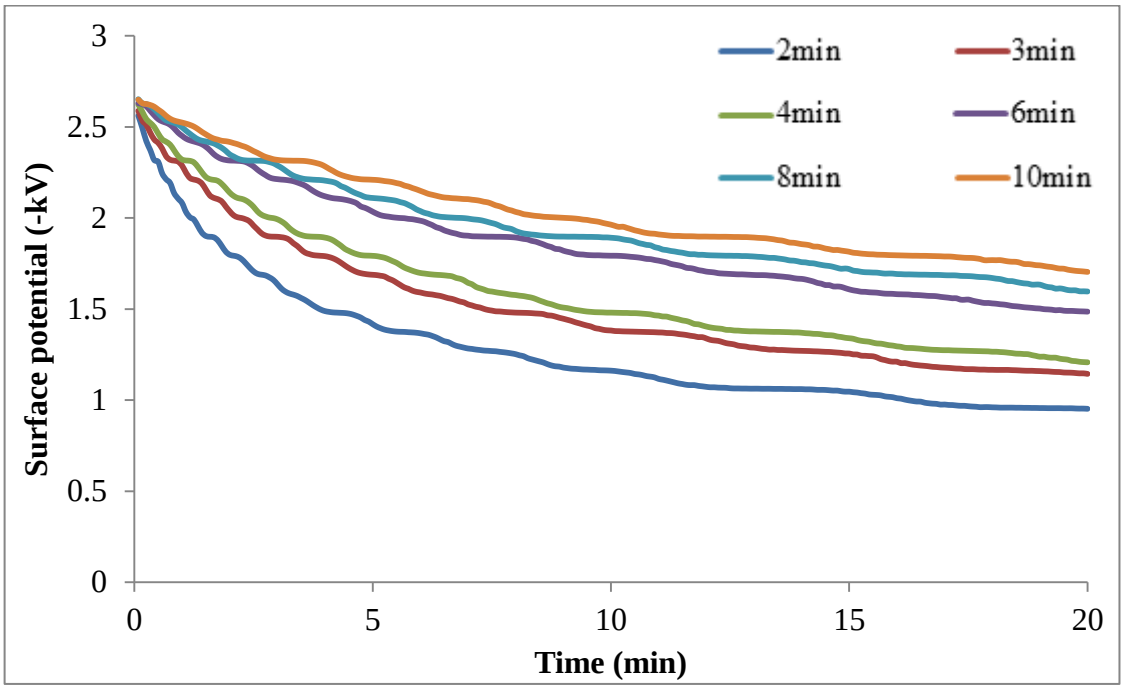


Figure 5-5b Surface potential decay of LDPE after corona charged under a grid voltage of – 4 kV for different times

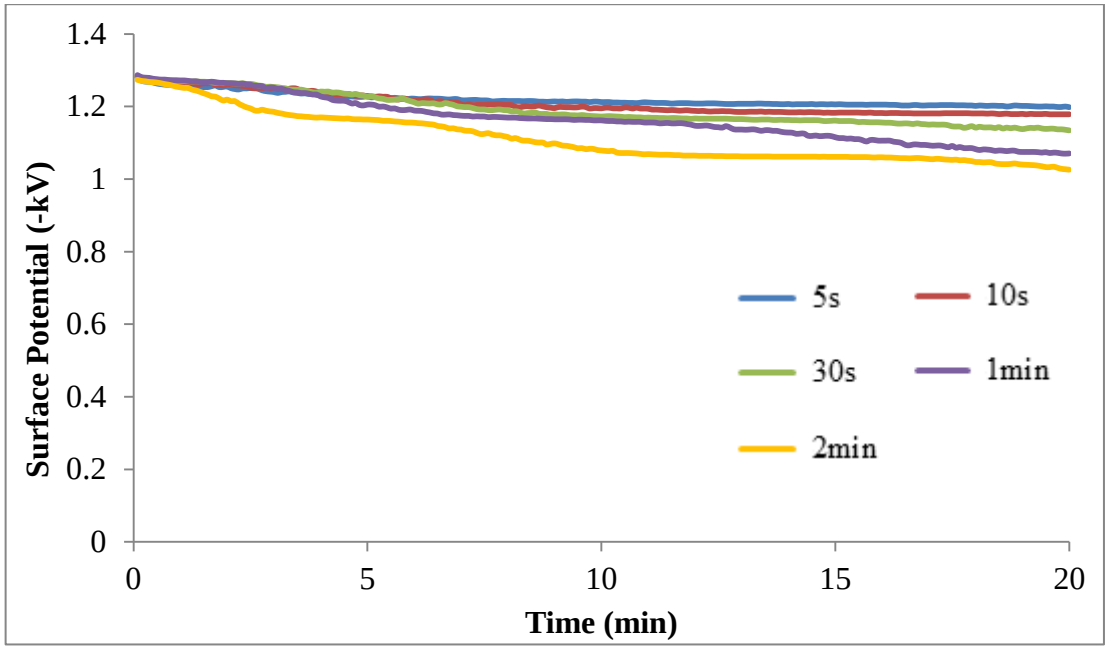


Figure 5-6a Surface potential decay of LDPE after corona charged under a grid voltage of – 2 kV for different times

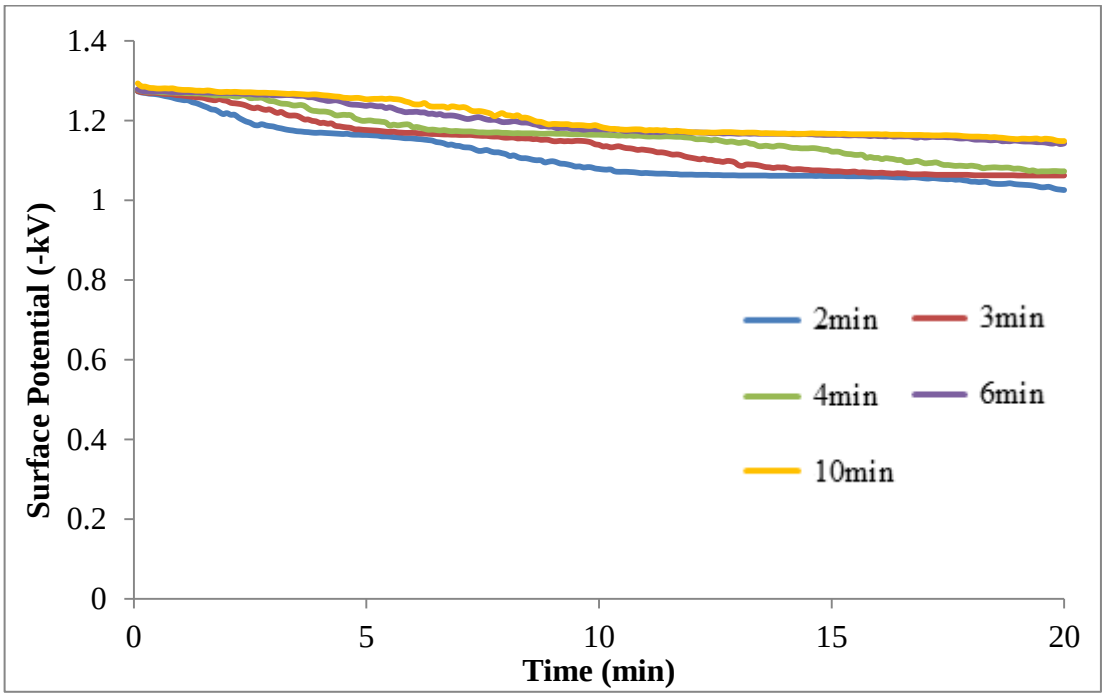


Figure 5-6b Surface potential decay of LDPE after corona charged under a grid voltage of – 2 kV for different times

The – 6kV, - 4kV and – 2kV results given above show a similar trend to – 8kV, but the turning point is changed from 4 min to 3 min or 2min charging period. One probability may be explained by the fact that the charge carriers are more likely to be trapped under a very long charging time. This will be further discussed in section 5.3.

### *5.2.2 PEA Measurements*

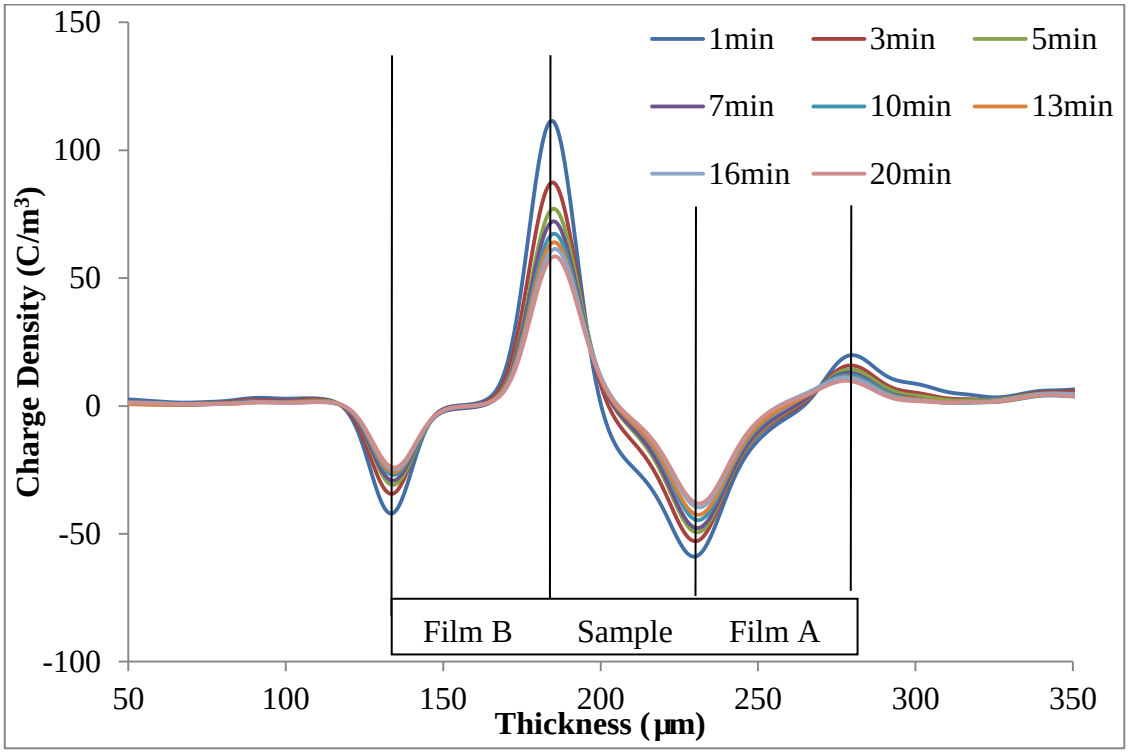


Figure 5-7a Space charge distribution for − 8 kV with 5 s charging time

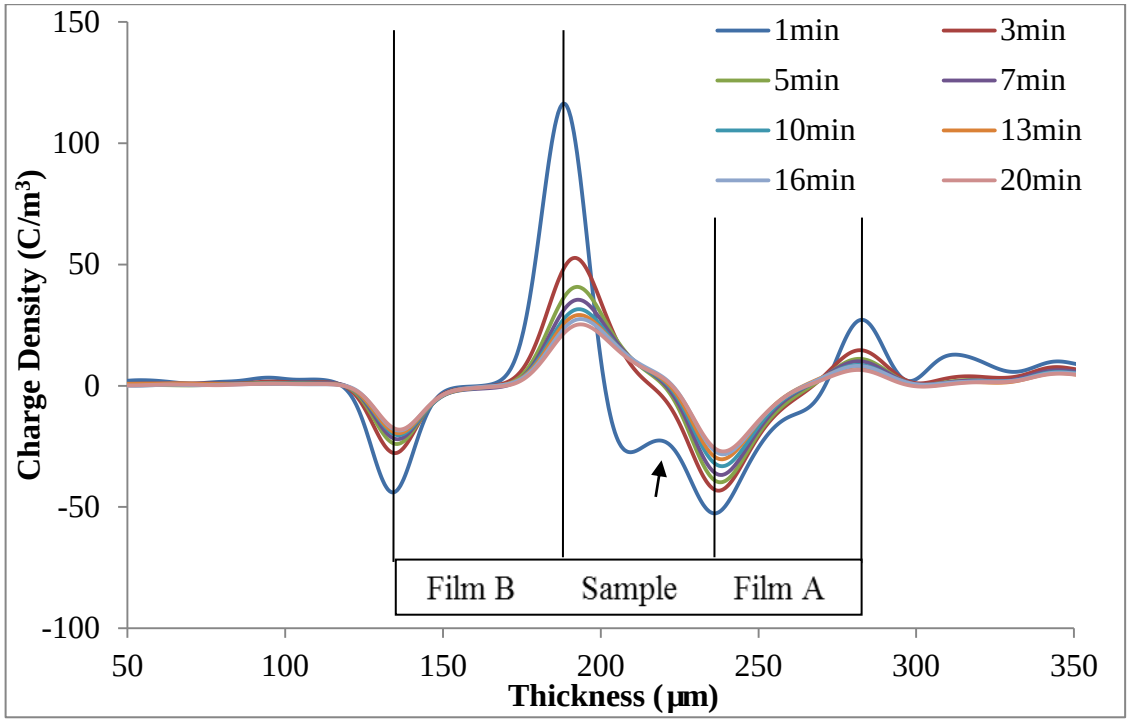


Figure 5-7b Space charge distribution for − 8 kV with 4 min charging time

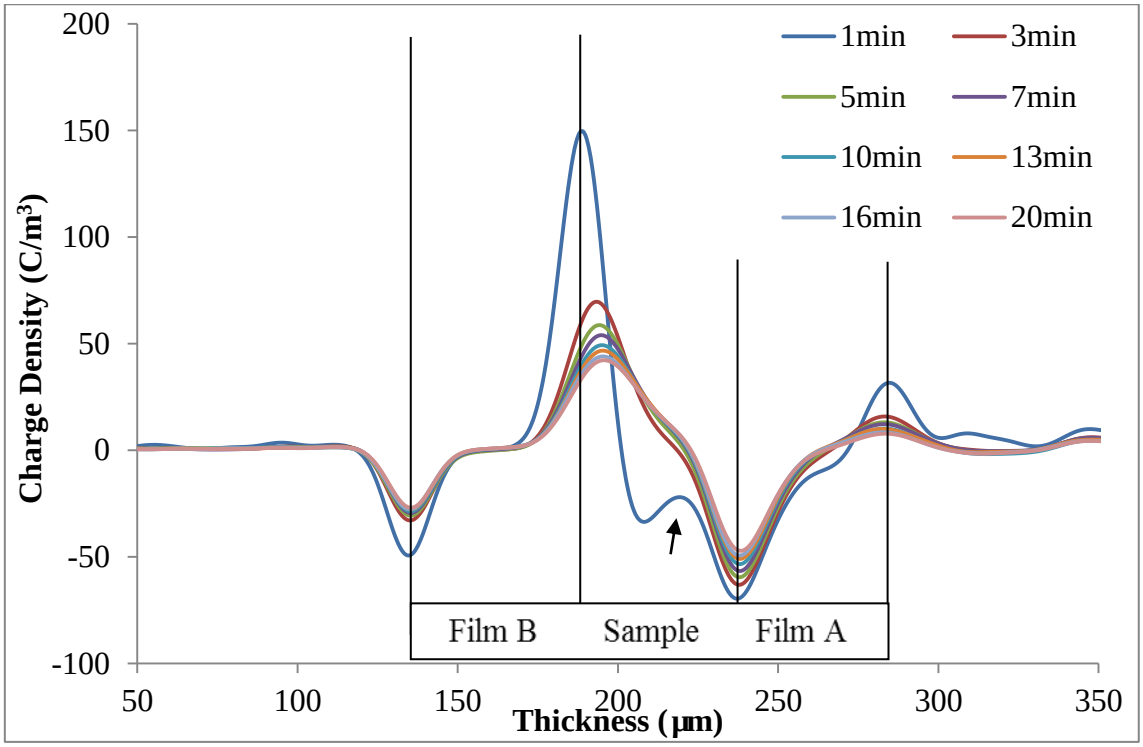


Figure 5-7c Space charge distribution for − 8 kV with 10 min charging time

Figure 5-7 shows space charge distributions following the corona charging at -8 kV for 5 s, 4 min and 10 min respectively. The charges at both electrodes of the sample of the 4

min results decay a lot faster than the 5 s and 10 min one, which can represent the faster surface potential decay. It can be observed from Figure 5-7b and Figure 5-7c that the 1 min charge distribution curve has a small difference from Figure 5-7a, which is pointed with an arrow. This phenomenon can only be observed for − 8 kV charging voltage with 4 min or longer charging time. Observation of charge packet in LDPE had been done in our laboratory [81]. It was found that under the same environment conditions, a positive charge packet can be observed in 15 s when the applied electric exceeds 50 kV/mm and the charge packet is mainly caused by charge injection. The size of the charge packet will be increasing with the electric field strength. It can be speculated that there may be a positive charge packet occurring in the sample, and it reduces the total negative charge density at the arrow in Figure 5-7b and Figure 5-7c; therefore the charge distribution curve results differently as in Figure 5-7a.

## 5.3 Discussion

### *5.3.1 Double Exponential Decay Analysis*

It had been reported that the exponential decay equation (20) can be used to fit the decay curves for a shorter time; however, there is a divergence at longer times [18].

$$\mathrm{V(t)} = \mathrm{A exp(-Bt)} \tag{20}$$

*V(t)* is the surface potential at any point of time after a certain decay period, parameter *A* is the initial surface potential after charging and parameter *B* is the constant of decay time. After applying equation (20) into the surface potential decay experimental results, it was observed that this equation cannot be fitted to the decay curves. Therefore, a new equation needs to be introduced for this purpose.

It is believed that the injected charge can be captured by traps on its way towards to the opposite electrode. Roughly, there are two types of charges inside the corona charged material: mobile and trapped. These two types of charges act very differently. It is known that mobile charges can easily travel across the sample, and the trapped charges stay inside the material for much longer. It can be assumed that there are two types of decay processes occurring simultaneously and being controlled by two types of charge. Therefore, a double exponential decay equation can be applied here:

$$\mathrm{V(t)} = \mathrm{A_m\, exp(-B_m t) + A_t exp(-B_t t)} \tag{21}$$

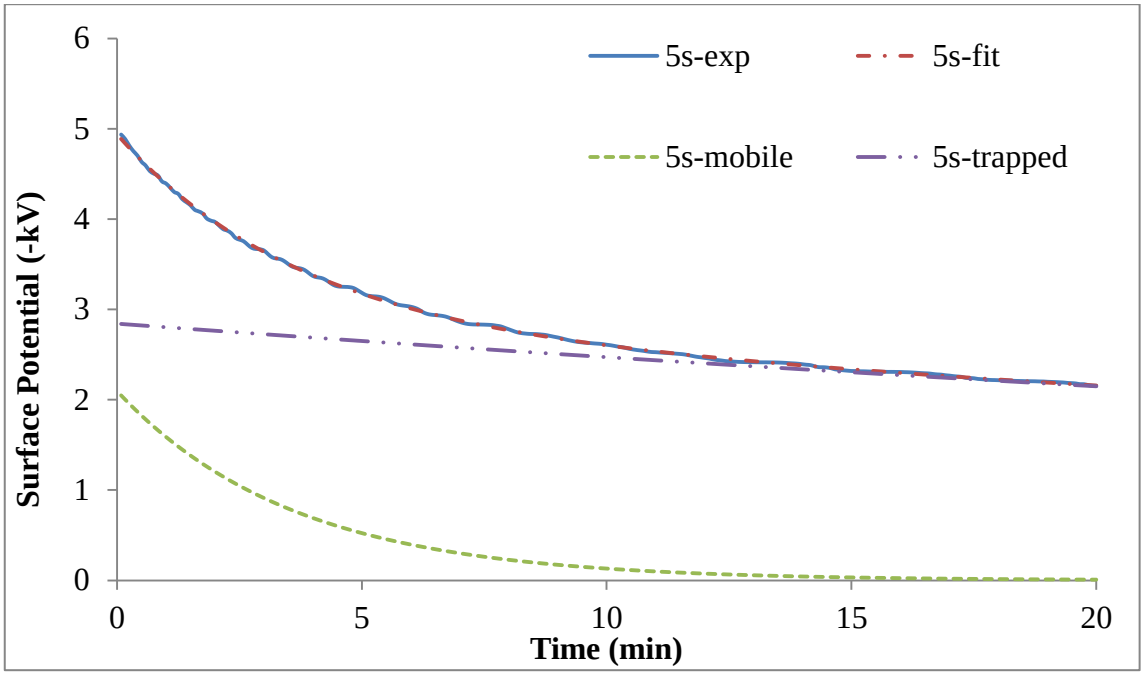


Figure 5-8a. Double exponential decay fitting for − 8 kV 5s

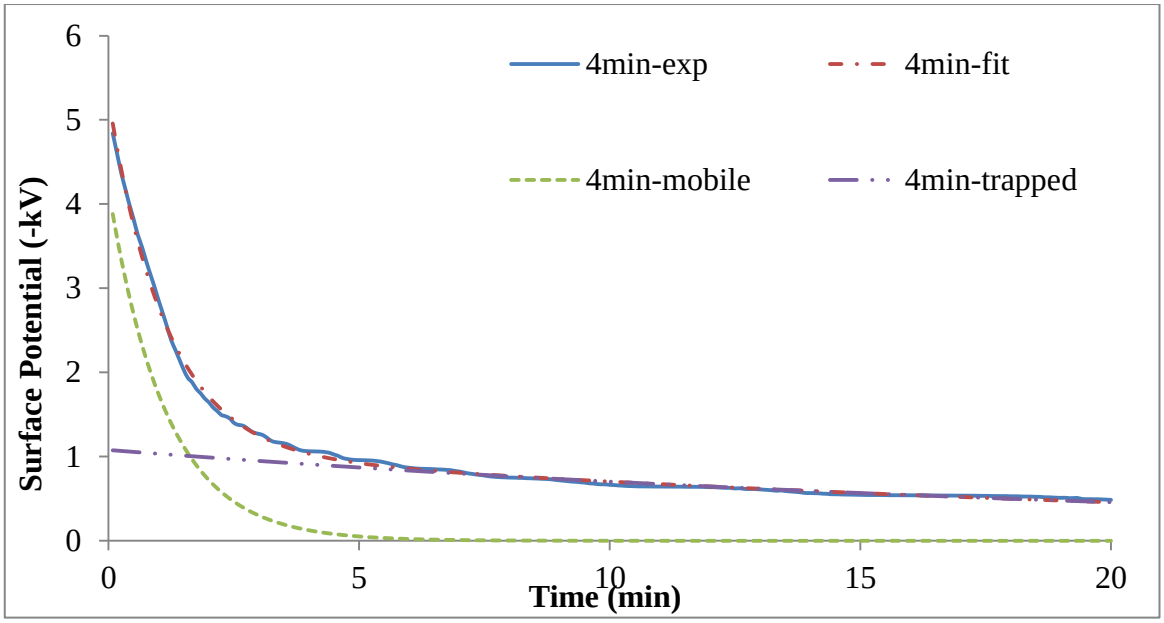


Figure 5-8b. Double exponential decay fitting for − 8 kV 4 min

Parameters from equation (21) were calculated by 'nlinfit' function in MATLAB. All the parameters were focused to be positive and the best-fitted result was selected. Equation (21) has two parts: m is for mobile charges and t is for trapped charges. The fitted results and parameters can be found in Figure 5-8 and Figure 5-9. Figure 5-8 clearly shows that equation (21) can match the experimental results very well for both short and long charging times and it can also reveal the detailed change in mobile

charges and trapped charges with time. The decay process of surface potential is determined by the decay of both mobile and trapped charges. The decay of the mobile charges dominate the first 5 to 10 min. After this interval, the surface potential decay is totally governed by the trapped charges. It can be seen from Figure 5-9 that $A_m$ and $A_t$ represent the amount of mobile charges and trapped charges after remove the applied voltage respectively; $B_m$ and $B_t$ show the constant of decay time for mobile charges and trapped charges. Figure 5-9a shows that the amount of mobile charges is increasing with longer charging time and decreasing if the charging time exceeds 4 min. As the sum of $A_m$ and $A_t$ is the same, the amount of deep charge have a completely different trend. Figure 5-9b represents the decay speed for both charges, and it can be found that mobile charges always decay faster than trapped charges.

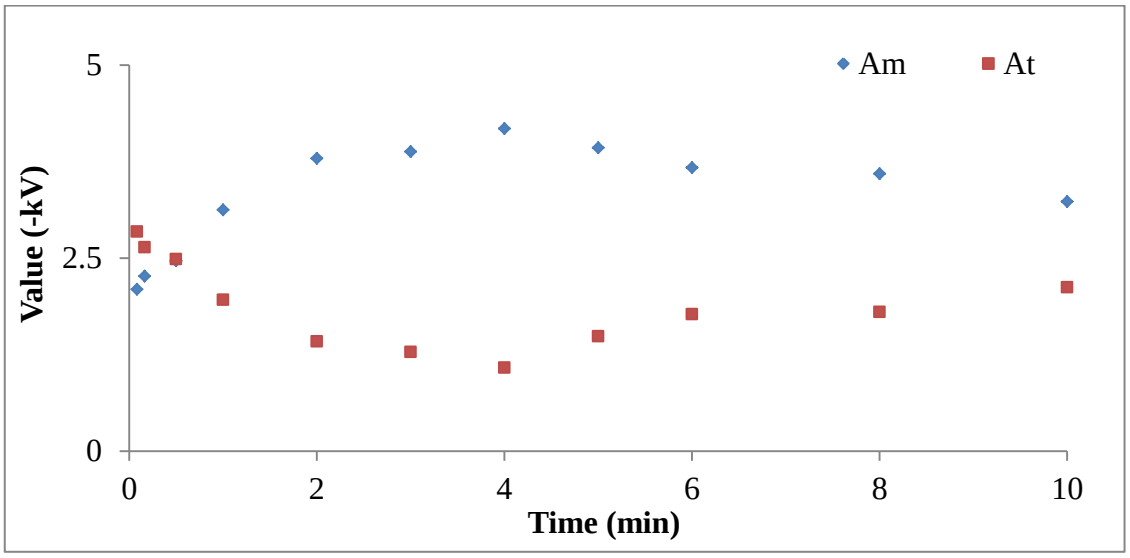


Figure 5-9a. Parameters A for equation (21) − 8 kV

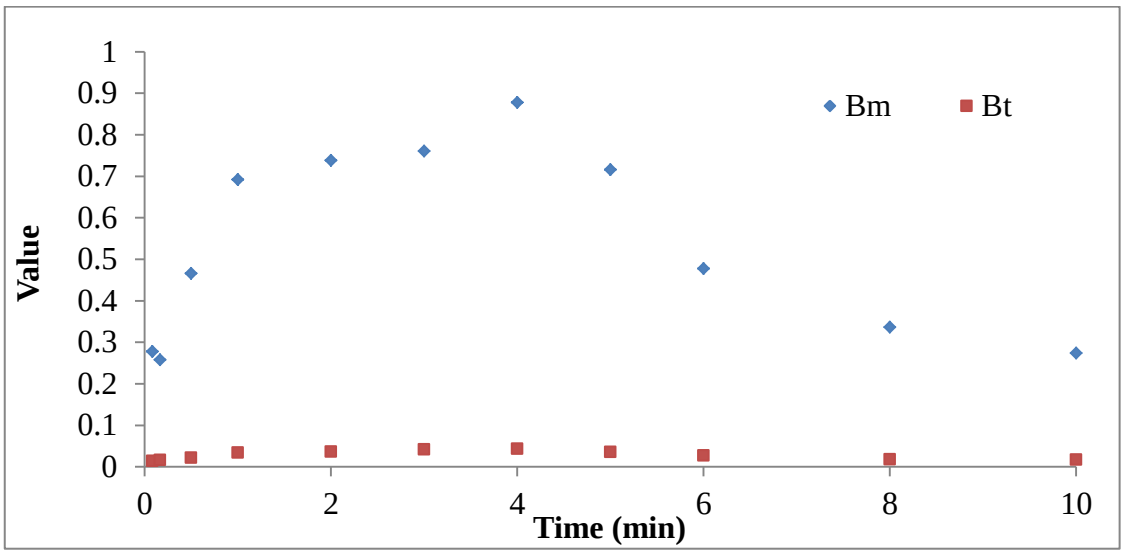


Figure 5-9b. Parameters B for equation (21) − 8 kV

### *5.3.2 Simulation Results*

To find out how the parameters in the model affect the surface potential decay results, two simulations had been done: (i) different charge injection and (ii) different charging time. The rest of the parameters will be kept the same such as trap coefficient, trap density, mobility etc. The results are summarised in Figure 5-10.

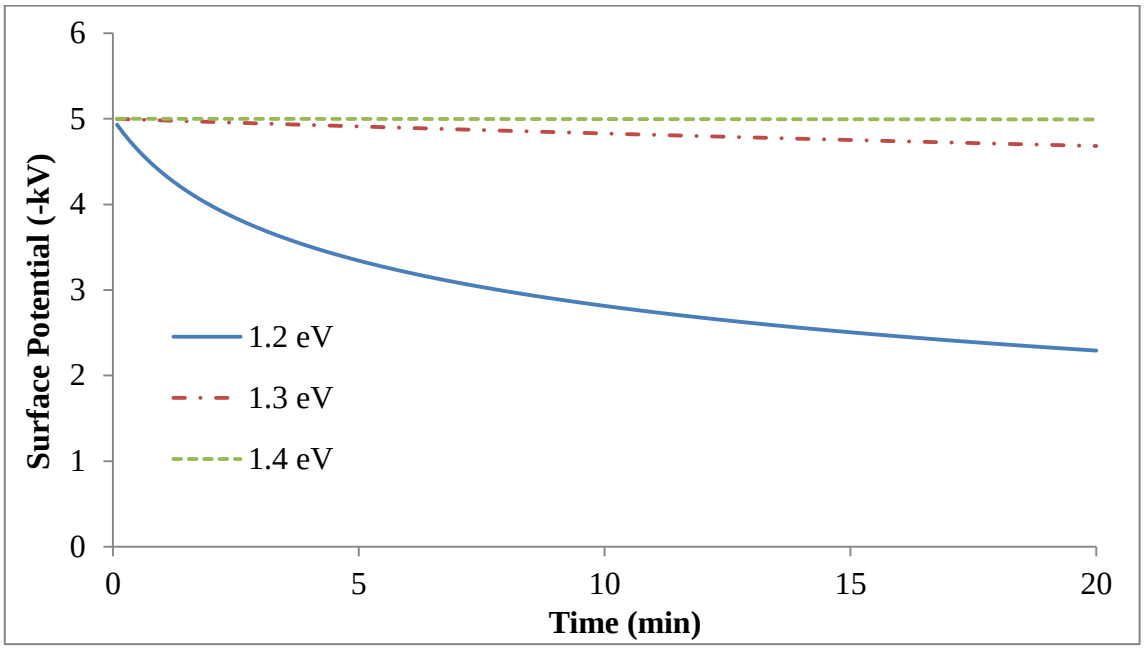


Figure 5-10a. Simulation results for different barrier heights with 4 min charging time

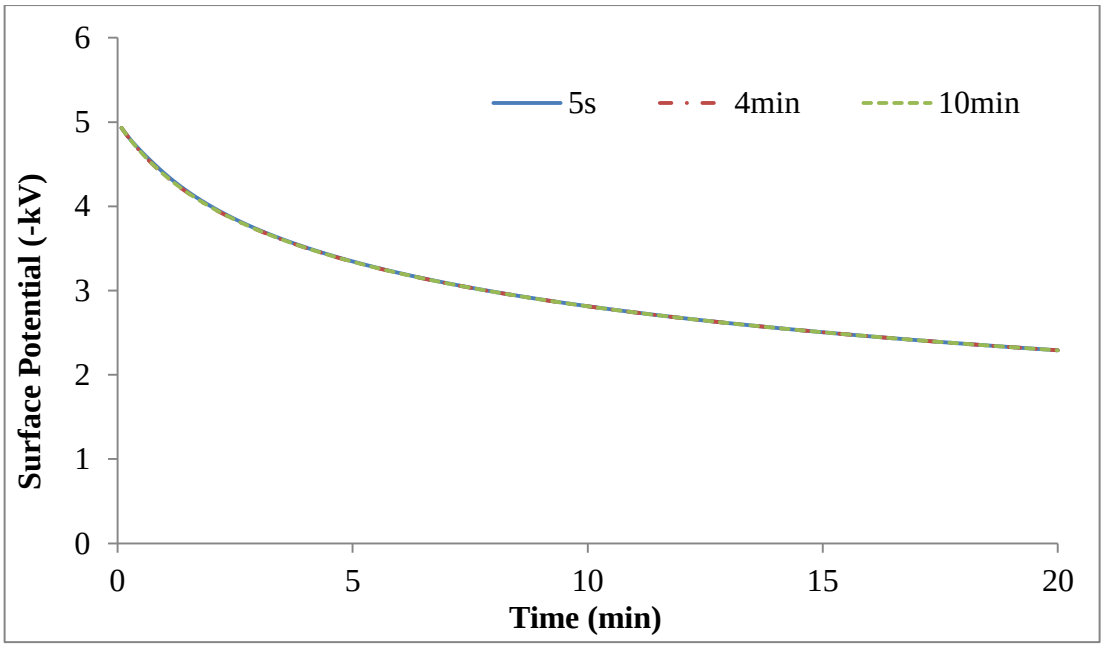


Figure 5-10b. Simulation results for different charging times with 1.2 eV injection barrier height

It can be noticed that larger charge injection (smaller injection barrier height) will lead to a faster decay (Figure 4-10a); however, if the charge injection barrier height was kept the same, a longer charging time would not affect the surface potential decay results much (Figure 5-10b), which is different from the experimental observation. In section 5.2.2, the charge packet has been only observed when the corona charging time has reached 4 min, which means that the charge injection before 4 min has not reached the largest injection yet. As the initial surface potential under the same charging voltage is the same even with different charging time, it is likely that the charges are accumulating at the sample's surface first, and then they are injected into the material. The amount of charge injection will increase with charging time until it reaches a maximum. Therefore, the amount of mobile charges inside the sample will increase and affect the decrease of trapped charges. However, the phenomenon when charging time exceeds 4 min cannot be explained by the model only.

### *5.3.3 Trap Energy Distribution*

It has been reported that charge trapping and detrapping are closely related to the trap distribution in terms of both space and energy [82]. It is well known that density of trap states near the surface is much higher than that in the bulk of a material. To simplify the analysis, it was assumed that surface trap states are uniformly distributed in a thin layer. After a sample was charged, charges in the material started to release as called detrapping. The research indicates that the charge density has a correlation with the current, and generally, charge condition inside the material can be represented according to the surface potential [83]. The current density can be obtained by

$$\mathrm{j} = \frac{\varepsilon_0 \varepsilon}{L} \frac{dV_s(t)}{dt} \tag{22}$$

Therefore, the relationship between the attenuation of surface potential and the current is

$$\mathrm{i(t)} = \mathrm{C} \frac{dV_s(t)}{dt} \tag{23}$$

where $\mathrm{C} = \varepsilon_0 \varepsilon A/L$; $A$ is the surface area, $L$ is the thickness of the sample, $\varepsilon_0$ is the dielectric constant under vacuum, $\varepsilon$ is the relative dielectric constant and $V_s$ is the surface potential [84].

It was mentioned that LDPE contains both deep traps and shallow traps. After the applied voltage was removed, charges in the shallow traps were released initially, and later the charges were released from the deep traps. One assumption is that the charges cannot be trapped again once it is detrapped. The trap energy level $E_t$ and the trap density $N(E_t)$ can be calculated by

$$E_t = kT \ln \nu t \tag{24}$$

$$N(E_t) = \frac{\varepsilon_0 \varepsilon t}{qL\delta kT f_0(E_t)} \frac{dV_s(t)}{dt} \tag{25}$$

where $K$ is the Boltzmann's constant $8.617 \times 10^{-5}$ eV/K, T is the absolute temperature K, $\nu$ is the attempt to escape frequency of trapped charge $4.17 \times 10^{13}$ $s^{-1}$, $q$ is the electron charge $1.6 \times 10^{-19}$ C, $\delta$ is the thickness of top charge layer 2 μm, $f_0(E_t)$ is the original occupation rate of traps inside the material 0.5 [85]. To find out the trap energy distribution for 4min charging or longer, calculation of equations (24) and (25) is shown in Figure 5-11.

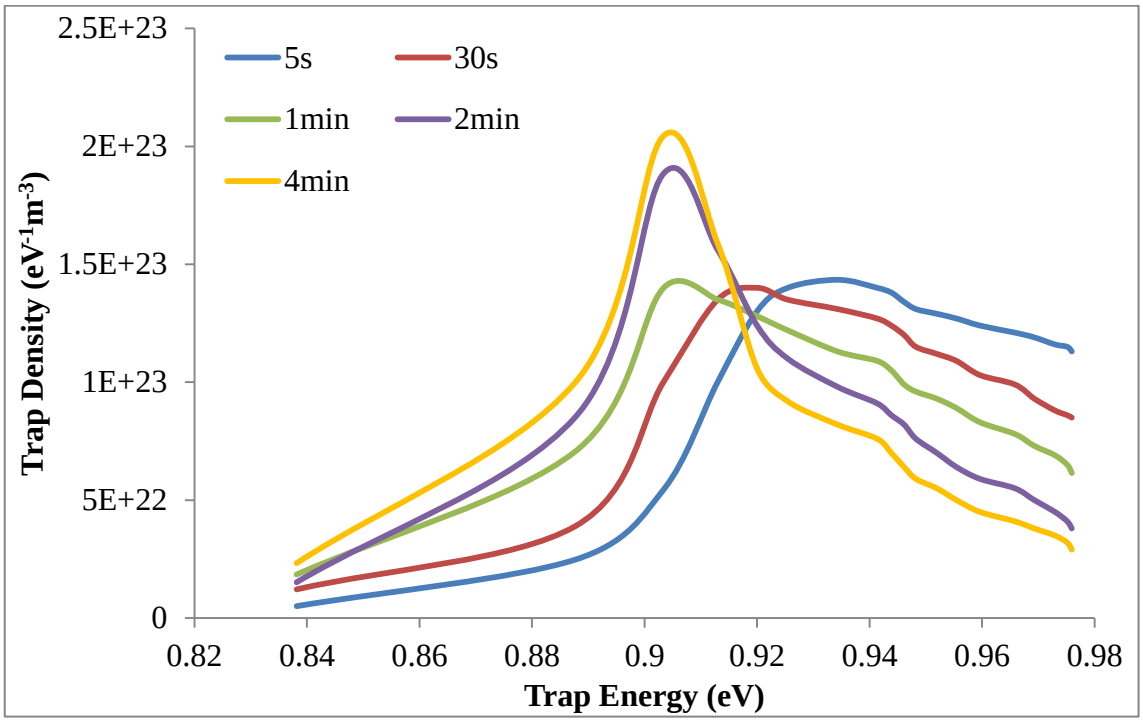


Figure 5-11a. Trap energy distribution for − 8 kV for different times

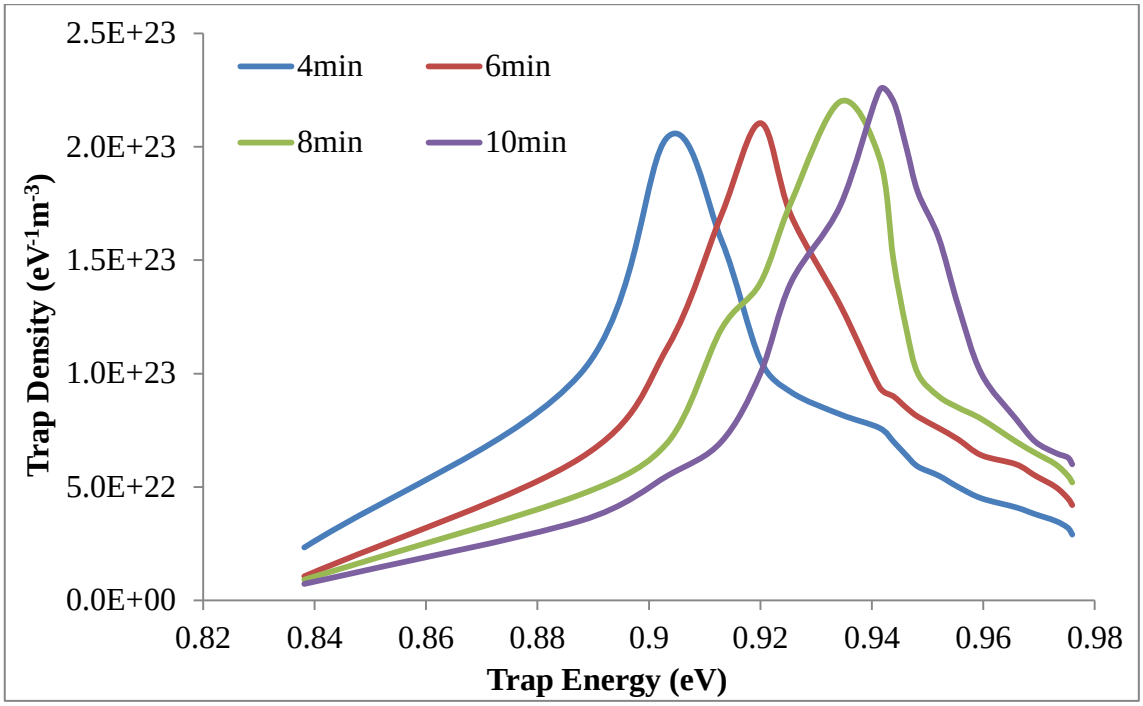


Figure 5-11b. Trap energy distribution for − 8 kV for different times

Figure 5-11a represents that the peak trap density is moving from higher trap energy to lower trap energy while increasing the corona charging time. This is because that the increasing of the charge injection can help the charges cross the trap more easily and therefore results the decrease of trap energy using the plot equation. The same mathematical agreement can be found in Figure 5-9a. Figure 5-11b clearly shows that the trap energy increases with charging time after 4 min charging. This result convinces the increasing number of trapped charges in Figure 5-9a as well. It has been reported that aged sample has a slower decay than normal sample due to the change of chemical structure [86]. In this case, the surface of the sample can be changed by constantly corona charging the sample. Therefore, it may generate few deep traps on the surface. As the charging time increases, the sample's surface can be damaged more and may start affect the structure inside the dielectrics. Therefore, a slower decay can be observed if the charge injection reaches the maximum and the material is continuing charging. To make this hypothesis more reliable, chemical analysis of corona charged product can be carried on.

# Chapter 6 Simulation on Surface Potential Decay

## 6.1 Mathematical Analysis on Experimental Results

For curves had been selected from Figure 4-1 (- 2 kV, - 4 kV, - 6 kV and - 8 kV) to be simulated by using bipolar charge transport model. Before the attempt made on simulation, a mathematical analysis from section 5.3.1 had been done to help the selection of parameters.

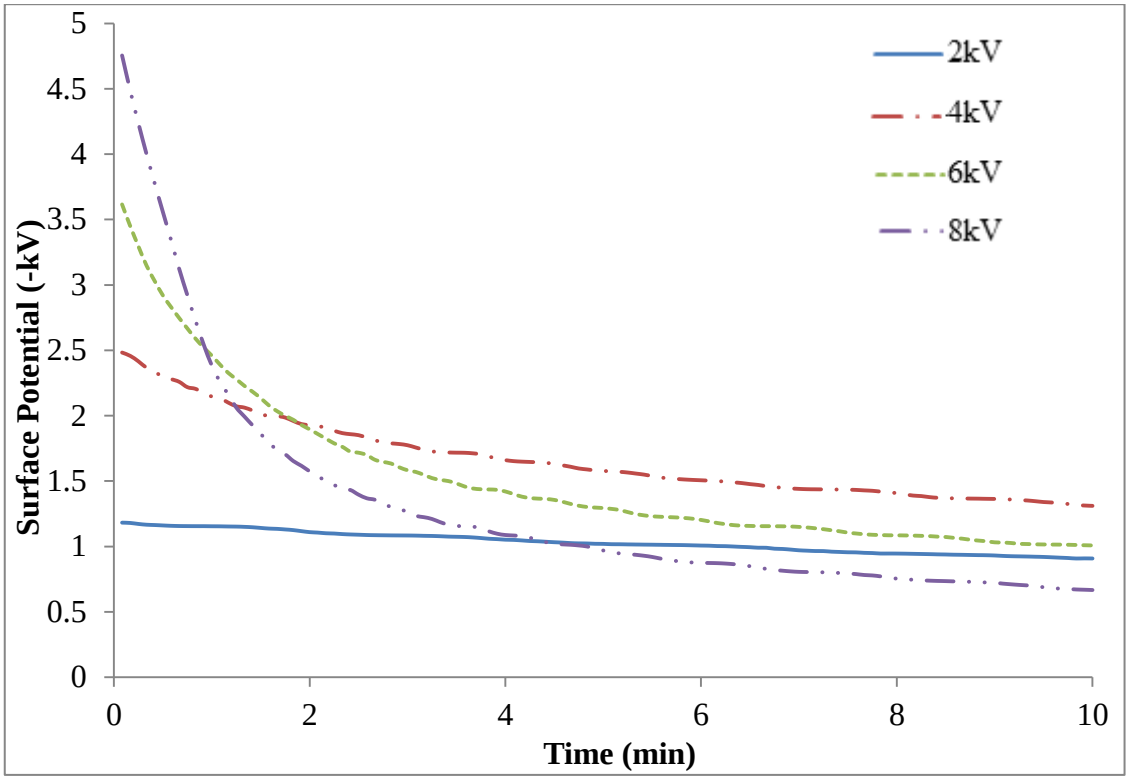


Figure 6-1 Selected experimental results from Figure 2-6.

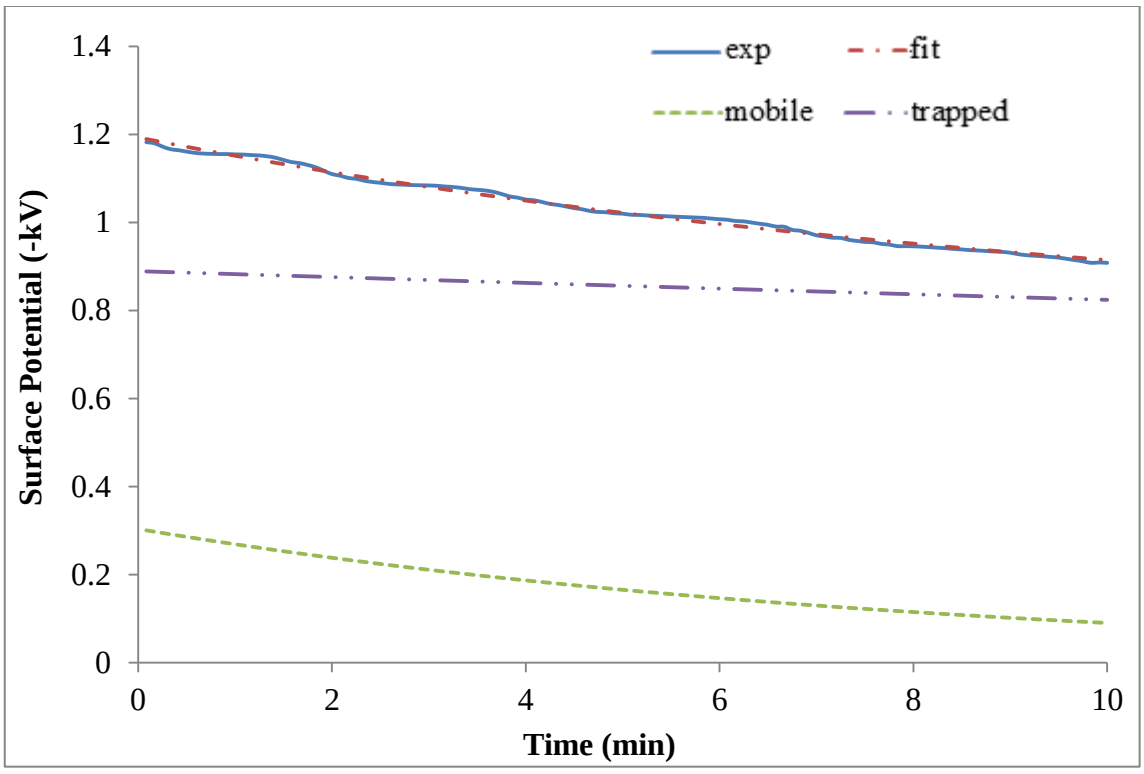


Figure 6-2a Mathematical results for – 2 kV.

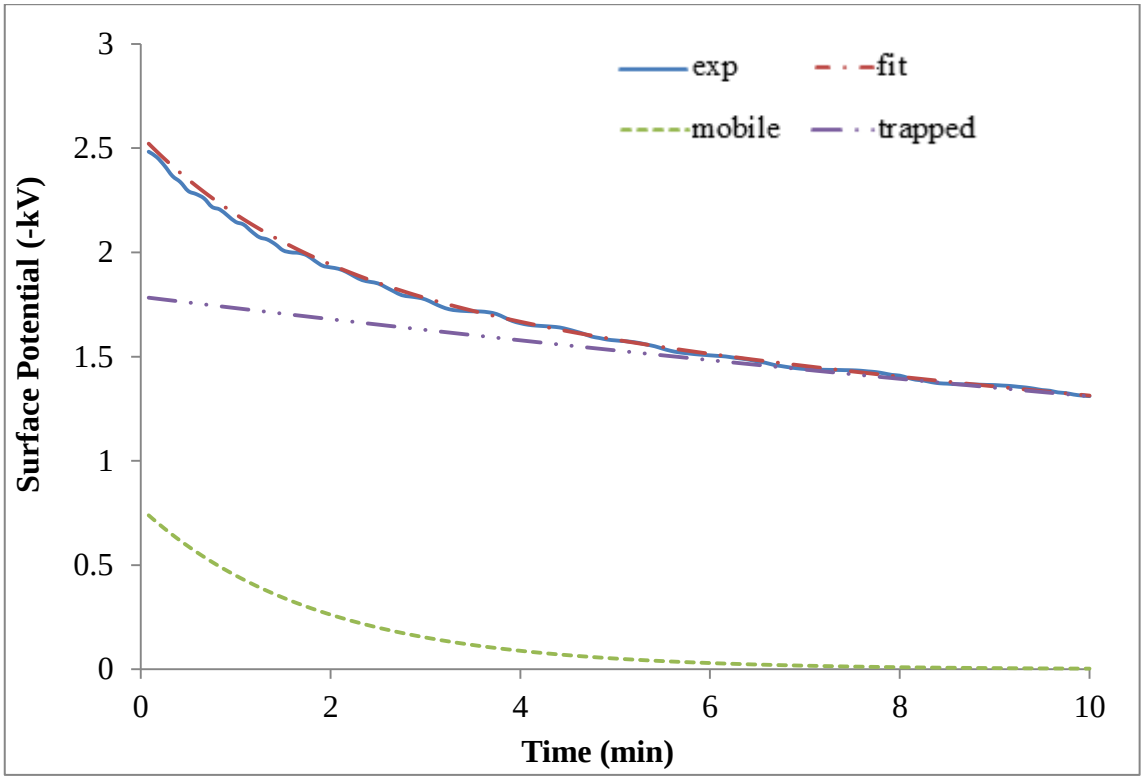


Figure 6-2b Mathematical results for – 4 kV.

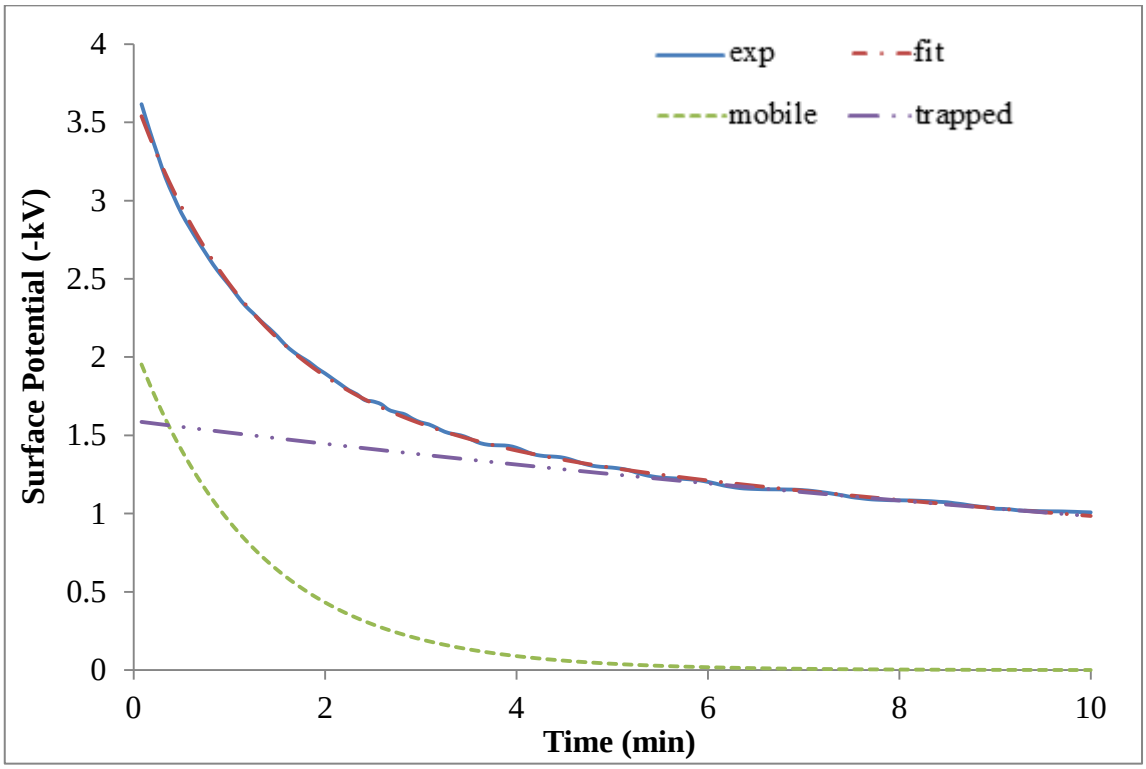


Figure 6-2c Mathematical results for – 6 kV.

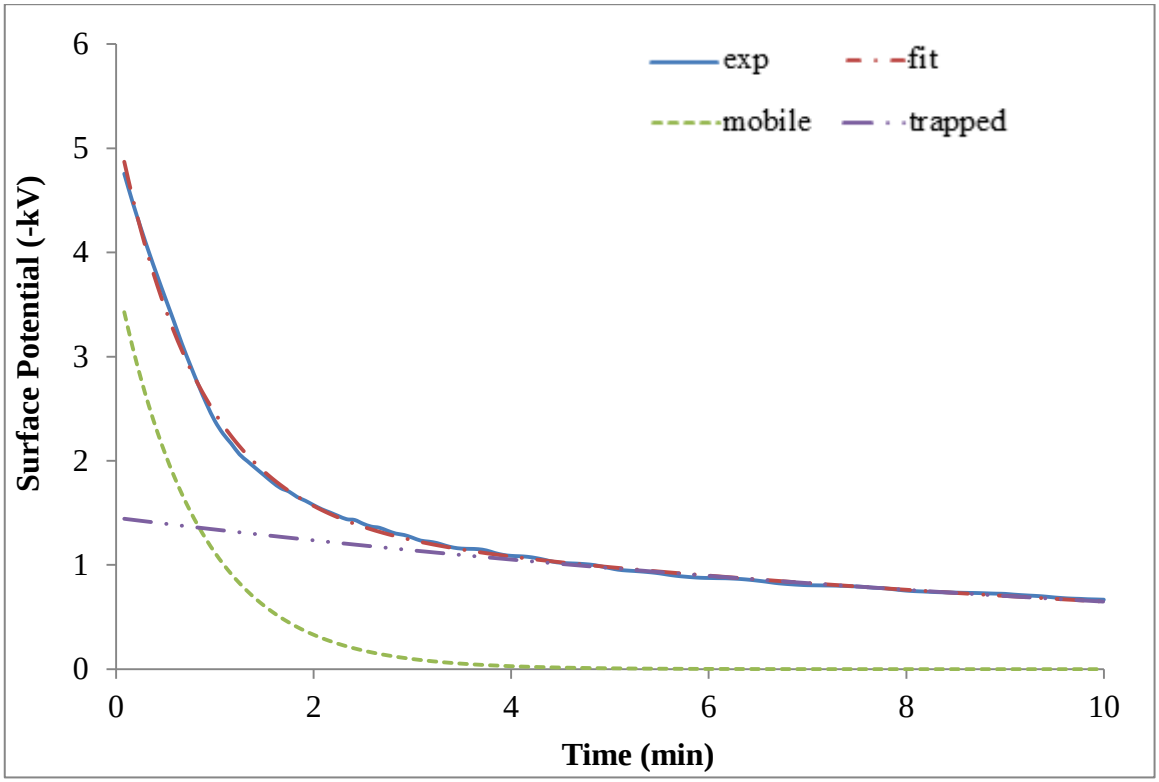


Figure 6-2d Mathematical results for – 8 kV.

Table 6-1 Parameters for equation (21)

| | – 2kV | – 4kV | – 6kV | – 8kV |
|---|---|---|---|---|
| $A_m$ | 0.3037 | 0.7228 | 2.0854 | 3.7933 |
| $B_m$ | 0.1213 | 0.54 | 0.7862 | 1.2202 |
| $A_t$ | 0.8893 | 1.7874 | 1.5923 | 1.4533 |
| $B_t$ | 0.0076 | 0.0311 | 0.0481 | 0.0807 |
| $A_m/A_{total}$ | 25.46% | 28.79% | 56.7% | 72.3% |

Figure 6-2 clearly shows that equation (21) is a good fit to the experimental results and it also represents the details of how mobile charge and trapped charge decay. It can be found that the constant of decay time *B* for both mobile charges and trapped charges are increasing with the corona charging voltage. For the initial potential *A*, the mobile charges keep increasing with the corona charging voltage; however, the trapped charges increase initially from – 2kV to – 4kV then start decreasing while corona charging voltage is increased further. To understand this phenomenon, the proportion of the mobile charges initial potential to the total initial potential was calculated and presented

in Table 6-1. It can be clearly seen that as the corona charging voltage increasing, $A_m/A_{total}$ increases, hence it can be concluded that the ratio of trapped charges against mobile charges is smaller while the corona charging voltage increases. These hypotheses that the cross-over phenomenon was dominated by the mobile charges, and the parameters for equation (21) are extremely helpful for the selection of parameters for bipolar charge transport model.

## 6.2 Simulation Results

Most of the models developed elsewhere have been using the hopping mechanism to describe the mobility of the charges [87]. However, based on the observation of charge packet in polyethylene, the mobility of the carriers has a more complex behaviour [81]. Therefore in this model, the mobility was kept constant for simulation at a particular corona charging voltage, but changed when a different corona charging voltage was applied. It had been noticed that for the current situation, the model cannot fit all the experimental results with unique parameters. The physical reason behind this is the charge injection from the top surface of the LDPE sample has more than one step. An electron avalanche in a negative corona is initiated by an exogenous ionisation event in a region of high potential gradient. The electric field accelerates these electrons so that they gain sufficient kinetic energy to cause ionisation when they collide with neutral gas molecules in their path. The electrons travel away from the negative electrode while the positive ions are drawn towards it. Therefore, electrons and several negative ions such as $O^-$, $O_2^-$, $O_3^-$, $HO^-$, $NO_2^-$, $NO_3^-$, $CO_3^-$ and $CO_4^-$ spread at the LDPE sample surface [88]. The electrons can easily inject into the bulk of the sample, but the negative ions will need to transformed into electrons then inject into the material. Therefore, to make the simulation results more manageable and simple, only the Schottky injection barrier height in the model is changed to fit the experimental results

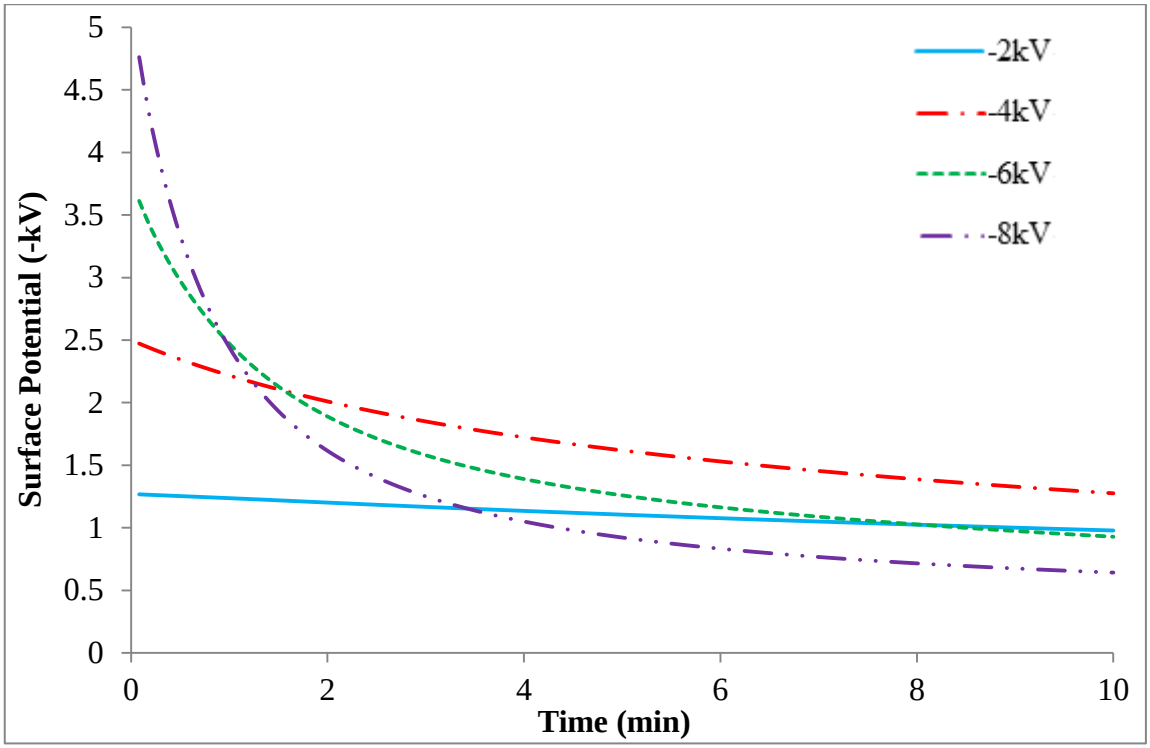

Figure 6-3 Simulation results

The simulation results obtained by adjusting the injection barrier height are shown in Figure 6-3. The simulation parameters for the model are given in Table 6-2. To compare these simulation results with the experimental results, coefficient of determination (known as R-squared) was also calculated. The R-squared for all these simulation results is higher than 95%, which represents a good fit of the data. The magnitude of the mobility was taken from Reference [81] and the value of electric field by selected the mobility was calculated using the initial surface potential divided by the sample thickness. Trap coefficient was kept at $1e^{-3}$ $s^{-1}$, and the recombination coefficients were $4e^{-3}$ $m^3C^{-1}s^{-1}$ for $S_0$, $S_1$ and $S_2$, 0 for $S_3$. It can be seen that the Schottky injection barrier height is decreasing while increasing the corona charging voltage. This represents that the magnitude of the injection changes more dramatically than the Schottky injection law with the electric field. There is no research on the exchange rate from negative ions to electrons. However, it can be hypothesis that this physical phenomenon also creates a large amount of charge injection and therefore affects the surface potential decay results.

The simulation results clearly show the surface potential decay features observed experimentally, and the detailed match may require further understanding on the exact injection and conduction mechanisms together with determination of material parameters. However, based on the proposed model and its numerical simulation charge

dynamics in the material can be revealed. Figure 6-4 illustrates the charge density, electric field, trapped and mobile charges distribution at different times within the bulk of the sample during decay process at both – 2 kV and – 8 kV with 2 min charging. It can be seen that the injected charges dominate the regions adjacent to the injected surfaces initially. They move fast towards the opposite surfaces. The reduction of charges takes two routes, i.e. (i) recombination with opposite charges and (ii) leaking away through the electrode/charged surface. The electric field distribution in the material is not uniform, showing the higher in the region close to the bottom surface. The overall electric field decreases with time, reflecting the reduction of charges in the bulk. It can be clearly seen that the initial electric field for – 8 kV is much higher than – 2 kV; however, the electric field decays much quicker for – 8 kV and ended with a lower electric field after 20 min decay. This may correspond to the cross-over phenomenon observed in the experimental results. The charge movement within the bulk can be also observed from the graphs. At the beginning of the decay process, both – 2 kV and – 8 kV show that the majority of mobile charges accumulated close to the surface; however, with the decaying time increases, the charges start moving to the opposite side and reach the bottom/top surface. They overwhelmingly dominate charge distribution. The distribution for electrons and holes is not symmetrical due to different injection barrier height assigned for two surfaces. On the other hand, the trapped charges are much smaller as the trap coefficient is relatively small. This is more obviously for the – 8 kV results. It can be seen that the trapped charges are getting larger with the time increasing. This is because that no de-trapping terms were used in the model, and the only way to reduce the trapped charges is recombined with mobile charges. Charges on the two surfaces are not included in these Figures. They changed with time as well and affected charge dynamics in the bulk.

Table 6-2 Simulation parameters

| | -2kV | -4kV | -6kV | -8kV |
|---|---|---|---|---|
| Electron injection | 1.165 | 1.16 | 1.14 | 1.14 |
| Hole injection | 1.155 | 1.15 | 1.13 | 1.13 |
| Electron/Hole Mobility | 10e-15 | 9e-15 | 7e-15 | 6e-15 |
| R-squared | 0.9723 | 0.9548 | 0.9754 | 0.9635 |

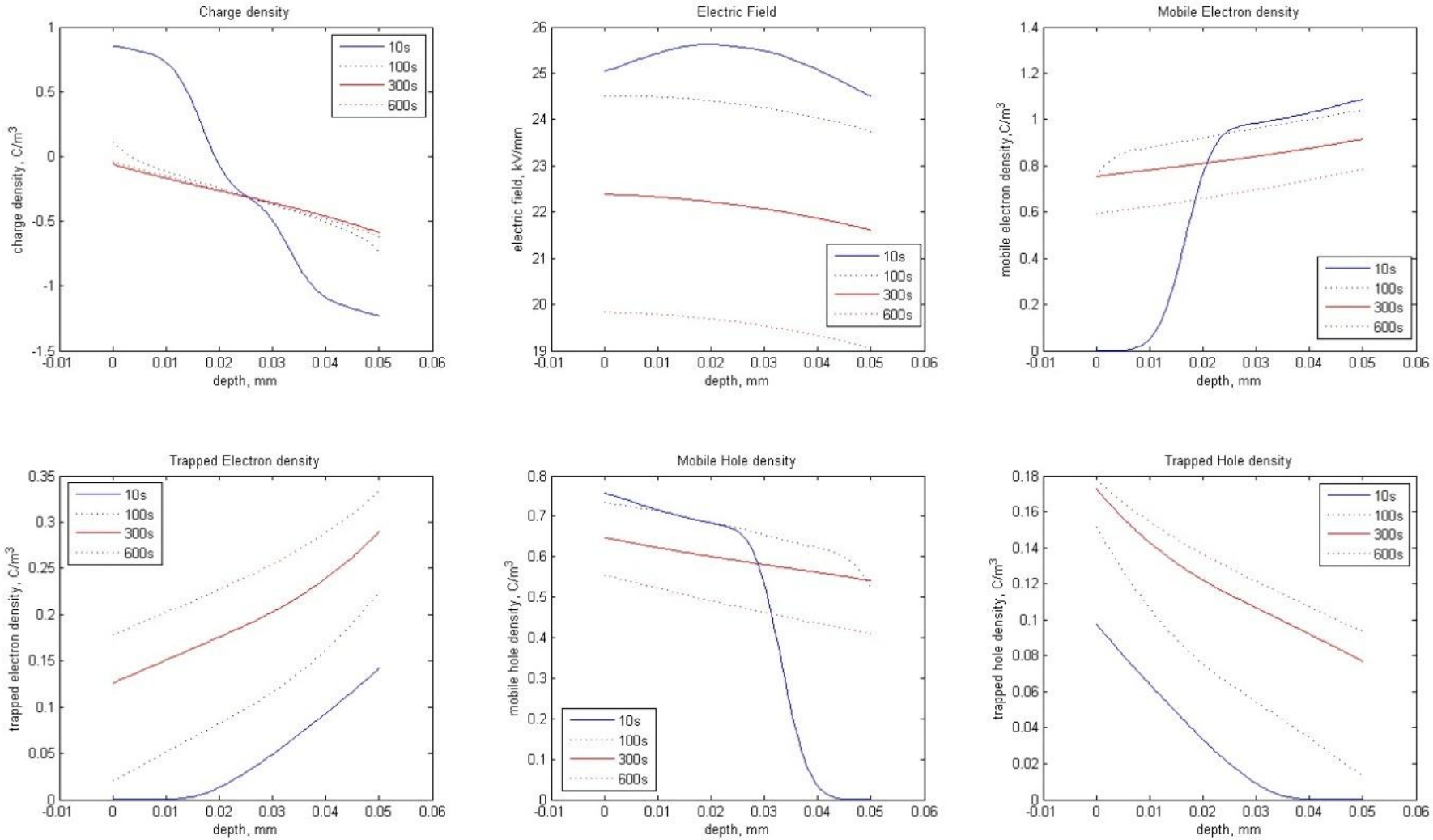


Figure 6-4a Charge and electric field distribution of corona charged LDPE film during surface potential decay process at – 2 kV.

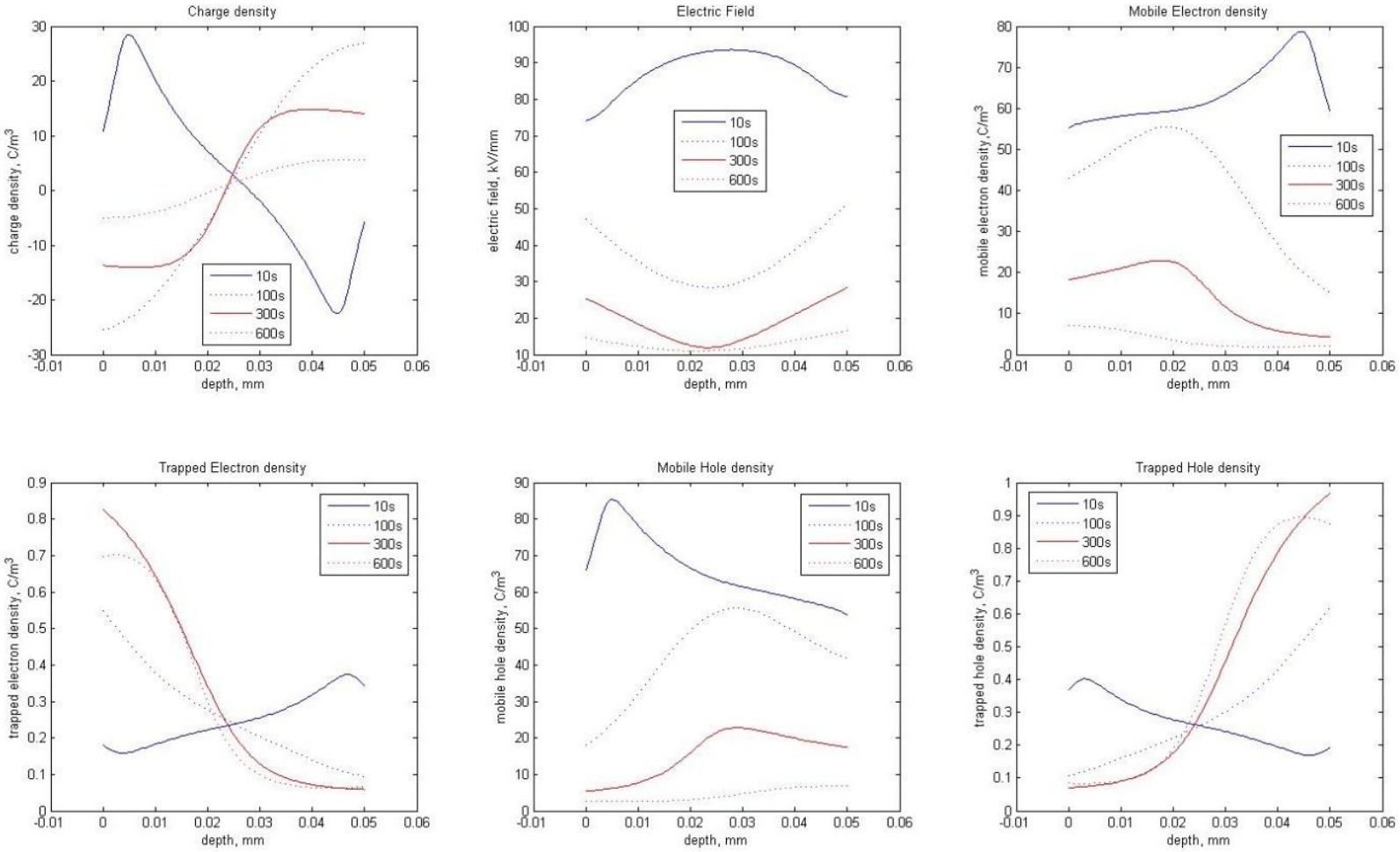


Figure 6-4b Charge and electric field distribution of corona charged LDPE film during surface potential decay process at – 8 kV.

## 6.3 Conclusions

From the previous sets of experimental data, a numerical simulation of surface potential decay has been carried out based on the bipolar charge transport model. Simulation results clearly demonstrate that the model has successfully revealed the surface potential crossover observed during decay process and a good fit of the experimental results can be achieved by adjusting the parameters. Further improvement on model parameters can be carried out especially the top surface charge injection equation. More importantly, information about charge transport, trapping and recombination of the material can be extracted via numerical modelling, which cannot be measured from the experiments. This information is critical if one wants to select materials for right applications.

# Chapter 7 Surface Potential Decay of Nano-polyimide Material Test

## 7.1 Introduction

Nanometer is a unit of length, which is defined as $10^{-9}$ meter. Nanotechnology focuses on studying the properties and applications of materials that have a structure size between 1 and 100 nm [89]. The research of nano material began with areas in ceramics and metal powder. Nowadays, more and more researchers start to look into the nano technology. The interfacial characteristics between nano particles and base polymer materials play an important role in determining the electrical properties due to the presence of such large surface area [90, 91]. Moreover, the changes in morphology due to the large surface area might also affect the trap depth and its density as well. Since the nano size particles have extremely large surface area, it is expected that even polymer materials loaded with a relative small amount of nano fillers lead to a strong effect on dielectric properties of the resultant composites [92, 93]. Consequently, polymer nanocomposites could have unique properties compared with ordinary polymer

composites. Polymer nanocomposites have attracted wide interest as a method of enhancing polymer properties and extending their applications. Polyimide (PI) as an engineering material has received more attention due to high thermal and chemical stability, good mechanical properties and excellent insulating properties in a wide range of temperatures [94]. There has been a lot of work over last few years on optical, thermal and mechanical properties of polyimide nanocomposites. However, little attention has been given to the effect of nano-fillers on charge transport and trapping in polyimide nanocomposites. In this chapter, surface potential decay method is used as a tool to monitor charge transport and trapping characteristics of insulating materials.

All the samples were supplied by University of Science and Technology Beijing. The $TiO_2$ with an average diameter of about 50nm was chosen as functional fillers because of its excellent corona resistance. In this experiment, the surface potential decay after dc corona charging of polyimide nano-$TiO_2$ has been studied. The PI/ $TiO_2$ nanohybrid films were prepared by using in-situ dispersive polymerization process. Prior to use, the surface of nano-$TiO_2$ was treated with y-aminopropyltriethoxy silane (KH550) as a coupling agent in order to disperse the $TiO_2$ nano-particles into the PI matrix homogeneously during the in-situ polymerization process [95]. The surface potential decay characteristics of pure PI film and PI/ $TiO_2$ nanohybrid films were investigated over the different corona charged times and charging voltages. To understand the influence of nano $TiO_2$ particle on the charge decay processes, samples with a different amount of nano-fillers were used in the research.

## 7.2 Experimental Results

### *7.2.1 Tests on high percentage nano-PI*

The first set of experiments was carried out on pure PI with three different nano-PI (5%, 10% and 15%). The environment condition was controlled at 21 $^{\circ}$C room temperature and 45% relative respectively, and the samples thickness is about 70 μm. The results of different initial voltages (− 2 kV, − 4 kV and − 7 kV) with a fixed charging time (4 min) are shown for all the samples with a decay period of 30min. Figure 7-1 shows the

experiment results for pure PI film and Figure 7-2, Figure 7-3 and Figure 7-4 show results for 5%, 10% and 15% respectively. It can be seen that all the results clearly show that the surface potential decay rates depend on the initial voltage. The results for 15% are not actually stable at the tail because the static monitor is set to measure high voltage range, and it cannot detect low surface potential accurately. It can be also seen that all the experimental results have the same trend that the higher initial voltage leads a faster decay. As PI is an excellent insulator, no cross-over phenomenon was observed except in the 10% results. The experiments on 20% and 25% were also attempted, but the results cannot be shown as the surface potential decays extremely fast to zero in any condition, which means that these samples are not able to store any charges, and they can easily move across the sample. In Figures 7-5 and 7-6, the results for all different samples under same experiment conditions were compared at both lower and higher field.

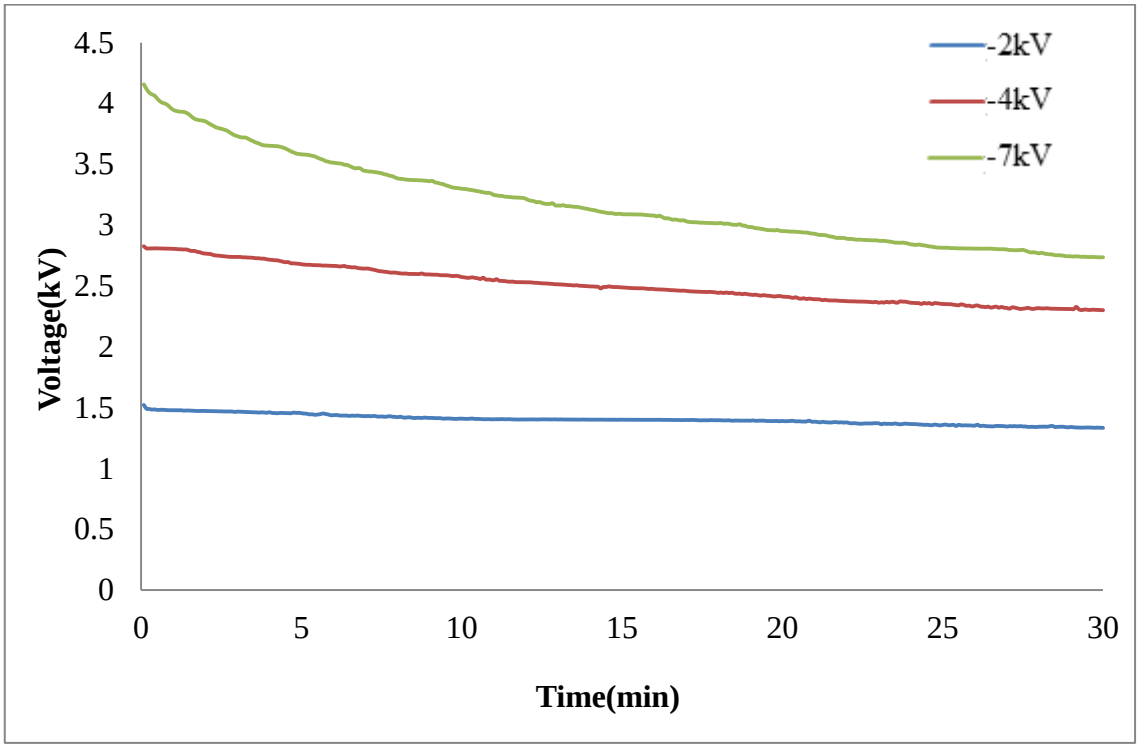


Figure 7-1 Surface potential decay of pure PI after corona charged under different grid voltages for 4 minutes

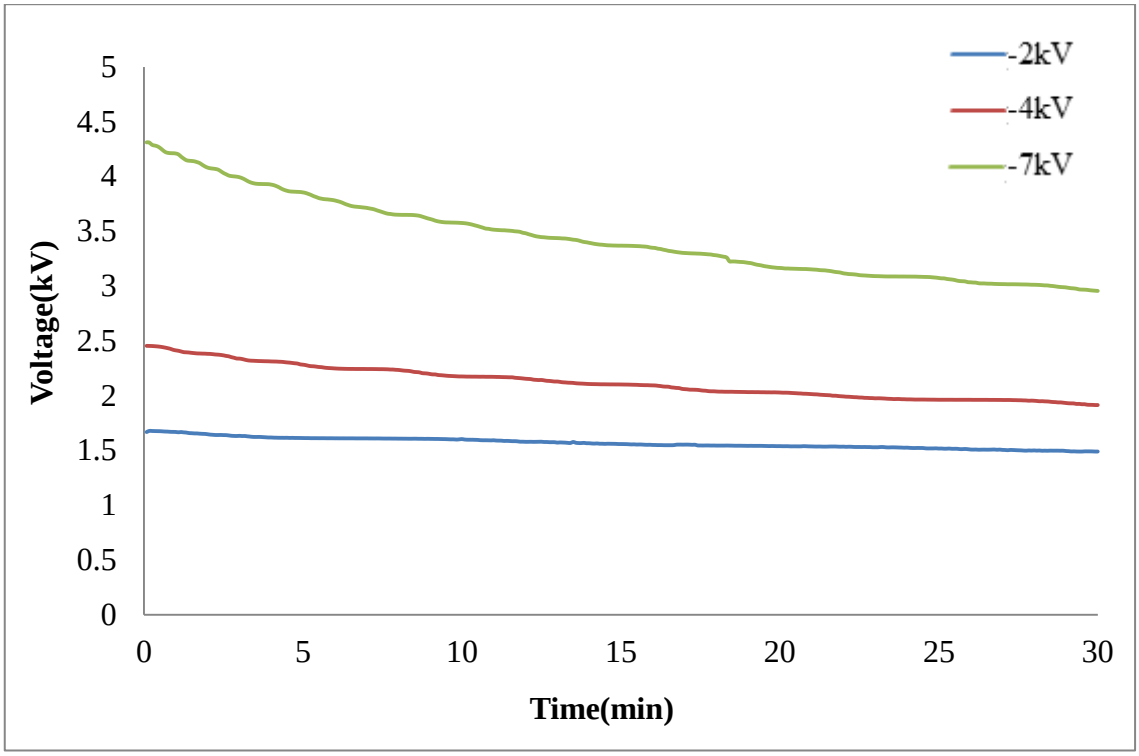


Figure 7-2 Surface potential decay of 5% nano PI after corona charged under different grid voltages for 4 minutes

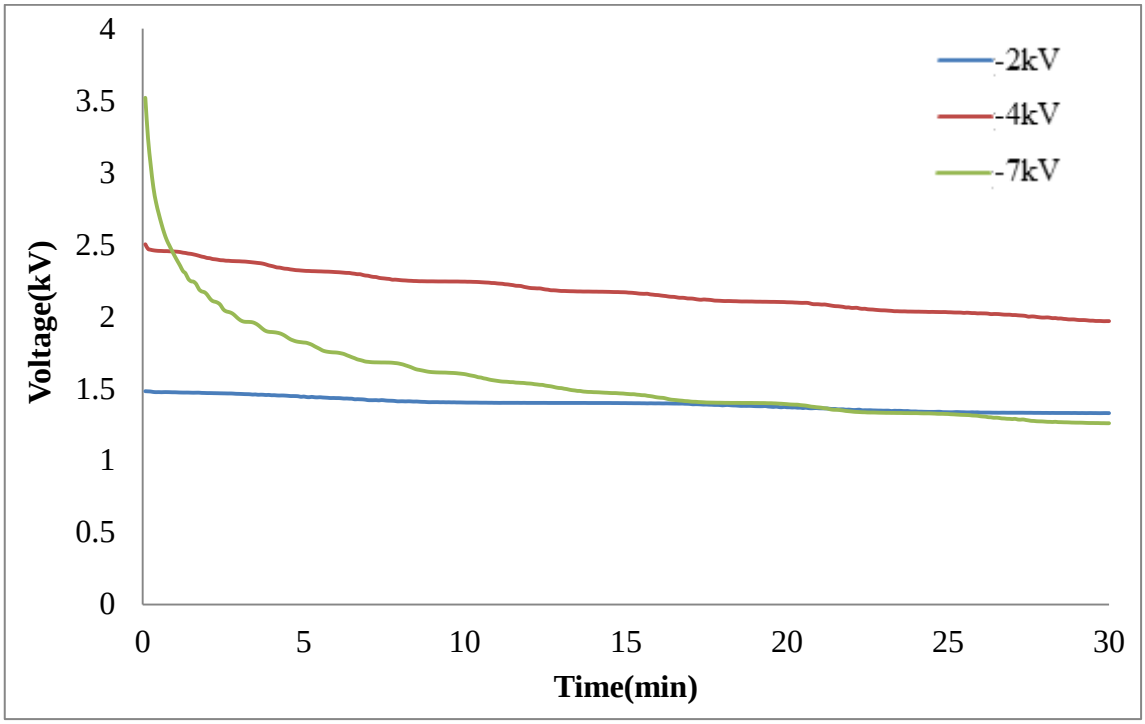


Figure 7-3 Surface potential decay of 10% nano PI after corona charged under different grid voltages for 4 minutes

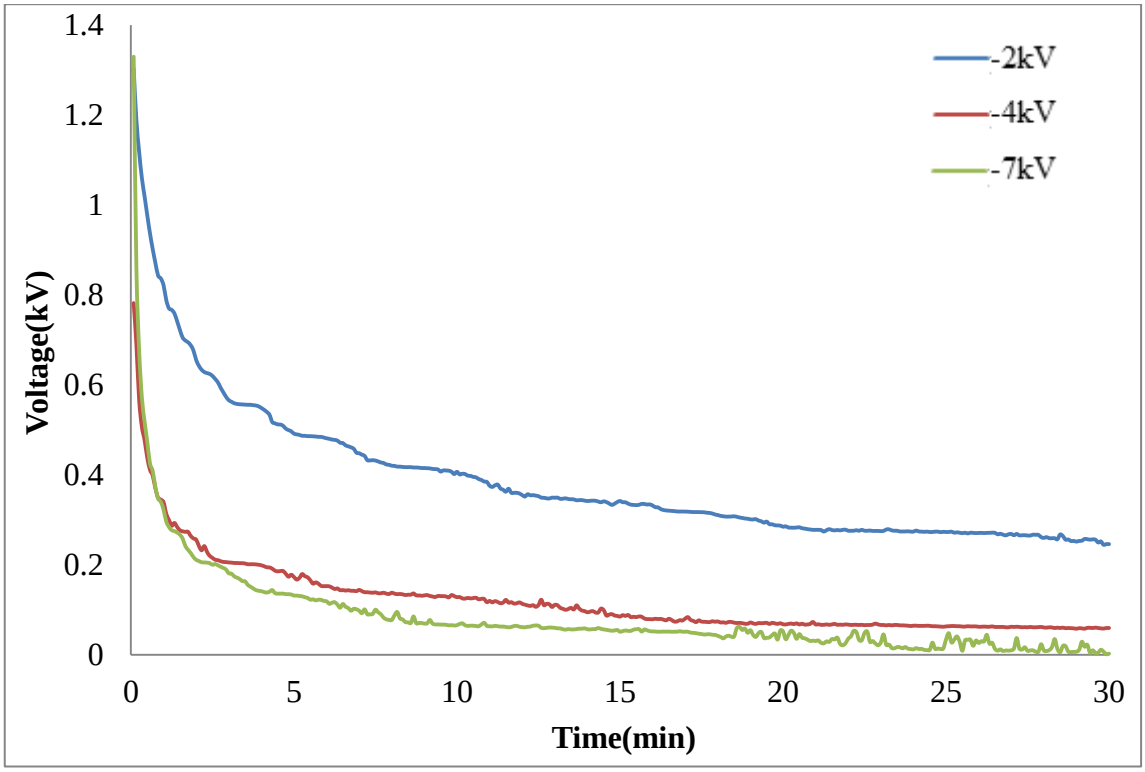


Figure 7-4 Surface potential decay of 15% nano PI after corona charged under different grid voltages for 4 minutes

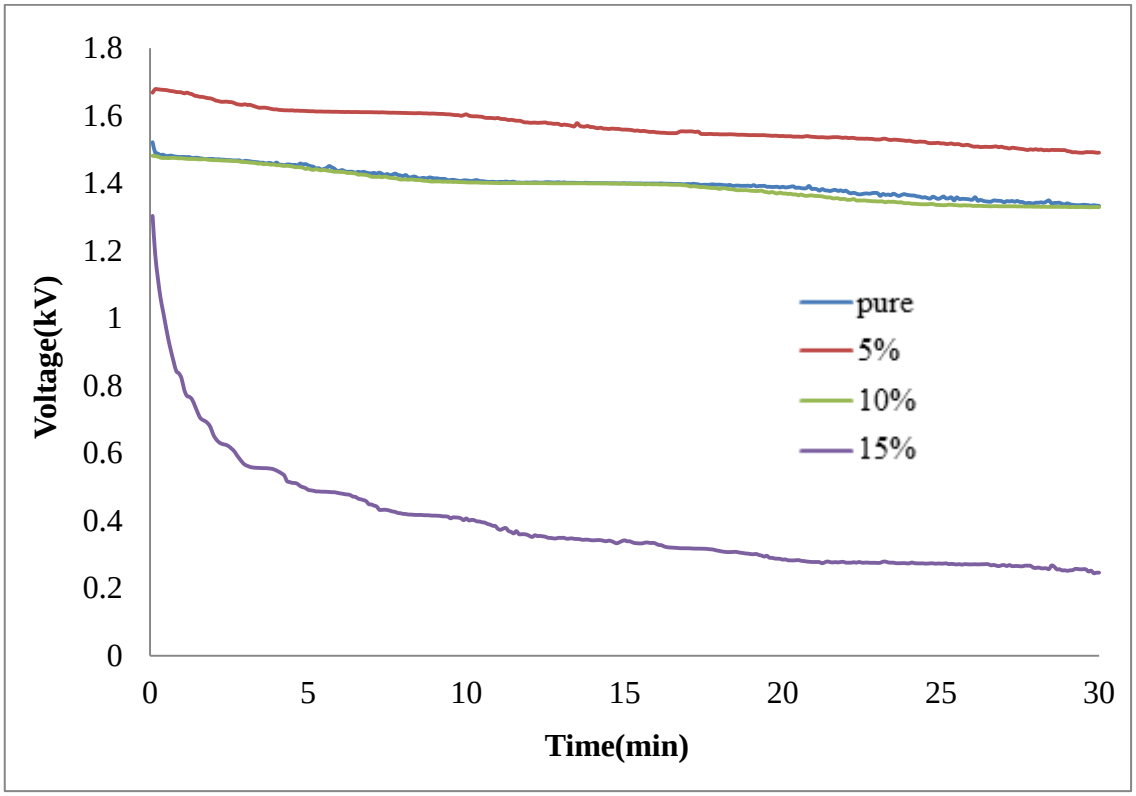


Figure 7-5 Comparison surface potential decay of all the samples after corona charged under a grid voltage of -2kV for 4 minutes

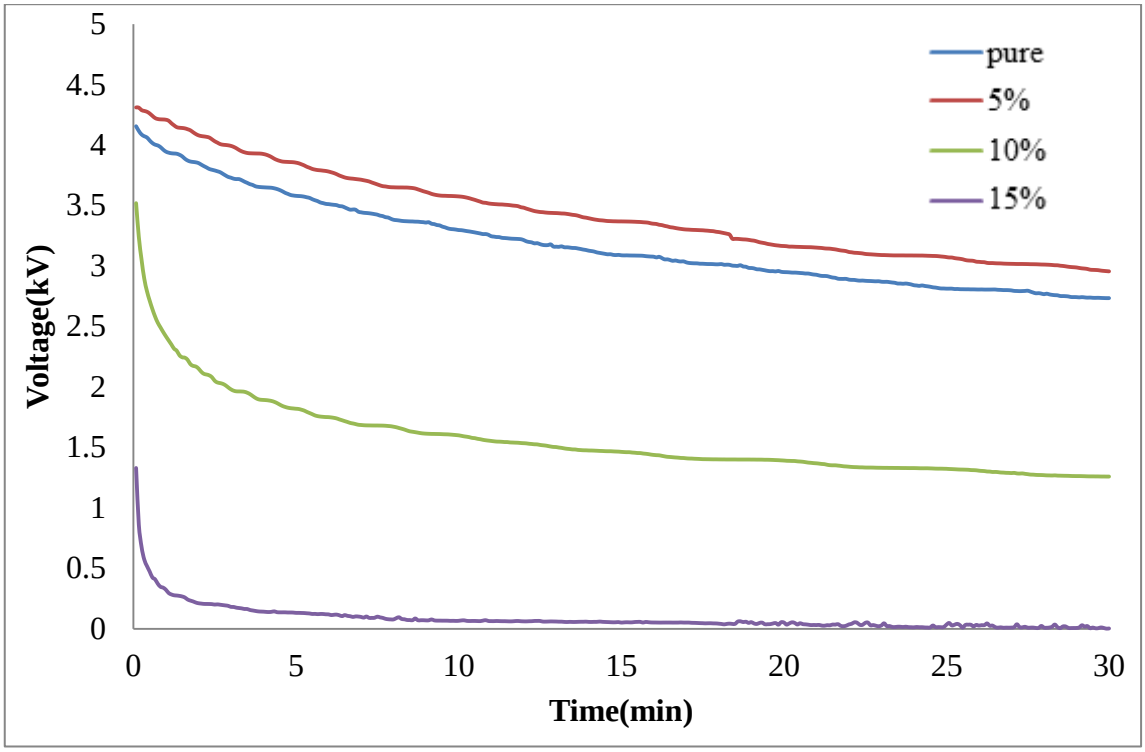


Figure 7-6 Comparison surface potential decay of all the samples after corona charged under a grid voltage of -7kV for 4 minutes

It can be seen that at a lower electric field (about 29kV/mm), the decay rates of pure-PI, 5% and 10% are similar to each other. However, the decay rate of 10% changes a lot under high electric field (100kV/mm). 15% sample's initial potential decay rate is a bit lower than 20% and 25% sample's; however, the total decay rate is large by comparing the 5% with the 10% samples and its surface potential ends close to zero. Surprisingly, 5% has the same trend with pure-PI as shown in Figure 7-5 and Figure 7-6, but due to the difference of the initial voltage, it is hardly to say which one has better insulation property.

### *7.2.2 Tests on low percentage nano-PI*

It was mentioned in the above section that adding nano-particles into PI can change its insulation property. However, if there is too much nano-composite inside the PI, the insulation property is decreased. Therefore, in this section, the pure PI with four different filler loading of PI (1%, 3%, 5% and 7%) will be examined by both surface

potential decay and DC conductivity measurements. A schematic diagram for DC conductivity equipment is shown in Figure 7-7. Both sides of the sample are gold coated and the electrodes are 20 mm diameter.

As there is no significant surface potential decay can be observed from the low field test, Figure 7-8 gives the results for all the samples on − 8 kV grid potential with three minutes charging. From the results, it can be seen that the nano-composite materials have a higher initial voltage compared with pure PI. It is highly clear that for these nano dielectrics, 3% has the best insulation property, 1% is slightly better than 5%, 7% is the worst. The pure PI cannot be directly compared with others because of significant difference in the initial surface potential. It is possible that breakdown strength of pure PI is much higher (about 210 MV/m) than the nano dielectrics (180 kV/mm for 5%) for a very short charging period (few minutes) [96]. Therefore, fewer charges are injected into the pure PI and results in a lower initial potential. The DC conductivity test was done in an oven, with a 20 mm diameter gold electrodes on both sides. As the temperature has a significant influence on the conduction current, the testing temperature was fixed at $30^{o}$C to avoid the influence of small temperature fluctuation in the room on the measured current. Figure 7-9 shows the conduction current for all the samples under 6.5 kV for a period of 1 hour. It can be clearly seen that the results show extremely good agreement with the surface potential decay results. The pure PI sample can be also examined. The insulation property of pure PI is only better than the 7% in this case.

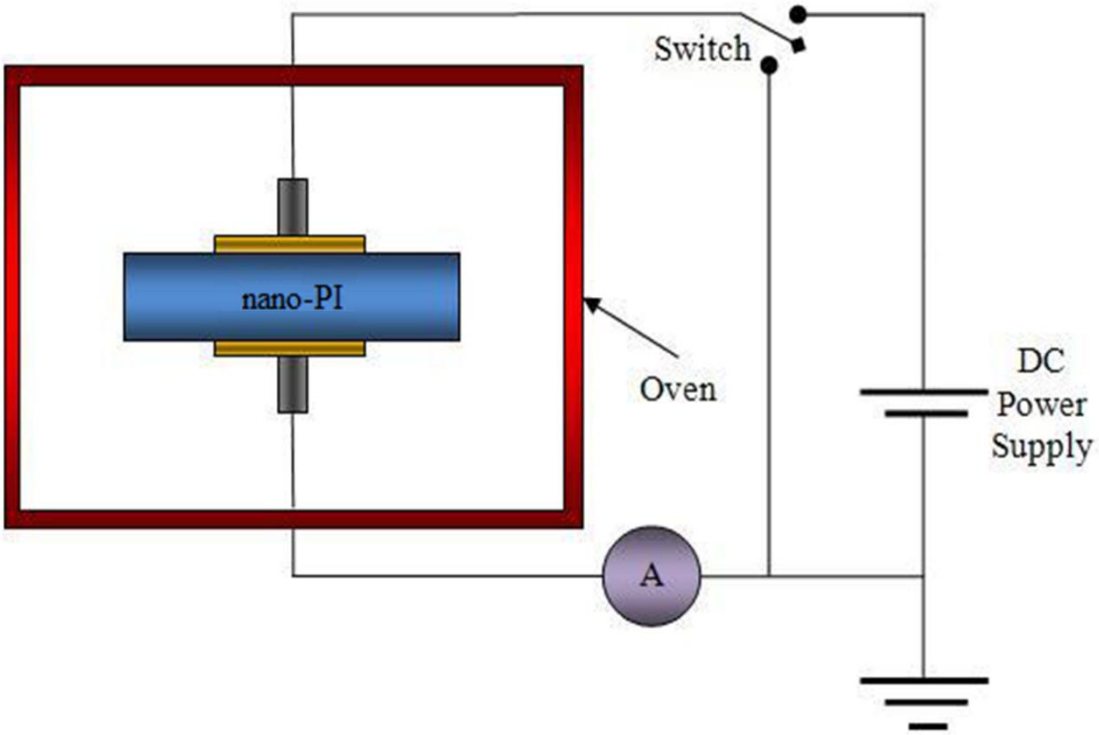


Figure 7-7 DC conductivity measurement equipment

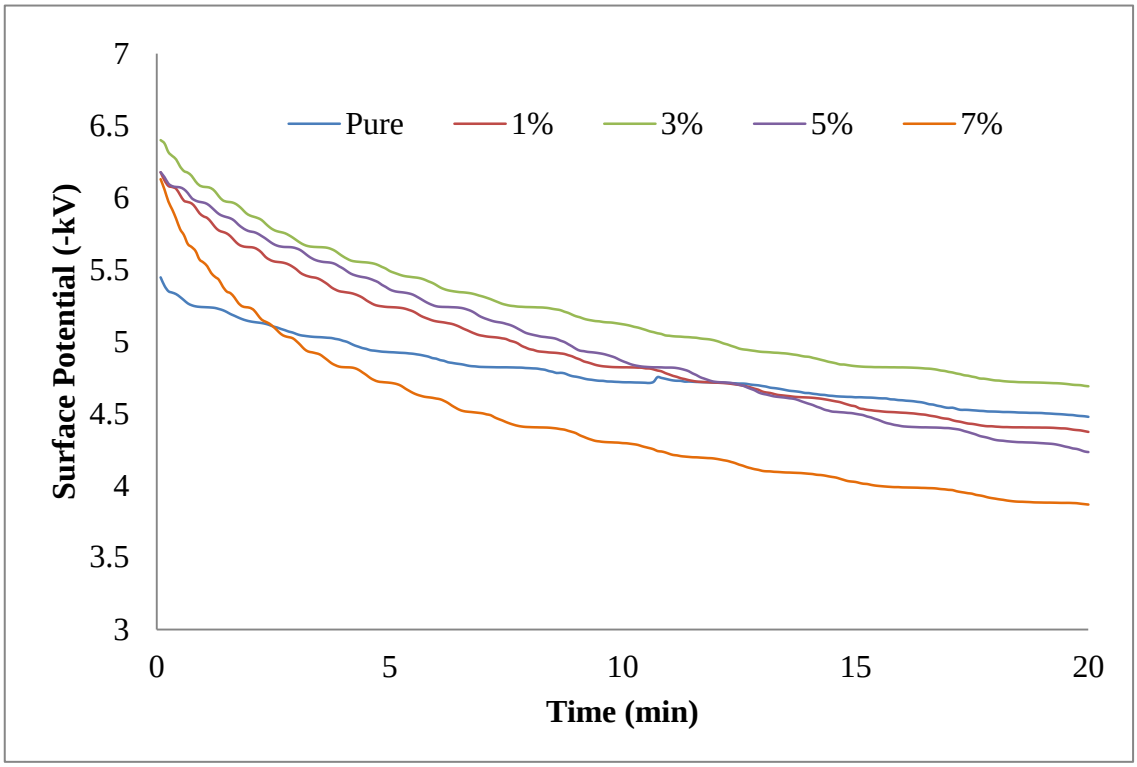


Figure 7-8 Surface potential decay at -8kV grid potential with 3min charging for low percentage nano-PI

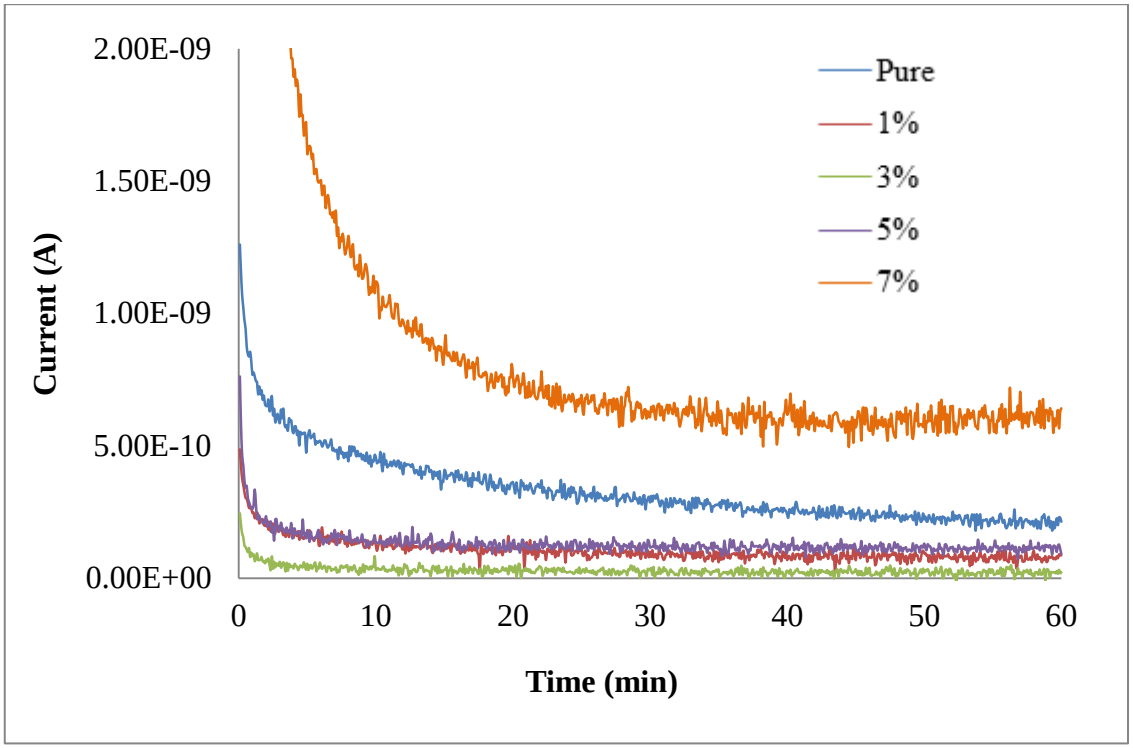


Figure 7-9 Currents at 6.5kV for 1 hour for low percentage nano-PI

From the results above, it can be concluded that adding nano-particles into dielectrics can improve its electrical properties. However, different amount of nano-fillers will give different results. As 1% and 3% samples reduce the conductivity to the lowest point, it has been known that a small amount of nano-fillers is separated inside the dielectric with a certain wide distance. These nano fillers become 'extra traps' for the dielectric, hence they can improve the insulation property. However, if more nano-particles are added into the dielectrics, a better insulation property can still be achieved, but its conductivity is increased (for example 5% sample). If the amounts of nano-particles are increased further, the opposite effect is achieved, and the dielectric's insulation property will get worse. From this section, it can be said that surface potential decay measurement can be used to compare unknown nano dielectrics insulation properties. The advantage for surface potential decay measurement is that it takes less time to examine one sample; also it can test a bigger sample than the dc conductivity measurement. However, the testing environment has to be carefully controlled, and if the initial potential had a big difference, the comparison cannot be made.

## 7.3 Discussion

A similar experiment had been done on measuring electric conductivities for pure LLDPE sample and LLDPE with 1%, 5% and 10% nano-alumina [97]. For an idealized situation where all the nano spherical shaped particles were assumed to sit on the eight corners of a cube (shown as Figure 7-10), it is possible to calculate the separation distance between adjacent particles using equation [97]:

$$d = r\left\{\left[\frac{4\pi}{3}\left(1+\frac{1-F}{F}\frac{\rho_t}{\rho_m}\right)\right]^{\frac{1}{3}}-2\right\} \tag{22}$$

where F is the weight fraction of nano $TiO_2$ particles, $\rho_t = 4000\ kg/m^3$ and $\rho_m = 1430\ kg/m^3$ are the density of $TiO_2$ and PI matrix respectively. Figure 7-11 shows the separation distance d versus $TiO_2$ fraction F in PI matrix for r=25nm. It can be seen that the separation distance varies rapidly for a small percentage of nano $TiO_2$ (5% or less), and it changes slowly for high percentages.

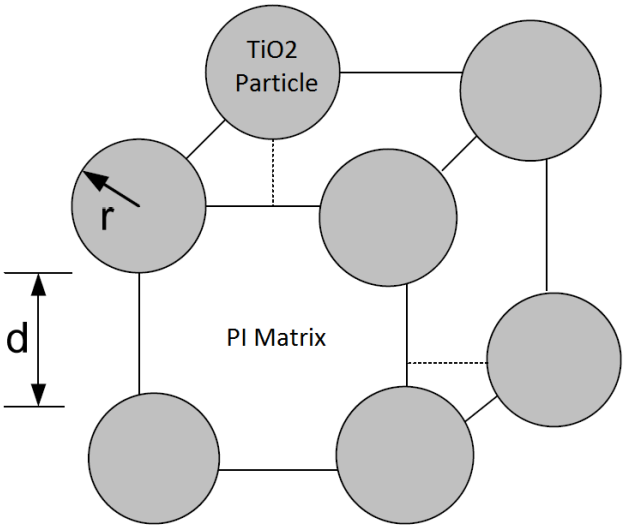


Figure 7-10 Cubic array of spherical nano $TiO_2$ particle of radius r and matrix spacing d.

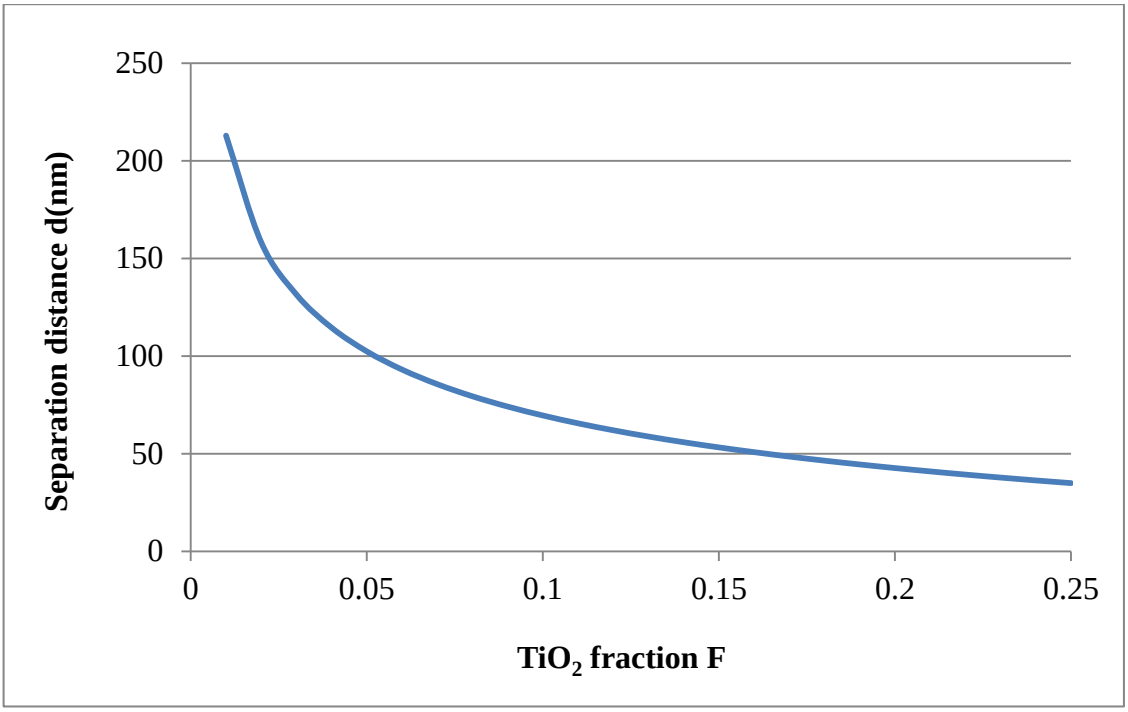


Figure 7-11 Separation distance between two adjacent nano $TiO_2$ particles with increasing volume fraction calculated from equation (22).

The behaviour of the nano materials can be explained by the behaviour of interaction zone around the nano-particle. In the 10% or more cases, the sample is then composed entirely of this interface region. In this region, the PI behaves differently from its normal response as in the absence of nano-$TiO_2$ fillers. It is believed that the confrontation of nano-$TiO_2$ particles and PI matrix with dissimilar structures introduces a transition or interaction zone through which the properties change from those of the filler particle to the bulk PI matrix. It is also possible that the interaction zone may behave completely differently. A schematic diagram is shown in Figure 7-12 to represent the interaction zone and overlap in the presence of a higher percentage of nano-$TiO_2$ particles. Based on the idealized model shown in Figure 7-10, the radius of the interaction zone can be estimated from the separation distance shown in Figure 7-11. As 7% nano-PI has higher conductivity for pure PI, we assume that the overlap of interaction zones become frequently. For 7%, the separation distance is around 85.66 nm, so the radius of the interaction zone is about 67.83 nm by calculation.

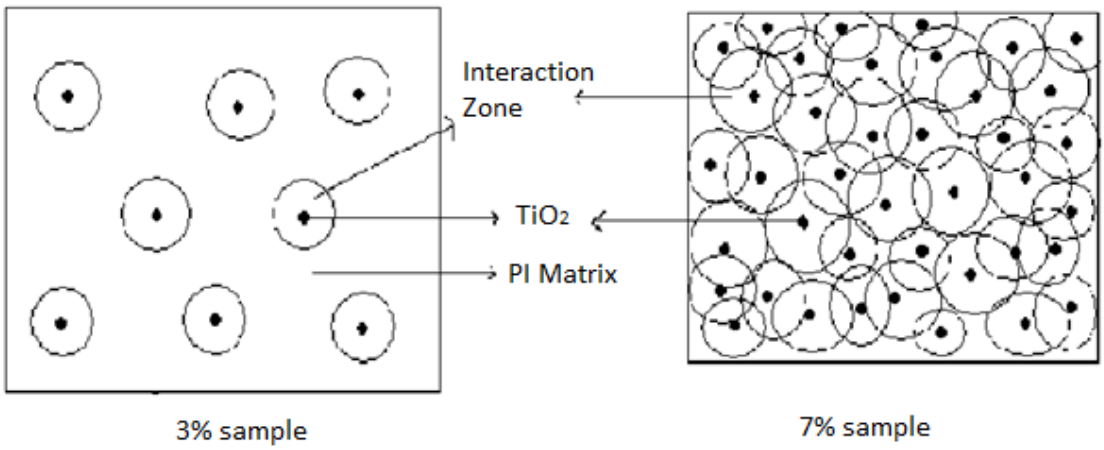


Figure 7-12 Schematic diagram of interaction zone around nano TiO2 particles.

Therefore, for 3% sample or less, the nano-composites can be seen as some additional traps in the sample, which results in a slower potential decay on the sample surface. For 5% sample, the nano-composites can still be able to trap some electrons, but there can be few overlap of interaction zones, as a result, its conductivity is slightly higher than the 3%, but still less than pure PI. For 7% sample or more, it can be known as there are too many overlaps between each interaction zones, which the electrons can easily across through the sample. Therefore result in an extremely fast decay for a high percentage nano-PI.

# Chapter 8 Modelling of Corona Charging Process

## 8.1 Introduction

Recently, most of the corona charging systems are using the needle-grid set-up (Figure 8-1) mainly for two reasons: firstly the surface potential of the dielectrics can be easily controlled by adjusting the magnitude of the grid electrode potential, and secondly the capability of this set-up to get a uniformly distributed charge density along the dielectric surface [50]. However, there are no work and available data on the potential differences and distance between the two electrodes such that a perfectly charged sample would be achieved. It had been found that there were no consistent data available to set up the grid position in relationship with both needle and sample. For example, in the literature available, the grid position was varied from 0.5 cm to 1.5 cm above the dielectric samples and the needle position was moved between 1 cm to 5 cm above the dielectrics [80, 98, 99]. The aim of this chapter is to build up a model to find out how the geometry of the corona charging system affects the surface charge density of the polymer. The model in this work was based on a gas discharge model [100-106]. It was built in 2D axial symmetry configurations using the finite element COMSOL Multiphysics package.

It had been proved that the negative corona discharge occurs in the vicinity of the cathode, therefore, due to the high electric field and charge densities, a very fine 'FEA mesh' need to be used around the needle head and along the axial symmetry line (Figure 8-2). In this chapter, the effect of adding the grid electrode to the corona charging system will be discussed by studying the impulse current formed and dielectrics surface charge density on the sample surface.

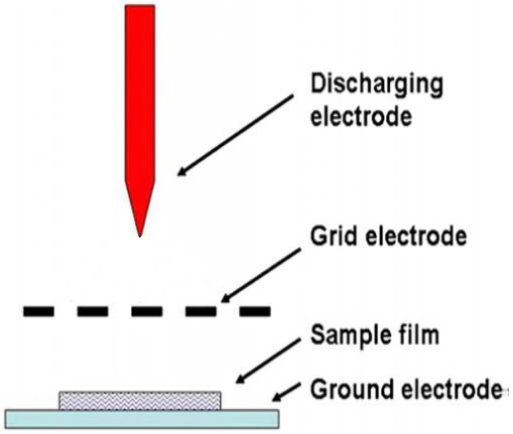


Figure 8-1 Needle-Grid electrodes corona charging system

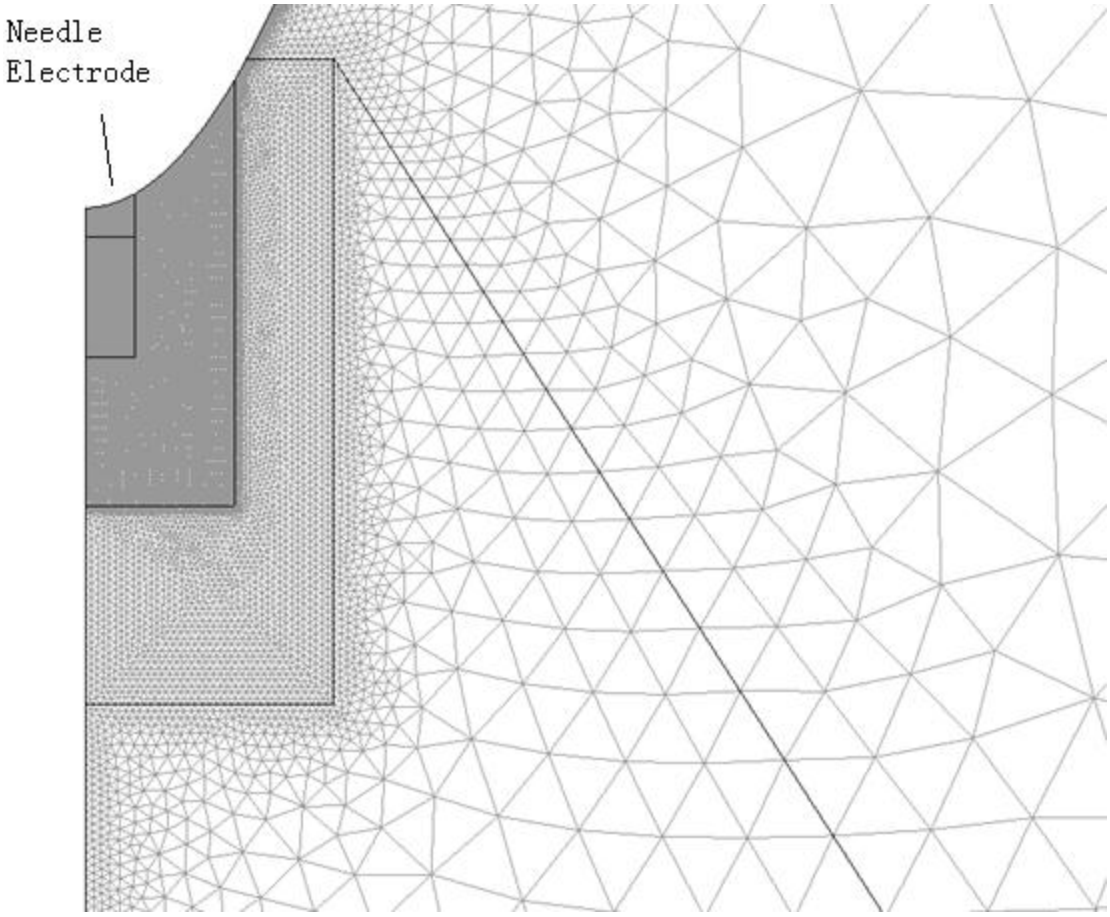


Figure 8-2 'FEA mesh' distribution in the model

## 8.2 Model Description

### *8.2.1 Geometry of the model*

From Figure 8-3, it can be observed that the needle in this model has curvature. The geometry of the needle was drawn with the help of equation (23). The radius of the curvature at the needle tip is 174 µm. In the model shown in Figure 8-4, the sample has a diameter of 28 mm, and it was considered to be a polyethylene film with 50 µm thickness. In the first instance, the grid electrode was modelled as several concentric circular conductors, which were varied at different radiuses from the axial symmetry line of the model. The grid electrode has a thickness of about 500 µm; however in our model, this dimension was reduced to zero to limit the size of the 'FEA mesh', therefore reducing the computer memory. The bottom surface of the polyethylene sample was grounded, and the needle electrode was fixed at 2 cm away from the ground. The grid electrode was set 0.5 cm or 1 cm away from the ground respectively. The model was solved using a transient solver within COMSOL. The electric potential of the needle and the grid electrode were initially set to 0 V. Within the first 0.1 ns of the simulation these potentials were brought to the working voltage levels -6500 V for the needle and -1000 V for the grid respectively. From 0.1 ns to 5 µs when the simulation was finished, the two voltage levels were kept constant

$$\left(\frac{z}{b}\right)^2 - \left(\frac{r}{a}\right)^2 = 1 \;;\; \frac{a^2}{b} = \textit{radius of curvature} \tag{23}$$

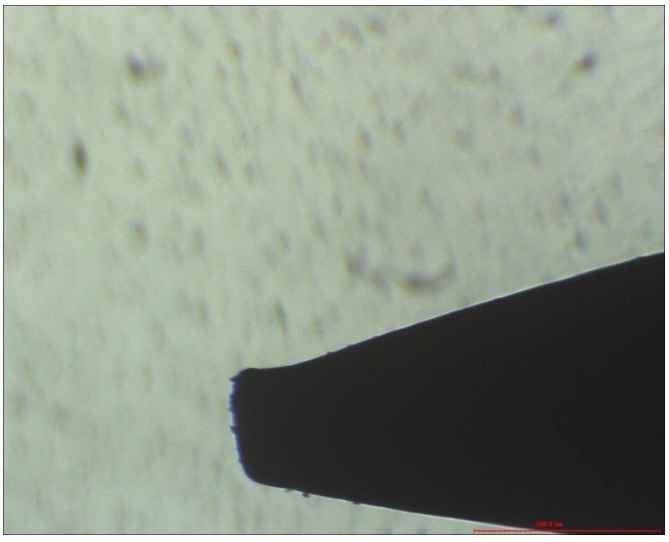

Figure 8-3 Picture of the needle

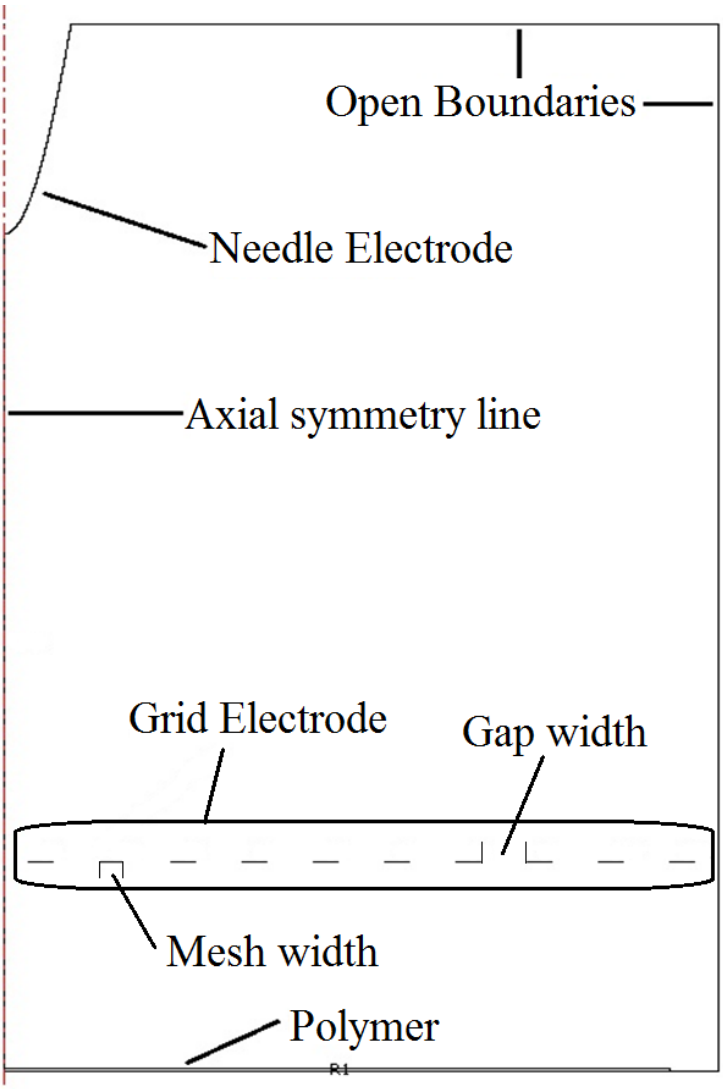


Figure 8-4 Corona charging system simulation geometry

### *8.2.2 Mathematical model*

A well-known hydrodynamic drift-diffusion model consists of a set of continuity equations coupled with Poisson's equation, given as:

$$\frac{\partial N_e}{\partial t} = N_e \alpha |W_e| - N_e \eta |W_e| - N_e N_p \beta_{ep} - \nabla \cdot (N_e W_e - D_e \nabla N_e) \tag{24}$$

$$\frac{\partial N_p}{\partial t} = N_e \alpha |W_e| - N_e N_p \beta_{ep} - N_n N_p \beta_{np} - \nabla \cdot (N_p W_p) \tag{25}$$

$$\frac{\partial N_e}{\partial t} = N_e \eta |W_e| - N_n N_p \beta_{np} - \nabla . (N_n W_n) \tag{26}$$

$$\nabla \cdot (\varepsilon_r \nabla V) + \frac{e}{\varepsilon_0} (N_p - N_e - N_n) = 0 \tag{27}$$

where $t$ is time, $e$ the electronic charge, $\varepsilon_0$ the dielectric constant of free space, $\varepsilon_r$ the relative permittivity and $V$ the electric potential; subscripts $e$, $p$, $n$ represent electrons, positive and negative ions respectively; $N_e$, $N_p$ and $N_n$ are the ion number density; $W_e$, $W_p$ and $W_n$ the electron, positive and negative ion drift velocities; $\alpha$, $\eta$, $\beta$ and $D$ the ionization, attachment, recombination and electron diffusion coefficients respectively. The simulation parameters in equations (24-27), which are functions of the local electric field, are given in Table 8-1.

The total current can be then computed using the energy conservation law:

$$I = \frac{1}{V_{needle}}\left(\frac{d}{dt}\int_V W dV + \int_V P_D \, dV\right) \tag{28}$$

where $W = \frac{1}{2}\varepsilon_0 \varepsilon_r E^2$ and $P_D = \mathbf{E} \times \sum eN_i \mathbf{W}_i$ .

The surface charge density can be calculated by integrating the normal component of charged particle current densities at the surface. In cylindrical coordinates, this can be expressed as

$$\sigma_s(t) = \int_0^t (J_{ez} + J_{nz} - J_{pz}) dt \tag{29}$$

where $J_{iz} = eW_{iz}N_i$ .

Table 8-1 Simulation parameters [100]

| Parameters | Functions (Electric field strength $E = \varepsilon_r \varepsilon_0 \nabla V$ in $V \cdot cm^{-1}$) |
|---|---|
| $\alpha (cm^{-1})$ | $3500 \exp\left(-1.65 \times 10^5 E^{-1}\right)$ |
| $\eta (cm^{-1})$ | $15 \exp(-2.5 \times 10^4 E^{-1})$ |
| $\beta_{ep} = \beta_{np} (cm^3 s^{-1})$ | $2 \times 10^{-7}$ |
| $W_e (cm\ s^{-1})$ | $-6060\ E^{0.75}$ |
| $W_p (cm\ s^{-1})$ | $2.7E$ |
| $W_n (cm\ s^{-1})$ | $-2.7E$ |
| $D\left(cm^2 s^{-1}\right)$ | 1800 |

### *8.2.3 Boundary and initial conditions*

The boundary conditions of all the models are shown in Table 8-2. At the needle electrode, the boundary condition for electrons is given as a secondary emission flux when positive ions strike the cathode

$$N_e\left|\mathbf{w}_e\right| = \gamma N_p\left|\mathbf{w}_p\right| \tag{30}$$

where $\gamma$ has been used in the range from $10^{-3}$ to $10^{-2}$, it is chosen as 0.01 in this model [100].

The initial conditions are given as

$$N_e = N_{\max} \times \exp\left(-\frac{(r-r_0)^2}{2s_0^2} - \frac{(z-z_0)^2}{2s_0^2}\right) \tag{31}$$

where $N_{max} = 10^{15}\mathrm{m}^{-3}$, $r_0 = 0\,\mu\mathrm{m}$, $z_0 = 2\mathrm{cm}$, $s_0 = 25\,\mu\mathrm{m}$; $N_p = N_n = 0m^{-3}$ [100].

Table 8-2 Boundary conditions for all the models

| Application mode | Convection and diffusion $N_e$ | Convection and diffusion $N_p$ | Convection and diffusion $N_n$ | Electrostatics $V$ |
|---|---|---|---|---|
| Axial symmetry line | Axial symmetry | Axial symmetry | Axial symmetry | Axial symmetry |
| Needle electrode | Flux | Convective flux | Concentration=0 | $V = -6500$ |
| Grid electrode | Convective flux | Convective flux | Concentration=0 | $V = -1000$ |
| Polymer upper surface | Convective flux | Insulation/Symmetry | Convective flux | Surface charge |
| Open boundaries | Convective flux | Convective flux | Convective flux | Zero charge/Symmetry |
| Outer ground boundary | Convective flux | Concentration=0 | Convective flux | *V=0* |

## 8.3 Simulation results

Five different models with or without the grid electrode were built as shown in Table 8-3. Every model was run for 5 μs and the impulse current and surface charge density was observed. In this section, a comparison of the obtained results is presented.

Table 8-3 Model description

| Model Number | Description |
|---|---|
| Model I | Needle Only |
| Model II | Grid electrode 5mm above the ground, mesh width is 5mm and gap width is 10mm. |
| Model III | Grid electrode 10mm above the ground, mesh width is 5mm and gap width is 10mm. |
| Model IV | Grid electrode 10mm above the ground, mesh width is 10mm and gap width is 10mm. |
| Model V | Grid electrode 10mm above the ground, mesh width is 10mm and gap width is 5mm. |

### *8.3.1 Effect of the grid electrode height*

In this section, the effect of the extra grid electrode with two different positions is compared with the model that has a needle electrode only. The results for models I, II and III are shown in Figures 8-5 and 8-6.

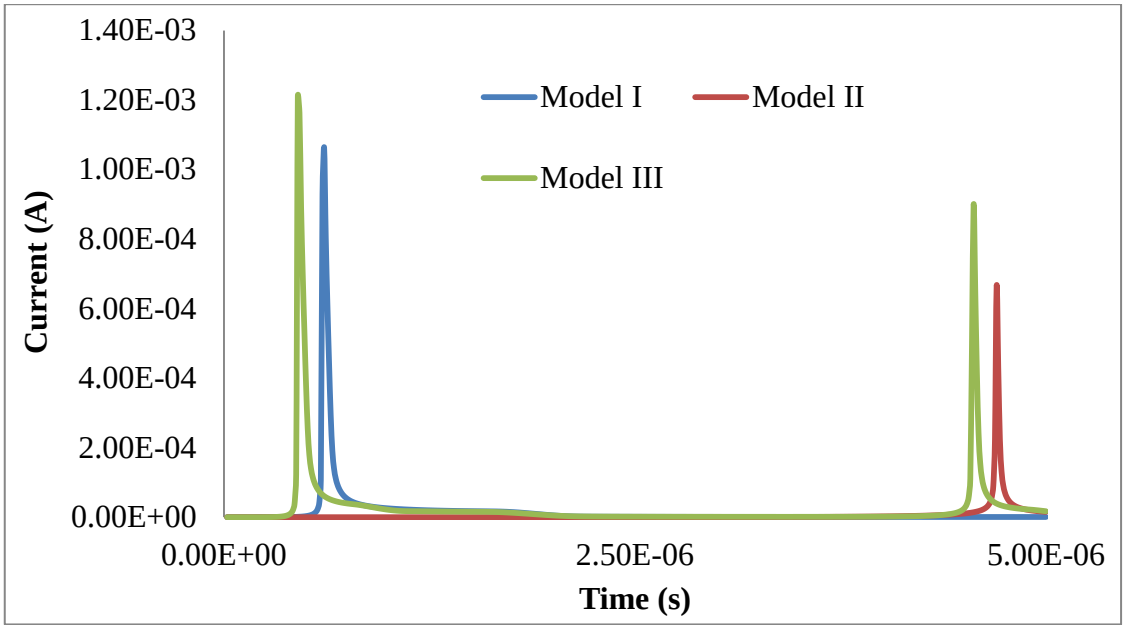


Figure 8-5 Current for models I, II and III

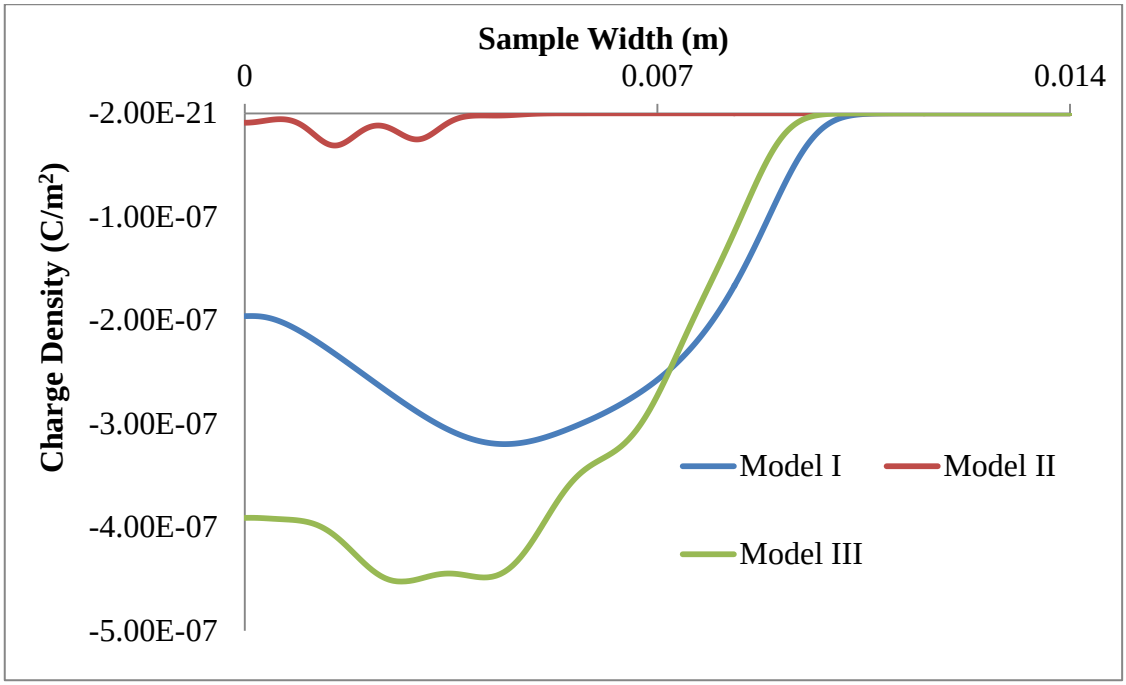


Figure 8-6 Surface charge densities for models I, II and III at 5 μs

From the graphs above, it can be seen that the initial impulse current for model I and III emerges at a similar time, but it appears extremely late in model II. Model III has two impulse current emerged within 5 μs. Large differences in surface charge densities were observed. It can be noticed that at the point where the impulse current appeared, a great amount of electrons are generated as shown in Figure 8-7. They will be pushed down to the sample surface, leading to an increase of surface charge density. As a result, model

III has the largest surface charge density because of one more impulse current compared to the other two. It has been reported in [96] that the higher needle electrical potential will cause larger initial impulse current amplitude and a higher frequency of the current pulse. In models II and III, the needle electrical potential is the same as in model I; however the impulse current is different. Therefore, the electric field underneath the cathode affects the behaviour of impulse current. From model I, it can be found that the electrical potential at 5 mm and 1 cm above the ground is about -600 V and -1200 V at the symmetry axis (Figure 8-8). The electrical potential at 5 mm above the ground is fixed to -1000 V in model II, therefore, reduces the electric field at the needle and leads to a smaller and slower first impulse current. In model III, the electrical potential is restricted to -1000 V at 1 cm above the ground, which leads to a higher electric field underneath the cathode and hence in this case a larger and faster first impulse current is observed.

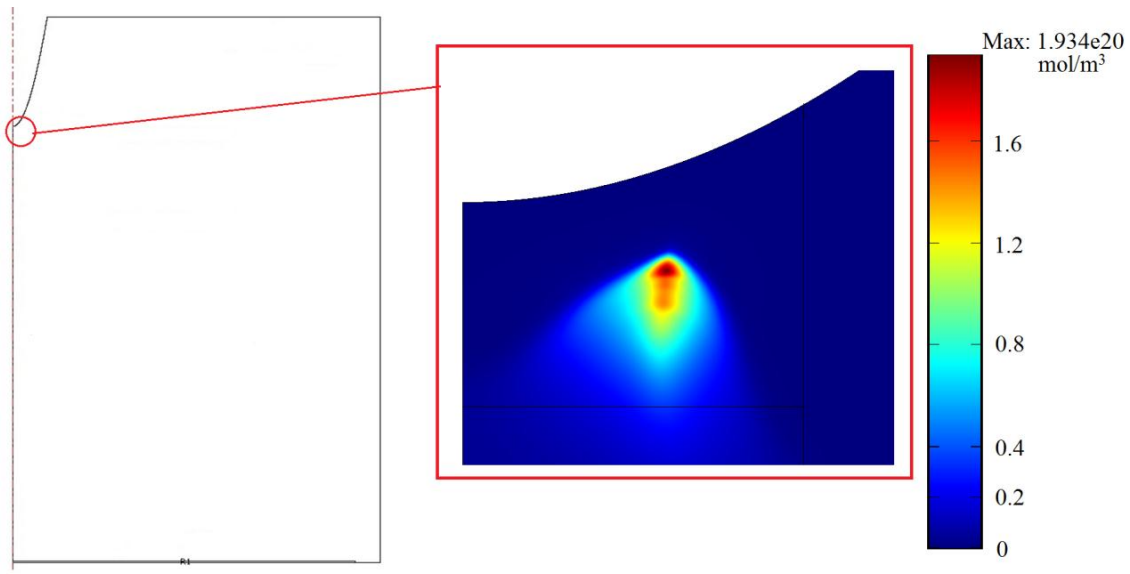


Figure 8-7 Electron density plot at 0.6 μs (peak of first impulse current in model I)

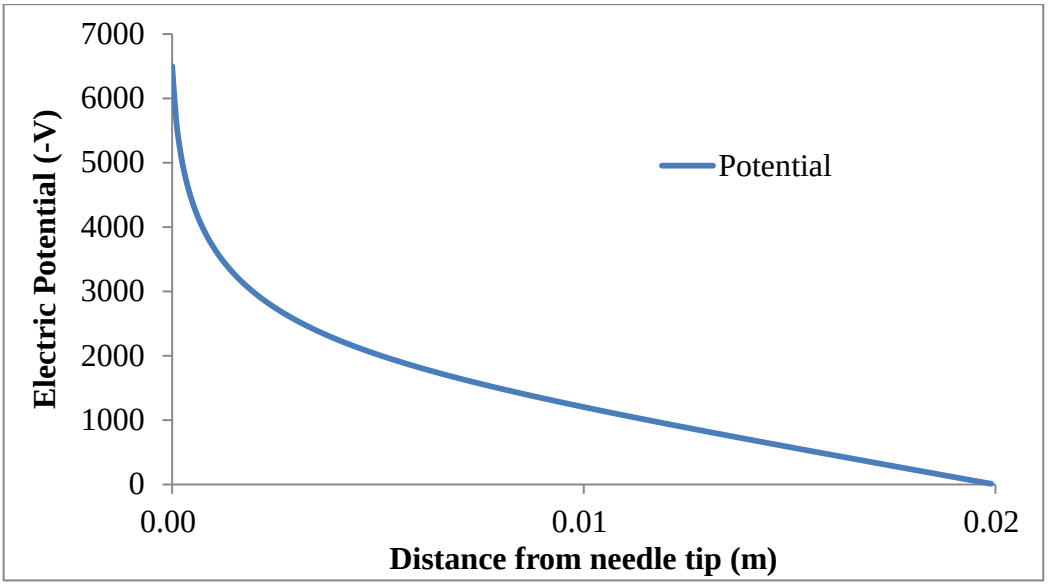


Figure 8-8 Electric potential distribution along the symmetry axis

### *8.3.2 Effect of the geometry of grid electrode*

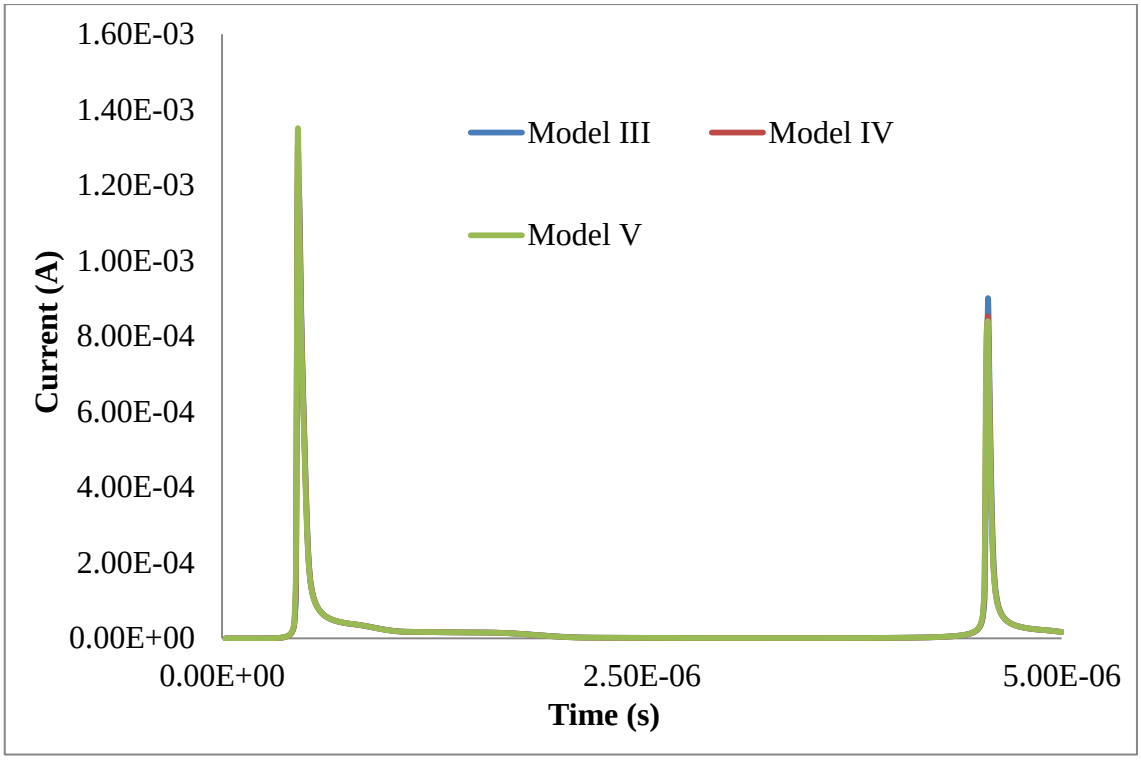


Figure 8-9 Current for models III, IV and V

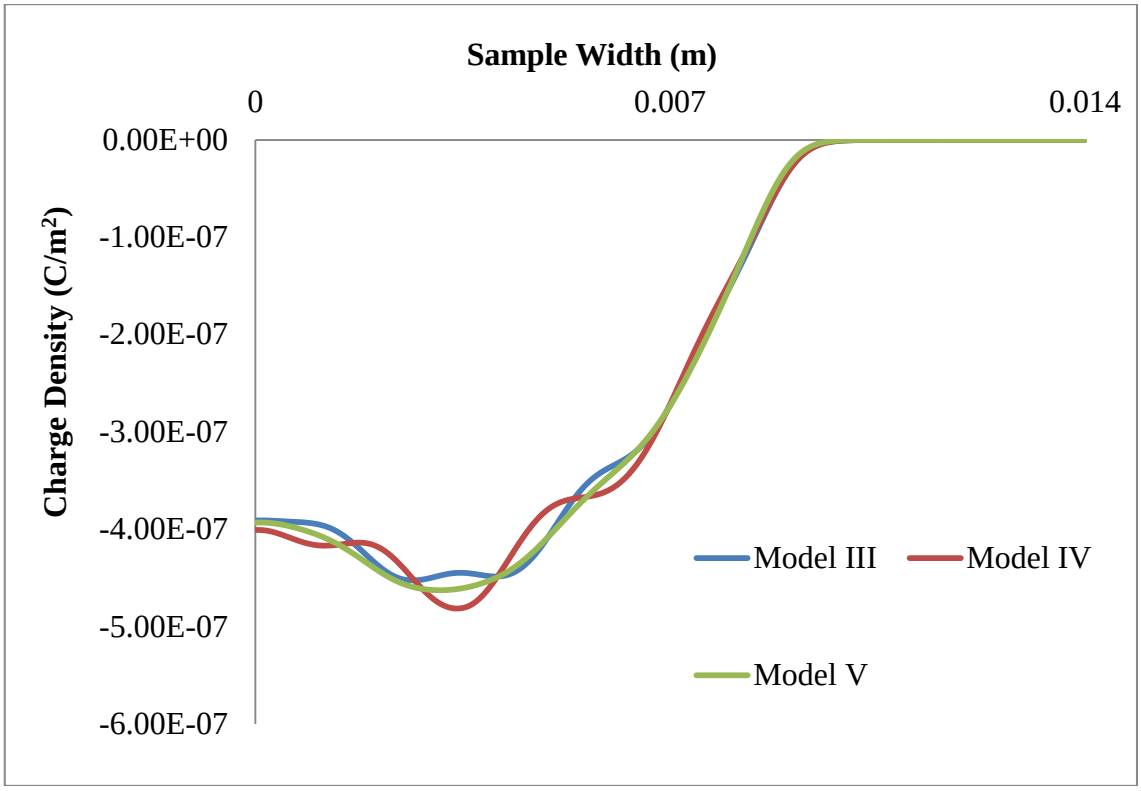


Figure 8-10 Surface charge densities for models III, IV and V at 5 μs

The real grid electrode is a fine mesh which varies in width and gap, which is different from the one built in the current model. Therefore, three different geometries (model III, IV and V in Table 8-3) of the grid electrode were selected and modelled to observe any possible effects of the mesh geometry to the surface charge density at the polymer. The results for these models are shown in Figures 8-9 and 8-10. From those graphs, it is clear to see that the difference between the surface charge density is insignificant. From these models, it can be noticed that at the beginning of the corona charging process, the electrons will travel from the cathode to the sample as model I; however with the infinitely thin grid electrode in the current models, the electrons can pass through the mesh and mainly through the gaps of the mesh. In Figure 8-11, the logarithm plot of the electrons is shown at three different simulation times: 0.01 μs, 0.5 μs and 1 μs. It is clear to see that at the beginning of the simulation, a cloud of electrons sits underneath the needle electrode and then they were pushed towards the polymer; the process of how electrons passing through the grid electrode can be also observed clearly from 0.5 μs and 1 μs results. Therefore, it can be said that a 2D-axis symmetry model can be used with confidence to simulate corona charging process, and it is much more efficient than a larger 3D model.

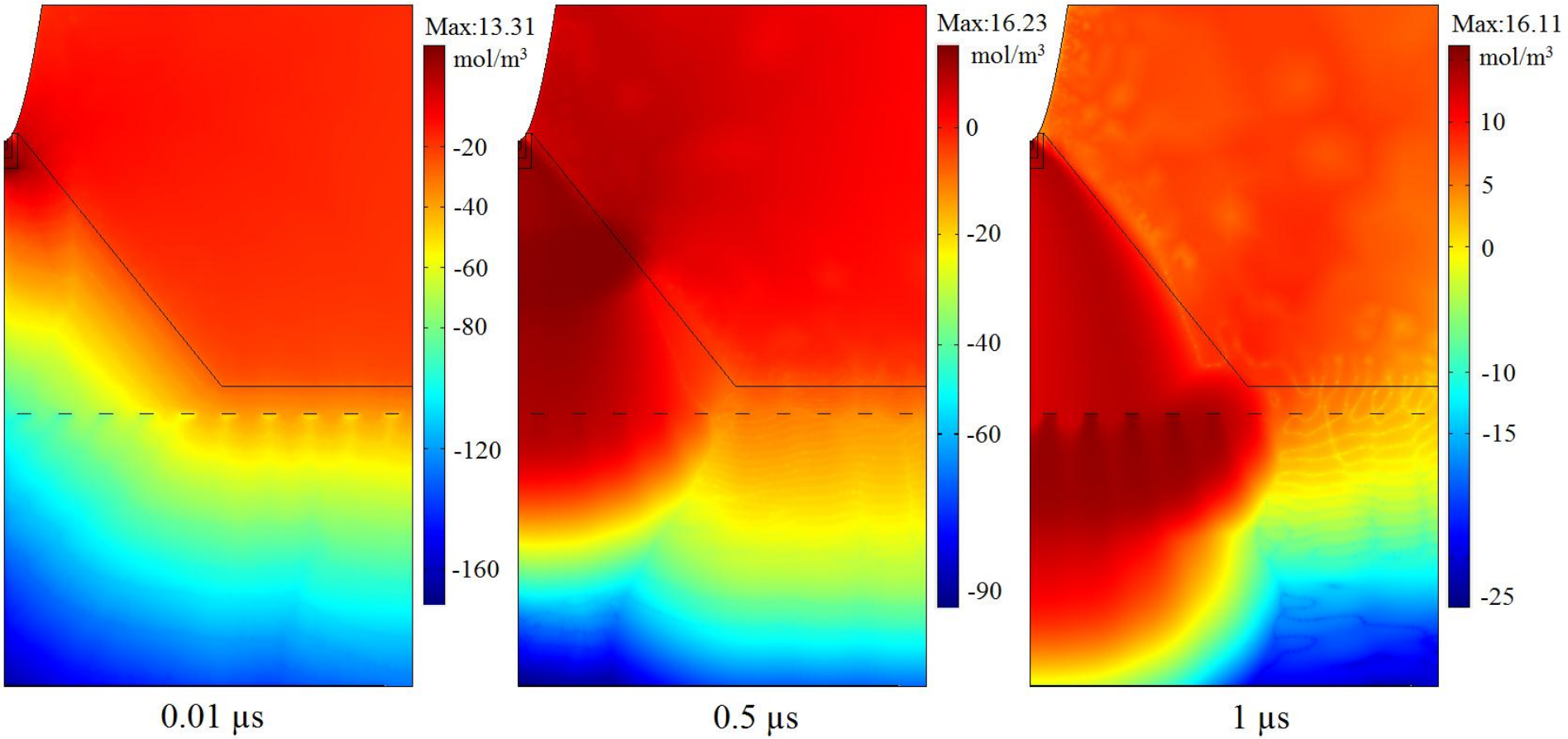


Figure 8-11 Logarithm plot of electrons for model III at different times

## 8.4 Conclusion

It can be concluded that by adding the grid electrode into the corona charging system the whole system will be affected. Varying the distances between the grid electrode and the ground will result in a different impulse current and therefore make the surface charge density difference. The place of the grid electrode is usually suggested placing close to the sample to get a more controllable surface potential. The electric potential of the grid can be referenced from Figure 8-8 It has been found experimentally that if the grid potential were selected too low, its potential can be brought up by the needle potential; if the grid potential were selected too high, no corona effect can be observed from the needle. Our simulation results showed that the different grid electrode geometries do not affect much the current or the surface charge density at 5 μs. However, much longer solving time might be necessary to observe any possible effects of the grid electrode, and our model should be useful for such future observations.

# Chapter 9 Conclusions and Future Work

## 9.1 Conclusions

This report focuses on the research into charge transport under corona charged polyethylene. The research work had been accomplished by experimental works and modelling works on surface potential decay of corona charged additive free LDPE film. Also, nano-polyimide materials had been tested to exam its insulation properties. The characteristics of gas discharge during the corona charging process were also investigated by simulation. Based on this fundamental work, several conclusions can be drawn.

Initially, the well-known cross-over phenomenon can be clearly seen on the potential decay of negatively corona charged LDPE sample. Bipolar charge injection had been observed from the space charge distribution using the pulsed electro-acoustic method. To confirm the importance of the charge injection from the ground electrode, samples with two different types of ground electrodes were examined (aluminium and gold). The

differences between aluminium ground sample and gold ground sample can be clearly seen from the surface potential decay measurements, the corona charging current measurements and space charge measurement. As the work function of aluminium is different from gold, it was assumed that gold ground sample had less charge injected into the material than aluminium ground sample. This is more obviously when the corona charging voltage is high. A bipolar charge transport simulation model was also built to verify that the charge injection from the ground electrode plays a particularly significant role during the corona charging and potential decaying processes.

The experimental work on the effect of different polarity was carried out. It had been observed that the surface potential decay of positive corona charged sample cannot cross-over each other, which represent that the decay rate is slow than the negative corona charged sample. A corona charging current measurement also showed that positive polarity gave a smaller amount of charge injection than the negative polarity. This tells us the slower decay was caused by charge injection. It had been reported that negative corona charges contain electrons and negative ions and positive corona charges contain only positive ions. This fact had been agreed in Reference [18] to be the main reason that causes the slower decay for positive charges. The effect of different corona charging time was also tested. Due to the lack of research on this area, only a few papers had mentioned its properties, and all of them agreed that a longer corona charging time lead to a faster decay within 1 min charging. In this report, the corona charging time was extended to 10 min and surprisingly the potential decays faster and faster initially when increasing the charging time but it becomes slower and slower if continue to increasing the charging time. This is true for both positive charge and negative charge, but the turning point is different with different corona charging voltage. To get a better understanding about this phenomenon, space charge distribution had been observed after the samples were corona charged at different charging voltage and time. The results on – 8 kV with 4 min charging showed a positive charge packet in the bulk of the material. It was reported that charge packet can be only observed if the injection is truly large. As the charge packet was not observed in shorter charging time, it was hypothesised that the charge injection is not constant during the corona charging process.

Bipolar charge transport model concerning with bipolar charge carrier injection at the dielectric surface, charge transport with trapping and recombination had been developed to simulate charge dynamics in polyethylene subjected to electric fields. The simulation with symmetric parameterization for positive charge (holes) and negative charge (electrons) produced the basic surface potential decay curve and proved that this model can be used to simulate the surface potential decay processes. A fit of simulation result with experimental measurement had been achieved by optimizing the parameters in the model. To make the adjustment more controllable, only one parameter was changed for single simulation. More importantly the influence of essential parameters related to the properties of material on the behaviour of surface potential decay had been revealed through the simulation, which indicates that the charge injection, charge transportation and trapping in the bulk of polyethylene play significant roles in the surface potential decay processes. This can help the researcher to understand the physical process during the decay which cannot be observed experimentally at the moment.

For the nano-PI examination, the surface potential decay results can give a good agreement with the DC conductivity results. It had been found that the best quantity of adding nano-$TiO_2$ into polyimide to improve its insulation properties is 3% from these tested samples.

For the modelling on gas discharge, it can be learnt that the grid electrode plays an influential role during the corona charging process and its position will affect the surface charge density of the sample.

## 9.2 Future work

The bipolar charge transport model is able to present the surface potential decay curves, and the simulation results can fit the experimental results by adjusting the parameters. However, current parameter selections are using the same value for both electrons and holes expect charge injection barrier height. This may not be true as positive charges and negative charges behave differently inside the material. Also, most parameters were

kept constant during one single simulation in the current model, this is the main reason why the currently cannot fit all the experimental data with unique parameters. However, the model can be improved by adding either time dependent parameters or electric field dependent parameters to simulate a group of experimental data with the same parameters.

In present, parameters of charge injection barrier height, trapping coefficient, trap density and recombination coefficient cannot be directly measured by experiments. This results in that the value of these parameters changes in a wide range. Although the final simulation results can still fit the experimental results if adjusting other parameters in the model, the model cannot definitively present the true physical process. The selections of parameters also need plenty of experimental results to support it or to narrow down to a reasonable range. However, the bipolar charge transport model has also been used to simulate other experimental results such as space charge, charge packet, DC breakdown and electroluminescence (EL) etc., therefore, if researchers were carried out their experiments using the same sample and simulated the experimental results using the same model, the model can be improved, and the range of parameters values can be also narrowed down.

More experimental work can be development to find out value of injection barrier height, trap density and trap depth. Chemical analysis on the corona charged sample can also be made to see if the corona charging process may change the material's chemical structure such as cross-linking and chain scission, or some extra defects may be generated at the surface. More importantly, the results can be used to optimize the parameters in the simulation model.

# Appendix A Matlab code for bipolar charge transport model

Charging Parameters:

```
clear
clc

%By Yuan ZHUANG in 2011
%3rd year PhD in EPE group of ECS
%Modelling of decay of surface potential on LDPE surface corona charged under DC
Field
%Supervisor : Prof. George Chen & Dr. Mihai Rotaru
%Simulation Source Code

%Defination of constants
global V d m alt dx dt K ec epr Be Bh S0 S1 S2 S3 Ue Uh U0 U01 n Eot Hot Wei Whi
A T A1 bb Dei Dhi v_dt;
%----------------------------------------
alt=12e2;                   %number of iterations
V=-4e3;                     %External applied voltage (in volts)
d=50e-6;                    %sample thickness (in metres) / interelectrode spacing
m=50;                       %number of equal divisions
dx=(d/m);                   %divisional length -- 1.0e-6
dt=0.1;                     %time step = time difference between each loop ( in
secs )/10^-2
K=1.380658e-23;             %Boltzmann's constant
```

```
ec=1.6e-19;                 %Electronic charge
epr=2.3*8.85e-12;           %Permittivity of the Sample material
Bh=7.0e-4;                  %Trapping coefficient for holes ( s^-1 )
Be=7.0e-4;                  %Trapping coefficient for electrons ( s^-1 )
%Recombination coefficients ( m^3 C^-1 s^-1 )for
S0=4e-3;                    %trapped electron/trapped hole
S1=4e-3;                    %mobile electron/trapped hole
S2=4e-3;                    %trapped electron/mobile hole
S3=0;                       %mobile electron/mobile hole
U01=9e-15;                  %electron mobility
U0=9e-15;                   %hole mobility
Eot=100;        Hot=100;    %Trap density for electrons & holes
Whi=1.1;        Wei=1.1;    %Barrier Height for injection for electrons & holes
A=1.2e6;                    %Richardson constant [ Am^-1K^-2 ]
T=295;                      %Room Temperature ( in Kelvin )
set_completed=1;            %initiation / defination of working matrix
E=zeros(1,m);               %Mobile Electron densities
H=zeros(1,m);               %Mobile hole densities
Et=zeros(1,m);              %Densities of Trap Electon
Ht=zeros(1,m);              %Densities of Trap Hole
N=(H - E + Ht - Et);        %Effective Current density
JE=zeros(1,m-1);            %Current density of electrons
JH=zeros(1,m-1);            %Current density of holes
DC=zeros(1,m-1);            %Density of Displacement current
TC=(JE + JH + DC);          %Total current density
F=zeros(1,m);               %Electric field
Ue=zeros(1,m);
Uh=zeros(1,m);

fprintf('Simulation of corona charging \n');
fprintf('DC %3dkV on %4dum LDPE disc\n',V/1e3,d*1e6);

% Start of time
Ts=clock;
```

```
fprintf('Start time: %4d-%2d-
%2d %2d:%2d:%2d\n',Ts(1),Ts(2),Ts(3),Ts(4),Ts(5),fix(Ts(6)/1));

% Program starts
[ch,F1,DC1,TC1,U1,Esave,Hsave,Etsave,Htsave,JEsave,JHsave,E,H,Et,Ht,JE,JH,F,N,D
C,TC]=Yuan_prog_linx(E,H,Et,Ht,JE,JH,F,N,DC,TC);

% End of time
set_completed=set_completed+1
Te=clock;
fprintf('End time: %4d-%2d-
%2d %2d:%2d:%2d\n',Te(1),Te(2),Te(3),Te(4),Te(5),fix(Te(6)/1));

%=====save values===============
savefile = 'linxq_Neg4000V_120s_corona_50um_1111_trap_70_4_70_4_u_90_90.mat'
save(savefile,'ch','F1','DC1','TC1','U1','Esave','Hsave','Etsave','Htsave','JEsave','JHsave','
set_completed','E','H','Et','Ht','JE','JH','F','N','DC','TC');
%================================
```

## Charging Processes:

```
function
[ch,F1,DC1,TC1,U1,Esave,Hsave,Etsave,Htsave,JEsave,JHsave,E,H,Et,Ht,JE,JH,F,N,D
C,TC]=Yuan_prog_linx(E,H,Et,Ht,JE,JH,F,N,DC,TC)

global V d m alt dx dt K ec epr Wei Whi Ue Uh U0 U01 A T;

a=1;    %index of the 1st iteration
F0=F;   %electric field at time t=0s
% -------------------
% Program
% -------------------

format long;
```

```
% -------------------
% Poisson's Equation
% -------------------

for t=1:alt

   for k = 1:m

      b = 0;
      for i = 1:k
      temp(i) = (i-0.5)*N(i);
      b = b + temp(i);
      end

      c = 0;
      for w = k:m
      temp1(w) = (m-w+0.5)*N(w);
      c = c + temp1(w);
      end

   F(k) =(V/d)-((dx/(m*epr))*(b-c));
   Ue(k)=U0;
   Uh(k)=U01;


   end  %for electric field F(k)
   F1(a:t*m)=F;
   U1(a:t*m)=Ue;

   for k=1:(m-1)
      if a==1
          DC(k)=epr*((F(k)-F0(k))/dt);
      else
          Fn=F1((a-m):(t-1)*m);
```

```
            DC(k)=epr*((F(k)-Fn(k))/dt);
        end
    end  %for displacement current DC(k)
    DC1(a:(t*m)-1)=DC;


% ------------------------------
% Transport & Continuity Equation
% ------------------------------
% solve for the s value ( by assuming J value can be formulated )
% Schottky Injection for E at Cathode(k=1) and H at Anode (k=m)

JH_Anod = A*T^2*exp([-
(ec*Whi/(K*T))])*exp([(ec/(K*T))*sqrt((ec*abs(F(1)))/(4*pi*epr))]);
JE_Catd = A*T^2*exp([-
(ec*Wei/(K*T))])*exp([(ec/(K*T))*sqrt((ec*abs(F(m)))/(4*pi*epr))]);

for k=1:(m-1)

    JH(k) = Uh(k)*H(k)*abs(F(k));
    JE(k) = Ue(k+1)*E(k+1)*abs(F(k+1));

end

JEsave(a:(t*m)-1)=JE;
JHsave(a:(t*m)-1)=JH;

TC=JE + JH + DC;        %Total current density added as shown
TC1(a:(t*m)-1)=TC;

%Extraction of electrons and holes respectively at the Anode and Cathode under no
extraction barrier
JE_Anod = Ue(1)*E(1)*abs(F(1));
JH_Catd = Uh(m)*H(m)*abs(F(m));
```

```
% ------------------ODE initial condition----------------

% for k=1 (first division)
H(1) = (-(JH(1) - JH_Anod)/dx)*(dt) + H(1);
E(m) = (-(JE(m-1) - JE_Catd)/dx)*(dt) + E(m);

for k=2:m-1

   H(k) = (-(JH(k) - JH(k-1))/dx)*(dt) + H(k);
   E(k) = (-(JE(k-1) - JE(k))/dx)*(dt) + E(k);

end % for E & H --> PDE initial condition

H(m) = (-(JH_Catd - JH(m-1))/dx)*(dt) + H(m);
E(1) = (-(JE_Anod - JE(1))/dx)*(dt) + E(1);



% --------------------PDE solver---------------------------
for k=1:m

tspan = [0 dt];
y0 = [E(k), H(k), Et(k), Ht(k)];
sol = ode45(@f,tspan,y0);

x = dt;
y = deval(sol,x);

%------- setting the output of ODE to the species value ------
E(k) = y(1,:);
H(k) = y(2,:);
Et(k) = y(3,:);
Ht(k) = y(4,:);
```

```
end % for ODE solver

Esave(a:t*m)=E;
Hsave(a:t*m)=H;
Etsave(a:t*m)=Et;
Htsave(a:t*m)=Ht;

N = (H - E + Ht - Et);
ch(a:t*m)=N;

a=a+m;
% t

if mod(t*dt,1)==0
    fprintf('Time step is 0.1s; Charging proceeded for%6ds.\n',t*dt);
end

end % for iterations

% ------------------------------------------------------------
function dNdt = f(t,y)

global Be Bh S0 S1 S2 S3 Eot Hot;

% y1 = E, y2 = H, y3 = Et, y4 = Ht
dNdt = [ -S1*y(4)*y(1) - S3*y(2)*y(1) - Be*y(1)*(1-(y(3)/Eot))
        -S2*y(2)*y(3) - S3*y(2)*y(1) - Bh*y(2)*(1-(y(4)/Hot))
        -S2*y(2)*y(3) - S0*y(4)*y(3) + Be*y(1)*(1-(y(3)/Eot))
        -S1*y(4)*y(1) - S0*y(4)*y(3) + Bh*y(2)*(1-(y(4)/Hot))];

%-------------------------------------------------------------
%                    * * END * *
%-------------------------------------------------------------
```

Decaying Parameters:

```
clear
clc

%By Yuan ZHUANG in 2011
%3rd year PhD in EPE group of ECS
%Modelling of decay of surface potential on LDPE surface corona charged under DC Field
%Supervisor : Prof. George Chen & Dr. Mihai Rotaru
%Simulation Source Code

%Defination of constants
global V d m alt dx dt K ec epr Be Bh S0 S1 S2 S3 Ue Uh U0 U01 n Eot Hot Wei Whi A T A1 bb Dei Dhi v_dt;

alt=60e2;                   %number of iterations
V=-4e3;                     %Initially applied voltage ( in volts )
d=50e-6;                    %sample thickness (in metres) / interelectrode spacing
m=50;                       %number of equal divisions
dx=(d/m);                   %divisional length -- 1.8e-6
dt=0.1;                     %time step = time difference between each loop ( in secs )/10^-2
K=1.380658e-23;             %Boltzmann's constant
ec=1.6e-19;                 %Elementary electronic charge
epr=2.3*8.85e-12;           %Permittivity of the Sample material
Bh=7.0e-2;      Be=7.0e-2;  %Trapping coefficient for electrons & holes ( s^-1 )
%Recombination coefficients ( m^3C^-1s^-1 )for
S0=4e-3;                    %trapped electron/trapped hole
S1=4e-3;                    %mobile electron/trapped hole
S2=4e-3;                    %trapped electron/mobile hole
S3=0;                       %mobile electron/mobile hole
U01=9e-15;                  %electron mobility
U0=9e-15;                   %hole mobility
Eot=100;        Hot=100;    %Trap density for electrons & holes
```

```
Whi=1.1;          Wei=1.1;     %Barrier Height for injection for electrons & holes
A=1.2e6;                       %Richardson constant [ Am^-1K^-2 ]
T=295;

Ue=zeros(1,m);
Uh=zeros(1,m);



fprintf('Modelling of surface-potential decay \n');
fprintf('DC %3dkV on %4dum LDPE disc\n',V/1e3,d*1e6);
timestart=clock

%=====load corona charged data at 120s======
load
('linxq_Neg4000V_120s_corona_50um_1111_trap_70_2_70_2_u_90_90.mat','E','H','Et'
,'Ht','JE','JH','F','N');

%=====First 120s iteration=====
[ch,F1,Q0,Q1,Q2,V1,U1,Esave,Hsave,Etsave,Htsave,JEsave,JHsave,E,H,Et,Ht,JE,JH,F,
N]=Yuan_prog_linx_decay(E,H,Et,Ht,JE,JH,F,N);
% set_completed
timedone=clock

%=======save values============
savefile =
'linxq_Neg4000V_50um_corona_120s_decay_600s_1111_trap_70_2_70_2_u_90_90.m
at'
save(savefile,'ch','F1','Q0','Q1','Q2','V1','U1','Esave','Hsave','Etsave','Htsave','JEsave','JH
save','E','H','Et','Ht','JE','JH','F','N');
%============================
```

Decaying Processes:

```
function
[ch,F1,Q0,Q1,Q2,V1,U1,Esave,Hsave,Etsave,Htsave,JEsave,JHsave,E,H,Et,Ht,JE,JH,F,
N]=Yuan_prog_linx_decay(E,H,Et,Ht,JE,JH,F,N)

global V d m alt dx dt K ec epr Be Bh S0 S1 S2 S3 Ue Uh U0 U01 n Eot Hot Wei Whi
A T v_dt Dei Dhi;

% ************************ Program start ************************

format long;

a=1;                    %index of the 1st iteration
V1(1)=V;                %initial surface potential at x=d
JH_Catd=0;
JE_Catd=0;



for t=1:alt

  for k = 1:m
      b = 0;
    for i = 1:k
      b = b + (i-0.5)*N(i);
    end
      c = 0;
    for w = k:m
      c = c + (m-w+0.5)*N(w);
    end
    F(k) = (dx/(m*epr))*(b-c);
  end                   % internal electric field by bulk charge
    g0 = 0;
  for k=1:m
    g0=g0+F(k)*dx;
```

```
end
V0(t)=-g0;                % internal potential by bulk charge
   z=0;
for i=1:m
   z=z+N(i);
end
Q0(t)=z;                  % bulk charge density, C/m^3
if  t==1
   Q1(t)=((2*epr/d)*(V1(t)-V0(t))-Q0(t)*dx)/2;
else
   Q1(t)=Q1(t-1)+JE_Catd*dt;
end                       % negative charge on free surface
Q2(t)=-Q1(t)-Q0(t)*dx;     % positive charge on grounded surface

for k=1:m
   F(k)=F(k)+(Q2(t)-Q1(t))/(2*epr);
end
% ---------- Open circuit condition: epr*(dE/dt)+J(x)=0 ----------
for k=1:(m-1)
   F(k)=F(k) - (dt/epr)*(JH(k)+JE(k));
   Ue(k)=U0;
   Uh(k)=U01;
end
   F(m)=F(m) - (dt/epr)*(JH_Catd+JE_Catd);
   Ue(m)=U0;
   Uh(m)=U01;
F1(a:t*m)=F;
U1(a:t*m)=Ue;

   g1 = 0;
for k=1:m
   g1=g1+F(k)*dx;
end
V1(t+1)=-g1;
```

```
% ---------- Transport & Continuity Equation ----------
% solve for the s value ( by assuming J value can be formulated )
% Schottky Injection for H at Anode(k=1) and E at Cathode(k=m)
% -----------------------------------------------------------
   JH_Anod = A*T^2*exp([-
(ec*Whi/(K*T))])*exp([(ec/(K*T))*sqrt((ec*abs(F(1)))/(4*pi*epr))]);
   JE_Catd = A*T^2*exp([-
(ec*Wei/(K*T))])*exp([(ec/(K*T))*sqrt((ec*abs(F(m)))/(4*pi*epr))]);

   for k=1:(m-1)

      JH(k) = Uh(k)*H(k)*abs(F(k));
      JE(k) = Ue(k+1)*E(k+1)*abs(F(k+1));

   end
   JHsave(a:(t*m)-1)=JH;
   JEsave(a:(t*m)-1)=JE;

% Extraction of E and H respectively at the Anode and Cathode under no extraction
barrier
   JE_Anod = Ue(1)*E(1)*abs(F(1));
   JH_Catd = Uh(m)*H(m)*abs(F(m));

% ------------------PDE initial condition-------------------

   H(1) = (-(JH(1) - JH_Anod)/dx)*(dt) + H(1);
   E(m) = (-(JE(m-1) - JE_Catd)/dx)*(dt) + E(m);

   for k=2:m-1

      H(k) = (-(JH(k) - JH(k-1))/dx)*(dt) + H(k);
      E(k) = (-(JE(k-1) - JE(k))/dx)*(dt) + E(k);

   end
```

```
    H(m) = (-(JH_Catd - JH(m-1))/dx)*(dt) + H(m);
    E(1) = (-(JE_Anod - JE(1))/dx)*(dt) + E(1);

% --------------------PDE solver--------------------------
    for k=1:m

        tspan = [0 dt];
        y0 = [E(k), H(k), Et(k), Ht(k)];
        sol = ode45(@f,tspan,y0);

        x = dt;
        y = deval(sol,x);

        E(k) = y(1,:);
        H(k) = y(2,:);
        Et(k) = y(3,:);
        Ht(k) = y(4,:);

    end % for ODE solver
    Esave(a:t*m)=E;
    Hsave(a:t*m)=H;
    Etsave(a:t*m)=Et;
    Htsave(a:t*m)=Ht;

    N = (H - E + Ht - Et);
    ch(a:t*m)=N;

    a=a+m;

    if mod(t*dt,1)==0
        fprintf('Time step is 0.1s; Decaying proceeded for%6ds.\n',t*dt);
    end
```

```
end % for iterations

% ------------------------------------------------------------
function dNdt = f(t,y)

global Be Bh S0 S1 S2 S3 Eot Hot Dei Dhi;

% y1 = E, y2 = H, y3 = Et, y4 = Ht
dNdt = [ -S1*y(4)*y(1) - S3*y(2)*y(1) - Be*y(1)*(1-(y(3)/Eot))
        -S2*y(2)*y(3) - S3*y(2)*y(1) - Bh*y(2)*(1-(y(4)/Hot))
        -S2*y(2)*y(3) - S0*y(4)*y(3) + Be*y(1)*(1-(y(3)/Eot))
        -S1*y(4)*y(1) - S0*y(4)*y(3) + Bh*y(2)*(1-(y(4)/Hot))];

%------------------------------------------------------------
%                    * * END * *
%------------------------------------------------------------
```

# References


[1] T Tanaka and A Greenwood, *Advanced Power Cable Technology,* Boca Raton, Fla. : CRC Press, 1983

[2] B M Weedy, *Underground Transmission of Electric Power,* New York: John Wiley & Sons, 1980

[3] P Graneau, *Underground power transmission : the science, technology, and economics of high voltage cables*, New York : Wiley, 1979

[4] *http://www.chemistrydaily.com/chemistry/Polymer* Viewed on 13th Apr. 2010

[5] X Wang, N Yoshimura, D Tu, Y Tanaka and T Takada, *"Distribution characteristics and formation mechanism of space charge in PE materials"*, Proceedings of International Symposium on Electrical Insulating Materials, 1998.

[6] *http://en.wikipedia.org/wiki/*Polyethylene Viewed on 21st Apr., 2010

[7] G Parker, *Introductory Semiconductor Device Physics,* New York: Taylor & Francis Group, 2004

[8] B G Streetman and S Banerjee, *Solid State electronic Devices (5th edition),* New Jersey: Prentice Hall, 2000

[9] J Dharma and A Pisal, "*Simple method of measuring the band gap energy value of TiO2 in the powder form using a UV/Vis/NIR spectrometer",* Application note on UV/Vis/NIR Spectrometer, 2009

[10] R Hoffmann, C Jaiak and C Kollmar, *"A chemical approach to the orbitals of organic polymers",* Macromolecules, 24, 3725-3746, 1991.

[11] M Meunier and N Quirke, "*Molecular modeling of electron trapping in polymer insulators",* J. Chem. Phys., 113, 369-376, 2000.

[12] M Meunier and N Quirke, *"Molecular modeling of electron traps in polymer insulators: Chemical defects and impurities"*, J. Chem. Phys., 115, 2876-2881, 2001.

[13] S L Roy, P Segur, G Teyssedre and C Laurent, *"Description of bipolar charge transport in polyethylene using a fluid model with a constant mobility: model prediction"*, J. Phys. D: Appl. Phys., 37, 298-305, 2004

[14] M. Ieda, G. Sawa and I. Shinohara, *"A decay process of surface electric charges across polyethylene film"*, J. Appl. Phys., 6, 793-794, 1967

[15] P Molinié, *"Charge injection in corona-charged polymeric films: potential decay and current measurements"*, J. Electrostatics, 45, 265-273, 1999

[16] T J Sonnonstine and M M Perlman, "*Surface-potential decay in insulators with field-dependent mobility and injection efficiency"*, J. Appl. Phys., 46 3975-3981, 1975

[17] H J Wintle, "*Surface-Charge Decay in Insulators with Non-constant mobility and with Deep Trapping"*, J. Appl. Phys., 43, 2927-2930, 1972

[18] E A Baum, T J Lewis and R Toomer, "*Decay of electrical charge on polyethylene films"*, J, Phys. D: Appl. Phys., 10, 487-497, 1977

[19] H V Berlepsch, "*Interpretation of surface potential kinetics in HDPE by a trapping model",* J. Phys. D: Appl. Phys., 18, 1166-70, 1985

[20] B Lutz and J Kindersberger, *"Determination of volume resistivity of polymeric insulators by surface charge decay",* Proceedings of the 16th International Symposium on High Voltage Engineering, Innes House, Johannesburg, 2009

[21] Z Xu, L Zhang and G Chen *"Decay of electric charge on corona charged polyethylene"*, J. Phys. D: Appl. Phys., 40, 7085-7089, 2007

[22] I P Batra, K D Kanazawa and H Seki, *"Discharge characteristics of photoconducting insulator"*, J. Appl. Phys., 41, 3416-3422, 1970

[23] D W Vance, *"Surface charging of insulators by ion irradiation"*, J.Appl. Phys., 42, 5430-5443, 1971

[24] P K Watson, "T*he transport and trapping of electrons in polymers",* IEEE Trans. Dielectr. Electr. Insul., 2, 915-924, 1995

[25] R H Young, *"Kinetics of xerographic discharge by surface charge injection"*, J. Appl. Phys., 42, 5430-5443, 1971

[26] P Molinié, *"A review of mechanisms and models accounting for surface potential decay"*, IEEE Trans. Plasma Sci., 40, 167-176, 2012

[27] G F Leal Ferreira and M T Figueiredo, "*Corona charging of electrets – models and results"*, IEEE Trans. Elect. Insul., 27, 719-738, 1992

[28] G M Sessler, C Alquié and J Lewiner, "*Charge distribution in Teflon FEP (fluoroethylenepropylene) negatively corona-charged to high potentials"*, J. Appl. Phys., 71, 2280-2284, 1992

[29] H Amjadi, "*The mechanism of voltage decay in corona-charged layers of silicon dioxide during UV irradiation*", IEEE Trans. Dielectr. Elect. Insul., 7, 222-228, 2000

[30] G M Sessler, "*Charge storage in dielectrics*", IEEE Trans. Elect. Insul., 24, 395-402, 1989

[31] B Gross, "*On discharge voltage and return voltage curves for absorptive capacitors*", Phys. Rev., 62, 383-387, 1942

[32] R A Moreno and B Gross, "*Measurement of potential buildup and decay, surface charge density, and charging currents of corona-charged polymer foil electrets*", J. Appl. Phys., 47, 3397-3402, 1976

[33] M Campos and J A Giacometti, "*Surface-potential decay in insulators with deep traps*", J. Appl. Phys., 52, 4546-4552, 1981

[34] A R Frederickson, "*Upsets related to spacecraft charging*", IEEE Trans. Nucl. Sci., 43, 426-441, 1996

[35] J F Fennell, H C Knoons, M S leung and P F Mizera, *A review of SCATHA satellite results: charging and discharging*, Los Angeles, CA, Tech. Rep., 1985

[36] D Payan, R Reulet and B Dirassen, "*Electrostatic behavior of dielectrics under GEO-like charging space environment simulated in laboratory*", 9th Spacecraft Charging Technology Conference, 2005

[37] L Levy, T Paulmier, B Dirassen, C Inguimbert and M Van Eesbeek, "*Aging and prompt effects on space material properties*", IEEE Trans. Plasma Sci., 36, 2228-2237, 2008

[38] T Paulmier, B Dirassen, D Payan and M Van Eesbeek, "*Material charging in space environment: experimental test simulation and induced conductive mechanisms*", IEEE Trans. Dielectr. Elect. Insul., 16, 682-688, 2009

[39] R Coelho, "*The electrostatic characterization of insulating materials*", J. Electrostatics, 17, 13-27, 1985

[40] R Coelho, L Levy and D Sarrail, "*On the natural decay of corona charged insulating sheets*", Phys. Stat. Sol., 94, 289-298, 1986

[41] R Coelho, P Jestin, L Levy and D Sarrail, "*On the return-voltage buildup in insulating materials*", IEEE Trans. Elect. Insul., E1-22, 683-690, 1987

[42] G M Sessler, "*Bernhard Gross and the evolution of modern electret research*", Braz. J. Phys., 29, 220-224, 1999

[43] A R Frederickson, C E Benson and J F Bockman, "*Measurement of charge storage and leakage in polyimides*", Nuclear Instruments and Methods in Physics Research Section B, 208, 454-460, 2003

[44] C Perrin, V Griseri, C Inguimbert and C Laurent, "*Analysis of internal charge distribution in electron irradiated polyethylene and polyimide films using a new experimental method*", J. Phys. D, Appl. Phys., 41, 205 417, 2008.

[45] R Hanna, T Paulmier, M Belhaj, P Molinié, B Dirassen, D Payan and N Balcon, "*Characterization of electrical transverse conductivity of space dielectric materials*", IEEE 14th International Symposium on Electrets (ISE), 2011

[46] G M Sessler and G M Yang, "*Charge dynamics in electron irradiated polymers*", Braz. J. Phys., 29, 233-239, 1999

[47] J Malecki, "*Dynamics of radiation-induced conductivity in the presence of spatial charge*", J. Electrostatics, 50, 109-117, 2001

[48] M A Noras *"Non-contact surface charge/voltage measurements"*, Trek Application Note 3001, 2002

[49] D A Hill, K Motohisa *Measurement, Instrumentation, and Sensors Handbook*, CRC Press LLC, 1999

[50] G Chen, Z Xu and L W Zhang "*Measurement of the surface potential decay of corona-charged polymer films using the pulsed electroacoustic method"*, Meas. Sci. Technol., 18, 1453-1458, 2007

[51] P Llovera, P Molinié, A Soria and A Quijano *"Measurements of electrostatic potentials and electric fields in some industrial applications: Basic principles"*, J. Electrostatics, 67, 457-461, 2009

[52] E Kuffel, W S Zaengl and J Kuffel, *High Voltage Engineering: Fundamentals*, Linacre House, Jordan Hill, Oxford, 2000

[53] L Herous, M Nemamcha and S Saad, *"Experimental Investigation on Surface Potential Kinetics in Polyethylene Terephtalate (PET)"*, J. Engineering and Appl. Sci., 1, 329-334, 2006

[54] B Lutz and J Kindersberge, "*Influence of Relative Humidity on Surface Charge Decay on Epoxy Resin Insulators"*, Proceedings of the 9th International Conference on Properties and Applications of Dielectric Materials, 2009

[55] User Manual: JCI 140 Static Monitor, UM 140 issue 21: September 2007

[56] J Lewiner, "*Evolution of experimental techniques for the study of the electrical properties of insulating materials"*, IEEE Trans. Electr. Insul., 21 351-360, 1986

[57] A Cherifi, M Abou-Dahka and A Toureille, *"The validation of the thermal step method"*, IEEE Tran. Dielectr. Electr. Insul., 27, 1152-1158, 1992

[58] Y Li, M Yasuda and T Takada, "*Pulsed electroacoustic method for measurement of charge accumulation in solid dielectrics*", IEEE Trans. Dielectr. Electr. Insul., 1, 188-195, 1994

[59] T Maeno, H Kushibe, T Takada and C M Cooke, *"Pulsed electro-acoustic method for the measurement of volume charges in E-beam irradiated PMMA"*, Annual Report, Conference on Electrical insulation and Dielectric Phenomena, 1988

[60] I P Batra, K Keiji Kanazawa and H. Seki, *"Discharge characteristics on photoconducting insulators"*, J. Appl. Phys., 41, 3416-3422, 1970

[61] I P Batra, K Keiji Kanazawa, B H Schechtman and H Seki, *"Charge carrier dynamics following pulsed photoinjection"*, J. Appl. Phys., 42, 1124-1130, 1971

[62] H J Wintle, *"Decay of static electrification by conduction processes in polyethylene"*, J. Appl. Phys., 41, 4004-4007, 1970

[63] H J Wintle, *"Decay of Surface Electric Charge in Insulators"*, Japan. J. Appl. Phys. 10, 659-660, 1971

[64] I P Batra and K K Kanazawa, *"On the 'cross-over' effect in surface potential decay"*, Japan. J. Appl. Phys., 10, 267-268, 1971

[65] T J Sonnonstine and M M Perlman, "*Surface potential decay in insulators with field dependent mobility and injection efficiency"*, J. Appl. Phys., 41, 3975-3981, 1975

[66] E A Baum, T J Lewis and R Toomer, "*Further observations on the decay of surface potential of corona charged polyethylene films"*, J. Phys. D: Appl. Phys., 10, 2525-2531, 1977

[67] K J Kao, S S Bamji and M M Perlman, "*Thermally stimulated discharge current study of surface charge release in polyethylene by corona generated excited molecules, and the crossover phenomenon"*, J. Appl. Phys., 50, 8181-8185, 1979

[68] R Toomer and T J Lewis, *"Charge trapping in corona-charged polyethylene films"*, J. Phys. D: Appl. Phys., 13, 1343-56, 1980

[69] J M Alison and R M Hill, "*A model for bipolar charge transport trapping and recombination in degassed crosslinked polyethylene"*, J. Phys. D: Appl. Phys., 27, 1291-1299, 1994

[70] N F Mott and R W Gurney *Electronic Processes in Ionic Crystals 2nd edn*, Oxford: Clarendon, 1948

[71] Y V Serdyuk and S M Gubanski, *"Computer modeling of interaction of gas discharge plasma with solid dielectric barriers"*, IEEE Trans. Dielectr. Electr. Insul., 12, 725-735, 2005

[72] S L Roy, G Teyssedre and C Laurent, "*Charge transport and dissipative process in insulating polymers: experiments and model"*, IEEE Trans. Dielectr. Electr. Insul., 12, 644-654, 2005

[73] G Chen, J Zhao and Y Zhuang, "*Numerical Modeling of Surface Potential Decay of Corona Charged Polymeric Material"*, IEEE International Conference on Solid Dielectrics, 2010

[74] G Chen, *"A New Model for Surface Potential Decay of Corona-charged Polymers"*, J Phys. D: Appl. Phys., 43, 055405, 2010

[75] Y Zhuang, G Chen and M Rotaru, "*Charge injection in gold ground electrode corona charged polyethylene film: numerical simulation on surface potential decay*", IEEE 14th International Symposium on Electrets (ISE), 2011

[76] L Zhang, Z Xu and G Chen, *"Decay of Electric Charge on Corona Discharge Polyethylene"*, 2nd Euro-Asian Pulsed Power Conference, 2008

[77] S L Roy, P Segur, G Teyssedre and C Laurent, "*Description of bipolar charge transport in polyethylene using a fluid model with a constant mobility: model prediction*", J. Phys. D: Appl. Phys., 37, 298-305, 2004

[78] G C Montanari, G Mazzanti, F Palmieri, A Moton, G Perego and S Serra, "*Space-charge trapping and conduction in LDPE, HDPE and XLPE"*, J. Phys. D: Appl. Phys., 34, 2902-2911, 2001

[79] D R Lide *CRC handbook of Chemistry and Physics 89th edition*, 2008

[80] Z Ziari, S Sahli and A Bellel, *"Surface potential decay of low density polyethylene (LDPE) films under different corona discharge conditions"*, M. J. Condensed Matter, 2010

[81] G Chen and J Zhao, *"Observation of negative differential mobility and charge packet in polyethylene"*, J. Phys. D: Appl. Phys., 44, 212001, 2011

[82] X Wang, *"Measuring energy distribution of surface trap in polymerinsulation by PEA method"*, Proc CSEE, 29, 127-132, 2009

[83] G Chen, H Xiao and Z Xia, *"Charge storage characteristics in hybrid electret film consisting of porous PTFE and PP with negative corona charging"*, Acta Phys Sin, 55, 2464-2469, 2006

[84] C Tang, R Liao, G Chen and L Yang, *"Research on the feature extraction of DC space charge behaviour of oil-paper insulation"*, Tech. Sci. China, 54, 1315-1324, 2011

[85] W Shen, H Mu, G Zhang, J Deng and D Tu, *"Identification of electron and hole trap based on isothermal surface potential decay model"*, J. Appl. Phys., 113, 083706, 2013

[86] G Chen, *"Influence of gamma irradiation on surface potential decay of corona charged polyethylene"*, J. Electrostatics, 68, 487-491, 2010

[87] Z Ziari, S Sahli, A Bellel, Y Segui and P Raynaud, "*Simulation of surface potential decay of corona charged polyimide*", IEEE Trans. Dielectr. Electr. Insul., 18, 1408-1415, 2011

[88] K Sekimoto and M Takayama, "*Surface analysis of traces stained with discharge on plane electrode in atmospheric pressure negative corona*", J. Electrostatics, 70, 363-373, 2012

[89] C Gao, "*Effects of nanometer material and their application*", J. Jiangsu Uni. Sci. Tech., 22, 63-70, 2001

[90] C Cheng, "*Nanostructured material's special effects and its applications*", J. Anhui Institute of Architecture, 4, 43-47, 2005

[91] T J Lewis, "*Interfaces are the dominant feature of dielectrics at the nanometric level*", IEEE Journals & Magazines, 11, 739-753, 2004

[92] J Nelson, "*Role of the interface in determining the dielectric properties of nanocomposites*", Annual Report Conference on Electrical Insulation and Dielectric Phenomena, 2004

[93] C Zhang, "*The dielectric behaviour of the interface in polymer nanocomposites*", IEEE International Conference on Solid Dielectrics, 2007

[94] W Qiu, Y Luo, F Chen, Y Duo and H Tan, *"Morphology and size control of inorganic particles in polymide hybirds by using $SiO_2$-$TiO_2$ mixed oxide"*, Polymer, 44, 5821-5826, 2003

[95] J Zha, H Song, Z Dang, C Shi, and J Bai, *"Mechanism analysis of improved corona-resistant characteristic in polyimide/TiO2 nanohybrid films"*, Applied Physics Letters 93, 192911, 2008

[96] J Zha, Z Dang, H Song, Y Yin and G Chen, *"Dielectric properties and effect of electrical aging on space charge accumulation in polyimide/$TiO_2$ nanocomposite films"*, J. Appl. Phys, 108, 094113, 2010

[97] G Chen, T J Sadipe, Y Zhuang, C Zhang and G C Steven, *"Conduction in Linear Low Density Polyethylene Nanodielectric Materials"*, The 9th International Conference on Properties and Applications of Dielectric Materials, 2009

[98] S Zhukov and H V Seggern, "*Piezoelectrets from sandwiched porous polytetrafluoroethylene films with different porosity"*, International Conference on Solid Dielectrics, 2010

[99] J Zha, G Chen, Y Zhuang and Z Dang, *"Novel surface potential decay of $TiO_2$-based polyimide nanocomposite films"*, Annual Report Conference on Electrical Insulation and Dielectric Phenomena, 2010

[100] T N Tran, I O Golosnoy, P L Lewin and G E Georghiou, "*Two dimensional studies of trichel pulse in air using the finite element method"*, IEEE Conference on Electrical Insulation and Dielectric Phenomena, 2009

[101] T N Tran, I O Golosnoy, P L Lewin and G E Georghiou, "*Numerical modelling of negative discharges in air with experimental validation*", J. Phys. D: Appl. Phys., 44, 015203, 2011

[102] G E Georghiou, R Morrow and A C Metaxas, "*A two-dimensional, finite-element, flux-corrected transport algorithm for the solution of gas discharge problems*", J. Phys. D: Appl. Phys., 33, 2453-2466, 2000

[103] P Espel, J Paillol, T Reess, A Gilbert and P Domens, "*Numerical modeling of negative corona discharge in $SF_6$ at atmospheric pressure*", J. Phys. D: Appl. Phys., 35, 318-327, 2002

[104] S Kumara, Y V Serdyuk and S M Gubanski, "*Surface charge relaxation in silicone rubber and EPDM*", Annual Report Conference on Electrical Insulation and Dielectric Phenomenon, 2009

[105] S Kumara, Y V Serdyuk and S M Gubanski, "*Charging of polymeric surfaces by positive impulse corona*", IEEE Trans. Dielectr. Electr. Insul., 16, 726-733, 2009

[106] O Ducasse, L Papageorghiou, O Eichwald, N Spyrou and M Yousfi, "*Critical analysis on two-dimensional point-to-plane streamer simulations using the finite element and finite volume methods*", IEEE Trans. Plasma Sci., 35, 1287-1230, 2007